FLORIDA INTERNATIONAL UNIVERSITY

Miami, Florida

IN SITU ARSENIC SPECIATION USING SURFACE-ENHANCED RAMAN SPECTROSCOPY AND THE COFFEE RING EFFECT

A dissertation submitted in partial fulfillment of

the requirements for the degree of

DOCTOR OF PHILOSOPHY

in

CHEMISTRY

by

Valery Liamtsau

2021

To: Dean Michael R. Heithaus
College of Arts, Sciences and Education

This dissertation, written by Valery Liamtsau, and entitled In Situ Arsenic Speciation Using Surface-Enhanced Raman Spectroscopy and the Coffee Ring Effect having been approved in respect to style and intellectual content, is referred to you for judgment.

We have read this dissertation and recommend that it be approved.

Barry P. Rosen

Bruce McCord

Jaroslava Miksovska

Anthony McGoron

Yong Cai, Major Professor

Date of Defense: June 8, 2021

The dissertation of Valery Liamtsau here is approved.

Dean Michael R. Heithaus
College of Arts, Sciences and Education

Andrés G. Gil
Vice President for Research and Economic Development
and Dean of the University Graduate School

Florida International University, 2021

DEDICATION

I dedicate this dissertation to

my parents, Svetlana Liamtsava and Victor Liamtsau

and

my extended family, Alexei Liamtsau and Natalia Liamtsava

for their love, support, and encouragement throughout my Ph.D. journey.

ACKNOWLEDGMENTS

I would like to express my appreciation to Dr. Yong Cai – my major Professor, for providing the opportunity to carry out the research in his scientific group. Providing his guidance, financial support, and deep understanding of environmental chemistry processes, I have this work completed. I am also grateful to the rest of my committee members, Dr. Barry P. Rosen, Dr. Jaroslava Miksovska, Dr. Bruce McCord, and Dr. Anthony McGoron for their insights, comments, and suggestions during our annual meetings. Especially, I thank Dr. Anthony McGoron in Biomedical Engineering Department for providing me with the Raman spectroscopy station and financial support to maintain the instrument, it would be impossible for this work to be completed without the Raman spectroscopy. Special thanks to Dr. Guangliang Liu (our lab manager and assistant director), and Dr. Changjun Fan (chemist lead at Shimadzu) for their suggestions and comments.

I also would like to thank the following persons, Dr. Alexander Mebel and Alexander N. Morozov for beneficial suggestions in computational chemistry, Dr. Cassian D’Cunha from FIU HPC faculty for the technical support and FIU mass facility for their help in MS analysis.

Lastly, I would like to express my deepest appreciation and gratefulness to my family, my mother Svetlana Liamtsava and my father Victor Liamtsau for their constant and unconditional supports and love.

ABSTRACT OF THE DISSERTATION

IN SITU ARSENIC SPECIATION USING SURFACE-ENHANCED RAMAN SPECTROSCOPY AND THE COFFEE RING EFFECT

by

Valery Liamtsau

Florida International University, 2021

Miami, Florida

Professor Yong Cai, Major Professor

The coffee ring effect (CRE) phenomenon is originated from the nonuniform solvent evaporation of a sessile droplet deposited onto the flat substrate. Once the evaporation starts, the droplet suspended particles move outwards by the radial flow and concentrate in the edge region of the evaporating droplet, resulting in the formation of the so-called CRE stains. In this work we have expanded the applications of the CRE from separation of particles and macromolecules to small molecules, in particular, coupled to surface-enhanced Raman spectroscopy (SERS). Herein, we have developed a theoretical framework to describe the CRE-driven separation process of small molecules, using SERS analysis of dimethylarsinic acid (DMA^V), dimethylmonothioarsinic acid (DMMTA^V), and dimethyldithioarsinic acid (DMDTA^V) on gold nanofilm (AuNF) as an example. By combining the CRE theory for the radial flow and the Extended Derjaguin-Landau-Verwey-Overbeek (XDLVO) theory for mass transfer between solution and AuNF surface, we adapted the conventional chromatographic theory to derive a modified van Deemter equation for the CRE-driven separation. By using this model, we predicted the travel distances of arsenicals based on the different affinity of analytes to AuNF and evaluated

the possibility of separation of unknown analytes by CRE-based SERS, demonstrating the successful adaptation of classic chromatographic theory to CRE-driven nanochromatography.

Furthermore, we have extrapolated the application of the developed method for the speciation of the peptide-like arsenic-based anticancer drug Darinaparsin (DAR) and its major breakdown product dimethylarsino-cysteine (DMAC). Despite the overlap of DAR and DMAC's Raman spectra in the final CRE deposit, we were able to identify each compound due to their unique SERS fingerprint. Overall, the developed method was able not only to separate and identify the S-conjugated arsenicals, but at the same time to preserve the DAR and DMAC's As^{III} oxidations state and the fragile As – S moiety, thus providing an alternative speciation method for unstable thioarsenicals. The key advantage of the application of this method for peptides separation is the separation coupled with the mild detection providing the rich structural information of each metabolite.

TABLE OF CONTENTS

CHAPTER PAGE

LIST OF TABLES

LIST OF FIGURES

FIGURE PAGE

LIST OF ABBREVIATIONS AND SYMBOLS

AFM	Atomic force microscope
AgNF	Silver nanofilm
AgNPs	Silver nanoparticles
APL	Acute promyelocytic leukemia
APTMS	3-Aminopropyl)trimethoxysilane
As^{III}	Arsenite
As^{V}	Arsenate
ATO	Arsenic trioxide
AuNF	Gold nanofilm
CE	Chemical enhancement
CRE	Coffee ring effect
DAR	Darinaparsin
DFT	Density Functional Theory
DI water	Deionized water
DMA^{V}	Dimethylarsinic acid
DMAC	Dimethylarsino-cysteine
$DMDTA^{V}$	Dimethyldithioarsinic acid
$DMMTA^{V}$	Dimethylmonothioarsinic acid
DNA	Deoxyribonucleic acid
EE	Electromagnetic enhancement
GC	Gas chromatography
GE-ICP-MS	Gel electrophoresis inductively coupled plasma mass spectroscopy

GSH	Glutathione
HOMO	Highest occupied molecule orbital
HPLC	High-performance liquid chromatography
HSAB	Hard/soft acid-base
IC	Ion chromatography
ICP-MS	Electrospray ionization mass spectrometry
LFA	Lateral flow immunoassay
LOD	Limit of detection
LUMO	Lowest unoccupied molecule orbital
MALDI	Matrix-assisted laser desorption ionization spectrometry
MMA^V	Monomethylarsonic acid
PAHs	Polycyclic aromatic hydrocarbons
PVP	Polyvinylpyrrolidone
Rh6G	Rhodamine 6G
ROS	Reactive oxygen species
SCRF	Self-Consistent Reaction Field method
SDS	Sodium dodecyl sulfate
SERS	Surface-enhanced Raman spectroscopy
SPR	Surface plasmon resonance
TEM	Transmission electron microscope
TLC	Thin layer chromatography coupled
XDLVO	Extended Derjaguin-Landau-Verwey-Overbeek theory

Chapter 1. Introduction, Problem Statement, Objectives, and Hypotheses

1.1 The coffee ring effect phenomenon

The evaporations of sessile droplets lying onto the solid substrate draw attention to the fundamentals of this physical phenomenon and its applications. This phenomenon emerged from the daily life of the process of the spilled coffee drops evaporation. Once a coffee droplet is deposited onto the solid substrate and the solvent starts evaporating, the ring-like stains are forming due to the radial outward flow driving the coffee powder particles from the center to the edge region of the evaporating droplet. This phenomenon is called the coffee ring effect (CRE)[1], which finds its industrial applications in inject printing[2], fabrication of the nanomaterials[3], plasmonics, and the colloidal particles depositions[4]. The evaporation of the droplet deposited onto the surface is nonuniform, peaking at the liquid-solid-air interface, where the highest velocity of solvent-air diffusion is observed. Once the evaporation starts, the outward radial flow drives the particles to the edge, replacing the evaporated solvent. The solute transport from the center to the edge region of the drying droplet is an intricate process, which is dependent upon the substrate polarity hydrophobicity[5], hydrophilicity[6], the presence of the surfactants[7], the substrate temperature[7] and the substrate surface charge[8]. Several theoretical models were presented to describe the processes that govern the morphology of the CRE deposit. The first and well-known model was developed by Deegan et al. who described the velocity of the radial flow and the particle transport equation[1]. Later, the influence of the major factors such as the receding of the contact line[9], center-enhanced flux[10], and presence of surfactants[11] were investigated during the formation of the CRE deposit. Extensive research has been devoted to understanding, suppressing, and ultimately controlling the

CRE. General rules have been established to control the CRE by tuning these interactions, and guidelines for the rational physicochemical formulation of colloidal suspensions capable of depositing particles in desirable patterns were provided. This opened perspectives for the reliable control of the CRE in real-world formulations and created new paradigms for flexible particle patterning at all kinds of interfaces as well for the application of the CRE as a robust and inexpensive diagnostic tool[3].

1.2 The theory of CRE

The solvent evaporation rate of a droplet placed onto the flat support is a quasi-steady process that is dominated by diffusion from the droplet surface to the atmosphere[12] and mainly depends upon the evaporation time. The basic model for the theory of drying droplets was developed and well known[9]. The theoretical and mathematical models have been developed to describe the process that occurs during droplet evaporation. We have summarized the key concepts of the radial flow-induced due to the droplet evaporation, the attraction-repulsive interactions of the analytes with the CRE substrate surface. To describe the sessile droplet lying onto the flat surface, the cylindrical coordinate system was applied and the key droplet features as the droplet height $h_0(t)$, droplet radius r, and the three-phase contact angle were depicted in **Figure 1**.

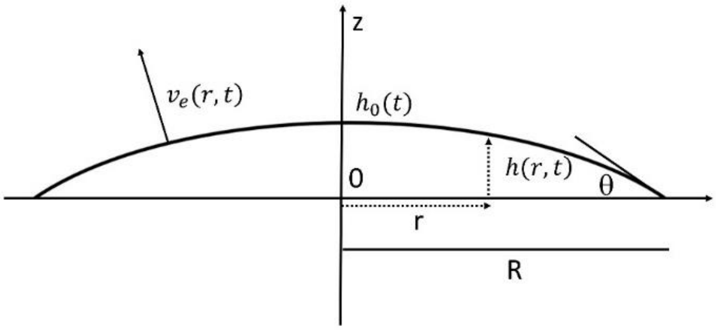

Figure 1. The mathematical outlook of the lying droplet cross-section.

The equation for the change of drop height throughout the drying $\mathrm{h(r,t)}$, could be expressed as

$$\mathrm{h(r,t)} = \sqrt{\left(\frac{\mathrm{R^2 + h_0(t)^2}}{\mathrm{2h_0(t)}}\right)^2 - \mathrm{r^2}} - \frac{\mathrm{R^2 - h_0(t)^2}}{\mathrm{2h_0(t)}}, \qquad 1)$$

where $\mathrm{v_e(r,t)}$ is the evaporation rate, $\mathrm{h_0(t)}$ is the initial droplet height, $\mathrm{h(r,t)}$ is the height profile that changes with the radius, R is the radius, r is the distance from the center to the specific point across the y-axis, θ is the contact angle.

The velocity of evaporation remains constant most of the time[13], even though it is nonuniform and maximized at the pinned contact line[1]. To derive the evaporation rate J from the eq 1, the following assumptions are made: the shape of the droplet is a semispherical cap[14], suspended particles are uniformly distributed, the contact line remains pinned during the evaporation[15], and temperature, electrostatic, and gravity effects—are negligible[1, 16]. Also, the drop height is much smaller than the drop radius and the receding contact angle ($\theta \ll 1$). The radial flow is linearly proportional to the evaporation flow and inversely related to the density of the solution[17, 18]:

$$\mathrm{u_r} = \frac{J}{p} \qquad 2)$$

where J is the evaporation rate, ρ is the density of the solution, $\mathrm{u_r}$ is the radial outward flow.

$$\frac{\mathrm{dm}}{\mathrm{dt}} \approx 1/(\mathrm{t_f} - \mathrm{t})^{1/4} \qquad 3)$$

where $\frac{\mathrm{dm}}{\mathrm{dt}}$ – the velocity of the particle's deposition, $\mathrm{t_f}$ – total evaporation time, t – evaporation time at the specific moment.

Regarding the interactions of the particles with substrate surface (forces responsible for the CRE deposit), electrostatic and van der Waals forces between the particles and the solid substrate are typically calculated by the DLVO theory. The surface-charged groups that stabilized the nanoparticles in a solution induce the surface charge onto the surfaces of the nanoparticles. To illustrate this, titania nanoparticles adsorption into the glass surface in an acid/base solution was investigated and the forces were computed providing evidence that the electrostatic attraction between the titania nanoparticles and the glass substrate results in the homogeneous distribution of the titania across the CRE substrate, in contrast, however, the electrostatic repulsion induced the CRE promotion aggregating the TiO2 nanoparticles near the edge region of the glass substrate. The substrate/particle interaction: electrostatic and wan der Waals and donor-acceptor:

$$\mathrm{F_{DLVO}} = \mathrm{F_{el}} + \mathrm{F_{vdW}} \qquad 4)$$

$\mathrm{F_{DLVO}}$ – total interaction of the particles with the solid substrate, $\mathrm{F_{el}}$ – electrostatic interactions, $\mathrm{F_{vdW}}$ – van der Waals interactions.

The third flow pattern is a Marangoni resulting in a central bump in the center of the CRE evaporating droplet. The typical velocity provided analytically:

$$V_{Ma} \approx \frac{1}{32}\left(\frac{\beta\varphi_i^2\Delta T}{\mu}\right) \qquad 5)$$

In this equation, φ is the wetting angle of the drop, μ is dynamic viscosity, β is the gradient of surface tension concerning the temperature, and ΔT is the temperature difference between the edge and the top of the droplet.

The CRE formation of the colloidal particles is predominantly governed by the two major mechanisms: the radially outward flow and the interactions of the analytes with the substrate surface providing that the Marangoni flow is weak in the aqueous solutions. The interactions through the oppositely charged surface and nanoparticles would lead to the suppression of the CRE resulting in the high uniform particle distribution across the nanofilm. Manipulating pH would affect particles-nanofilm interactions and thus, giving an option to suppress or to promote the CRE formation for certain specific purposes.

1.3 The analytical applications of CRE

The CRE preconcentrates the microparticles, nanoparticles, and the chemicals at the edge of the evaporated droplet, enabling the detection of single molecules as illustrated by coupling CRE to two common detection methods, surface-enhanced Raman spectroscopy (SERS)[19] and matrix-assisted laser desorption ionization (MALDI) spectrometry[7]. Also, the CRE is often employed for the separation and the deposition of the large particles aiming solely for the preconcentration of the analytes at the borderline, enabling the unprecedented levels of detection down to a single molecule[20]. The promotion of the CRE has been commonly employed for the preconcentration of particles or chemical compounds onto the ring region, thus enhancing the detection limit of the techniques. Typically, the analytes are mixed with the nanoparticles and this colloidal solution is deposited onto the planar surface. Once the solvent evaporates, the analytes bonded to the nanoparticles or microparticles start driving away from the center region of the drying droplet and concentrating into the ring stain (**Scheme 1**). Another important analytical application of CRE is the partial or total separation of the small peptides from the matrix as illustrated by MALDI, due to either distinct interactions of the nanoparticles bonded with the target molecules, or due to the size driven separations[21].

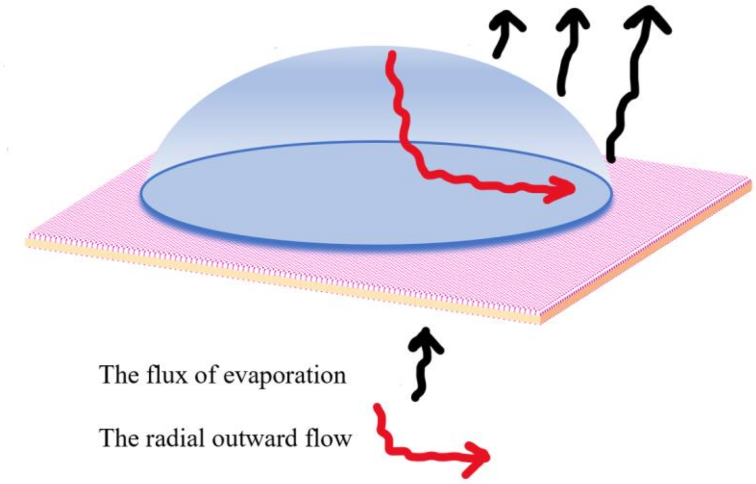

Scheme 1. Mechanisms influencing the formation of a coffee ring deposit.

Raman spectroscopy is a rapid and nondestructive method which offers rich and unique fingerprint of a molecule based on vibrational spectra. This method does not require sample preparation and capable of analyzing solid, liquid or gaseous samples[22]. Raman spectroscopy also allows the simultaneous detection of metabolites using distinct fingerprint vibrations for each compound[23]. The major limitation of this technique is the weakness of Raman signal and low cross section of the Raman scattering process (between 10^{-30} and 10^{-25} cm^2). To overcome the low intensity of Raman signal, surface enhancing methods, e.g., using certain metallic nanoparticles (NPs), have been employed for the amplification of Raman signal. For example, Au and Ag colloids can enhance the Raman intensity by a factor of 10^{14} [24], which means these colloidal substrates are capable of detecting a single molecule[25]. Thus, this technique, Surface-Enhanced Raman spectroscopy (SERS), efficiently combines the specificity of Raman signature with high sensitivity. In SERS abbreviation, the first "S" means a "surface" spectroscopy technique (the analytes must be on or close to the surface), "E" means signal "enhancement" (ensured by plasmon resonances in the metal) and "R" means "Raman" (providing fingerprint information about studied analyte). Last "S" means "scattering" or "spectroscopy". Currently, there are two separate enhancement mechanisms for overall SERS effect: the electromagnetic effect (EM) and the chemical effect (CM). EM is regarded as a long-range effect, in which the localized electromagnetic field plays a key role in SERS. CM is the interaction of the molecules adsorbed on the metal surface with the metal, such as the charge transfer of the adsorbate to the metal[26]. To obtain SERS signal molecule must be very close to the surface of nanoparticle (10 nm). Overall, SERS has many advantages over ordinary spectroscopic analytical techniques such as extremely high sensitivity, molecular selectivity, intense signals, and great precision[27].

Surface-enhanced Raman Spectroscopy is a widely used technique for bioanalytical sensing in living cells, viruses and microorganisms[28]. DNA, proteins and antitumor drugs can be detected by delivering individual or aggregated nanoparticles into cells following intrinsic intracellular SERS spectra measurements of immediate surroundings of nanoparticles[29-31]. Transport of nanoparticles inside the cell generally occurs by passive uptake of nanoparticles incubated with cells. However, this time-consuming method has poor translocation efficiency and control issues over distribution and aggregation of nanoparticles inside cells. Recently discovered ultrasound mediated delivery allows rapid transfer of nanoparticles into living cells without damaging cell nucleus and keeping cells alive. Reproducible SERS spectra were obtained by this method[32].

SERS detection for ciprofloxacin and norfloxacin analytes, two largely used antibiotics in the world, was performed by the enrichment and efficient delivery of analytes to the border of the evaporating droplet deposited onto the dip coated slippery-SERS substrates. The analyte particles with gold nanorods were efficiently transported to the active site resulting in the increase of particle concentrations, and, consequently, SERS signal at the edge of the droplet[33]. Unlike the previously mentioned regular dip coating process, the authors modified substrate fabrication by restricting the nanostructure deposition only to a very small area of the larger substrate concentrations and allowed the detection of noxious pathogens: *Staphylococcus aureus* *(S. aureus)* and Rhodamine 6G (Rh6G) down to a single molecule. To enhance the signal intensities further, they employed natural three-phase pinning to preconcentrate the gold nanoflowers analytes on nanostructure pocket, allowing maximal deposition at the CRE edges and thus the lowest

LOD down to 10^{-12} M[19]. Similarly, Minh and coworkers developed the TLC-SERS based method for the detection of sildenafil in drugs and herbal products. For the first time, the unique double "double coffee-ring effect" was reported promoting the separation of the herbal constituents and resulting in the redistribution of both silver nanoparticles and sildenafil molecules. The preconcentration of the sildenafil bonded nanoparticles in the edge of the CRE strain was obtained under double CRE[34].

The CRE was directly applied for the bioanalytical sensing, where an inexpensive optical sensing platform was manufactured by combining SERS detection with CRE-based nanofilm separation. The gold nanoparticle colloidal mix with the serum from patients with colorectal cancer was placed onto the glass surface and Raman spectra were acquired from the coffee-ring-like region at the rim, providing strong and stable SERS profiles[35]. To further optimize the surface capturing of the target analytes, Ag nanoparticles coated with β-cyclodextrin were used for the traditional anti-diabetic drug phenformin hydrochloride sensing. β-CD-functionalized nanoparticles were modified in a way to capture the drug and to position it in a fixed molecular orientation inside the hydrophobic cavity enabling the LOD as low as 8.0×10^{-9} mol L^{-1}[36].

The speciation of environmental hydrophobic pollutants, polycyclic aromatic hydrocarbons (PAHs), poses a clear challenge because the separation step is important before the detection and identification of PAHs using bare AuNPs[37]. To stabilize nanoparticles formation polyvinylpyrrolidone (PVP) was used as a capping agent. The results indicated that an increase in surface roughness reduced the sizes of the coffee rings, whereas the addition of PVP not only stabilized the AuNPs but also improved the robustness of the coffee rings. When applying the proposed method to determine the phenylalanine level in urine for rapid screening of the phenylketonuria disorder, strong chemical interference from uric acid, which is a major component in urine, was observed[38]. In addition to the SERS detection, the lateral flow immunoassay (LFA) biosensor was developed to measure the color change in the test zone allowing the sensitive detection of *staphylococcal enterotoxin B* (SEB) by incorporating hollow gold nanospheres probes instead of traditional gold nanoparticles. With the proposed SERS-based LFA strip, the presence of a target antigen was identified through a color change in the test zone. By measuring SERS signals of SEB from the test zone, the system LOD estimated with the SERS-based LFA strip was calculated as 0.001 ng mL^{-1}[39]. Overall, SERS platforms for the CRE displayed high sensitivity, robustness, reproducibility, and simplicity make this platform ideal for on-site analysis of small volume samples at low concentrations in complex matrix[40].

Zhang and coworkers developed the immunoassay for the DNA readout which comprised of the silica nanofilm used as a substrate to amplify the nucleic acids based upon the CRE formation. The colloid monodispersed silica nanoparticles were hexagonally close-packed providing the highly structured substrate providing the concentration of the nucleic acids by the loop-mediated isothermal amplification into the edge region of the frying droplet. For the detection was employed the smartphone providing the determination of the DNA structural elements[36]. The nanoparticles-based substrate might be used not only for the separation of the analytes due to the distinct interactions, but also to enhance the weak Raman signal, allowing the SERS detection of the low analyte's concentration down to 1 pmol. Indeed, Kim and coworkers applied 30 nm-thick gold substrates with gold nanoparticles deposited onto aluminum wafer that offered the amplification of the weak Raman signal by 10^{13} resulting in the detection of six E. coli isolates from human blood culture, thanks for the unique Raman fingerprint. This approach offers high reproducibility with approximately 5% relative standard deviation[41]. An alternative approach to fabricate the CRE substrate was proposed by Liu et al. by laser-induced dynamic dip-coating method allowing the uniform deposition of nanoparticles onto the solid substrate, thus avoiding the problem of poor detection reproducibility in conventional SERS substrates. The authors offered a compact and robust micro-coffee-ring-patterned fiber facets SERS probe enabling the detection limit lower than 10^{-8} M of fungicides, thiram and methyl parathion found in orange juice[42].

The key advantage of the CRE substrates lies not only in their capability to partially preconcentrate analytes, but also to potentially promote the separation of the analytes based upon the unique interactions of molecules with the substrate surface. Moreover, various nanoparticles combinations found their application for the surface modifications of the CRE. For instance, the mixture of AgNPs and AuNPs (Au@AgNPs) was deposited onto the glass surface providing the substrate for the urea and ammonium sulfate hazardous adulterants detection in milk products by the means of the CRE. The uniform distribution of analytes was observed, with enhanced Raman signals detected in a small region (maximum 1.9 mm) across the center of the CRE. This method required a small sample volume of 2 µL with minor sample pretreatment steps such as pH adjustment, centrifugation, and depositing the sample on a gold-coated slide for drying[43]. In another study, the biofluids detection was performed on the Ag based substrate, from a silver ink on the glass, and its utilization for bio detection was shown. This approach allowed to achieve lower LODs by effectively measuring areas with higher concentrations of targeted molecules than the initial sample, providing a robust and cost-effective platform for the SERS detection. The substrate was fabricated from a silver ink and deposited on the glass demonstrating the unusual hydrophobicity that enables the preconcentration benefit of the drop-coating deposition through the formation of the CRE[44]. Following this approach, a gold nanoparticles assembly was applied for the bio spectral sensing chips. The AuNF was fabricated with different particle densities assembled on mechanical polished copper substrate, demonstrating that the plasmonic hot spots formed by AuNPs and copper surfaces play an important role in achieving fluorescence enhancement[45].

1.4 Speciation analysis of arsenic

Inorganic arsenic (iAs^{III}) is known as a carcinogen, toxic threat for humans and environmental contaminant. Chronic exposure to the arsenic contaminated drinking water has various harmful effects, such as liver, skin and bladder cancers[46], neurological disorders and cardiovascular diseases[47]. Daily consumption of grains, vegetables and seafood is another pathway of exposure to arsenic leading to various health problems[48]. In addition, anthropogenic activities: agricultural use of pesticides and herbicides, mining and power plants also contribute greatly to the arsenic existence in the environment[49]. However, since ancient times arsenic has been employed as a curing medicine for psoriasis asthma and tuberculosis[50]. Arsenic based drugs, Flowler's, Donovan's solutions, and Salvarsan were used to cure respiratory diseases[51]. Moreover, nowadays arsenic based drug Darinaparsin is successfully used for the treatment of acute promyelocytic leukemia (APL)[52].

The speciation of thioarsenicals has been usually performed by a chromatographic separation coupled with spectroscopic determination. High-performance liquid chromatography (HPLC) coupled with inductively coupled plasma mass spectrometry (ICP-MS) and/or electrospray ionization mass spectrometry (ESI-MS) methods were the most common techniques for analysis of these species[53-56]. However, the sample alteration during the analysis may occur. For instance, for HPLC separation of the thio-organoarsenate (2-dimethylarsinothioyl acetic acid), the acidic mobile phase degrades the analyte momentarily, while weak acidic solution makes it almost impossible to elute the analyte from the column[57]. For detection, because of thioarsenicals oxidation likely to happen during ESI-MS, the compounds must be further characterized by accurate mass spectrometry and 1H NMR spectroscopy. Another problem that could arise is the lack of precise structural information. Indeed, in the study of pentavalent thioarsenicals complexed with GSH, from analyzing the ESI-MS data, it is not conclusive whether the thioarsenical is pentavalent (GSH directly bound to As through its cysteine unit) or trivalent (GSH bound through a sulfur–sulfur bridge to As)[58]. In addition, trivalent oxygenated arsenical (DMA^{III}) has been misidentified, as a result of having similar chromatographic properties to those of $DMMTA^{V}$[59].

As far as sample preparation is concerned, the extraction of arsenic species from biological samples must be done when using the current HPLC-ICP-MS or ESI-MS methods for analysis of thioarsenicals. For example, extraction by using certain types of solutions such as water, methanol, buffers, nitric acid and hydrogen peroxide mixture (HNO_3/H_2O_2) with the assistance of physical means such as sonication and microwave-assisted digestion was the most common method for arsenic speciation in biological samples[60-63]. However, thioarsenicals are unstable species, and they could be easily decomposed at acidic pH during extraction process, resulting in the conversion of thioarsenicals to MMA^V and DMA^V[57]. Therefore, there is the need for the method that can provide researchers with detailed structural information and the one that does not require extensive sample preparation.

1.5 Problem Statement

The CRE driven applications are currently limited to the fabrication of the chromatographical devices aimed to separate micro and nanoparticles by exploiting the particle size variations. Although the crucial role of flow patterns for micro and nanoparticles in the CRE has been thoroughly theoretically and experimentally described, the potential of the CRE application for the separation of small molecules, peptides and proteins have been largely neglected, which is critical for the CRE based biological sensing, pollutant detection and metabolomics analysis. Besides that, the prediction of the analytes traveled distances is of key interest in the CRE driven small molecules separation, for which a theoretical approach is currently lacking, thus limiting the potential CRE field application and in biological sensing.

Even though SERS has been used for molecular detection based on the preconcentration effect of CRE, the hyphenated method coupling SERS to the CRE-driven separation has not been developed. The key issue with SERS measurements in colloidal solutions lies in the nonuniform distribution on the nanoparticles, thus the SERS output signals become unstable and the overall method reproducibility remains questionable. The nanofilm would not only offer the advantage of the highly ordered and fixed surface nanoparticles and the chromatographic potential for the separation species by the CRE, but also allows enhancing a weak Raman signal to obtain the rich structural molecular information. It is critical to characterize unstable compounds onto the nanofilm surface and record their Raman spectra or fingerprint Raman frequencies under the influence of biological matrices.

Raman shift is a crucial parameter for the SERS sensing for molecular structure elucidation. The pH-dependent variations in Raman shift, however, were not properly unified and a unified approach has not been theoretically developed, to the best of our knowledge. The variations of the Raman shift shed the light on the adsorption of the species onto the surface of the nanoparticles, allowing us to predict the adsorption mechanism based on these pH-dependent variations. Also, the bond formation dependency on the Raman shift was not explored yet, which is of the key interest of the researchers to assess the complex formation onto the surfaces, provide bond formation analysis, and estimate the strength of the interactions between the adsorbed species and the nanofilm surfaces.

1.6 Objectives

The present work was aimed to expand the applications of CRE-SERS analysis to small molecules. Through demonstrating the separation of arsenical species and identification of Raman spectra of major arsenicals and developing a theoretical framework to describe the CRE-driven separation, a speciation analysis method using CRE-driven separation coupled to SERS detection was established for arsenicals and potentially for small molecules in general. The specific aims were as follows.

1. Employing CRE phenomenon for arsenic speciation analysis.

Arsenic speciation of four common arsenicals including arsenite (As^{III}), arsenate (As^{V}), monomethylarsonic acid (MMA^{V}), and DMAV were carried out on the silver nanofilm (AgNF) and the separation driving force is the capillary flow generated during the evaporation of the CRE. Arsenic fingerprint SERS signals were detected under different buffer systems and these buffer systems were used to adjust the interaction between arsenicals and silver nanofilm surface (AgNF). If no significant separation could be achieved by using the typical CRE, surfactants would be introduced into the arsenic mixture solution. The introduction of surfactants reduced the surface tension and caused the solution in the sessile droplet to move outwards and carry arsenicals in the flow. Thus, arsenic separation was possible to achieve because of different interactions between arsenicals and the AgNF surface.

2. Application of CRE-SERS method for speciation of unstable thioarsenicals.

The CRE-driven separations did not require extensive sample preparation and were applied for the sensing of the unstable thioarsenicals, such as dimethylmonothioarsinic acid (DMMTA^V) and dimethyldithioarsinic acid (DMDTA^V). A previously developed method based on surface-enhanced Raman spectroscopy (SERS) detection in combination with the CRE for separation was applied for the speciation of thioarsenicals. Through calculating the pKa's of DMMTA^V and DMDTA^V and accordingly manipulating the chemical environment, separation of these thioarsenicals was executed exploiting the thioarsenicals different traveled distances during the development of the coffee ring.

3. Development of a unified approach for the CRE driven separations of small molecules.

The unified nanochromatographical theoretical approach was developed by combining the general chromatography theory, DLVO theoretical approach, and the theory behind the CRE-driven particle separations. I created a theoretical framework to describe the CRE-driven separation process of small molecules, using SERS analysis of dimethylarsinic acid (DMA^V), dimethylmonothioarsinic acid (DMMTA^V), and dimethyldithioarsinic acid (DMDTA^V) on gold nanofilm (AuNF). By combining the CRE theory for the radial flow and the Extended Derjaguin-Landau-Verwey-Overbeek (XDLVO) theory for mass transfer between solution and AuNF surface, I adapted the conventional chromatographic theory to derive a modified van Deemter equation for the CRE-driven separation. By using this model, I predicted the travel distances of arsenicals based on the different affinity of analytes to the AuNF and evaluated the possibility of separation of unknown analytes by CRE-based SERS, demonstrating the successful adaptation of classic chromatographic theory to CRE-driven nanochromatography.

4. Extrapolation of small molecule CRE-SERS method for separation and speciation of peptide-arsenic conjugates.

I applied the nanochromatography method for the speciation of peptides DAR and DMAC, which combined the CRE-SERS approach. I manipulated pH and exploited the molecular size of compounds to optimize their separation. I detected DAR in the center and the middle regions, whereas DMAC traveled a longer distance across the CRE stain and was detected in the middle and the edge regions. Despite the possible overlap of DAR and DMAC's Raman spectra, I identified each compound due to their unique SERS fingerprint. Overall, the developed method not only allowed us to separate and identify the S-conjugated arsenicals but at the same time to preserve the DAR and DMAC's As^{III} oxidations state and the fragile As – S moiety, thus providing an alternative speciation method for unstable thioarsenicals.

5. Toward understanding of pH-dependent Raman shift using theoretical and experimental approaches

Raman shift is the key parameter for the evaluation of the adsorbed molecule–surface interactions and predicting the final geometry of adsorbed complexes onto nanomaterial surface. I developed the theoretical approach evaluating the influence of the variations of Raman shift of the adsorbed molecules onto the types of bonds formed between the molecules and nanofilm (AuNF). I employed three common arsenic species: DMA^V, DMMTA^V, and DMDTA^V as models for the theory development. By theoretically calculated interaction energies of species with Au cluster, I extrapolated this to the predictions of the Raman shift and the Raman shift variations with pH of the unknown arsenic species. Moreover, I classified the interactions of the various molecules with the citrate-coated gold nanoparticles. Typically, as pH increases, and overcomes pKa, charge transfer becomes more favorable leading to the stronger interactions of molecules with AuNF surface. Thus, I defined the interactions of molecules with AuNF surface by classifying the covalent and electrostatic interactions, providing the model for the prediction of the interactions based on the molecular charge and the Raman shift.

1.7 Hypotheses

The established objectives were guided by the following hypotheses:

The coffee ring effect would constrain all solutes within the region of the droplet because of strong surface tension, preventing solutes from migrating to the droplet peripheral region. During evaporation, most solutes would be pushed to the edge of the droplet by the capillary flow. Under this circumstance, it would be difficult to accomplish the separation of multiple arsenicals. Surfactants would be used to reduce the solute surface tension allowing the solvent permeation into the peripheral region outside the droplet region by a strong capillary action at the contact line. The capillary action would cause a flow to carry the solutes to move outwards. Different arsenicals would have different adsorption/desorption interactions with the AgNF surface. Therefore, the arsenicals would be separated using the coffee ring effect.

Thioarsenicals appear to be among the key intermediates involved in arsenic metabolism due to their wide detection in biological samples post As exposure, the capability of binding to proteins, and potentially high toxicity. Thioarsenicals are unstable species, and they could be decomposed at acidic pH or species alteration may occur during the analysis, thus, this is critical to developing a method for the speciation of unstable species. Due to the drawbacks of currently available methods for the analysis of thioarsenicals, it is believed that the inaccurate information (e.g., underestimation and/or speciation conversion) was associated with the analysis of thioarsenicals in previous studies.

Raman shift could be the key parameter for the evaluation of the molecular adsorption onto nanomaterial surface. It is possible to estimate the species adsorption and bond formation through the theoretical calculation of interactions energies of species with nanomaterials, however, it is time and resources consuming, thus I hypostasize that pH variations of the Raman shift might reveal the dependency of the analytes interactions with to the AuNF during the adsorption process. Also, Raman shift might allow classifying the interactions of the various molecules with the citrate coated gold nanoparticles. Besides, the unified theoretical approach would reveal the pH dependence of the Raman shift adsorption. Thus, I plan to develop a unified approach for the Raman shift variations to classify the bond formation through the adsorption onto the AuNF surface.

Chapter 2. Arsenic speciation on silver nanofilms by surface-enhanced Raman spectroscopy

Part of this chapter was published as a research paper for which I was one of the two co-first authors in the journal Analytical Chemistry. Adapted with permission from Yang, M.W., Liamtsau, V., Fang, C.J., Sylyers, K.L., McGoron, A.J., Liu, G.L., Fu, F.F., Cai, Y., 2019. Arsenic Speciation on Silver Nanofilms by Surface-Enhanced Raman Spectroscopy. Anal. Chem. 91, 8280-8288. Copyright (2019) American Chemical Society.

2.1 Abstract

Surface-enhanced Raman spectroscopy (SERS), as a non-destructive and fast detection technique, is a promising alternative approach for arsenic detection, particularly for *in situ* applications. SERS-based speciation analysis according to the fingerprint SERS signals of different arsenicals has the potential to provide a superior technique in species preservation over the conventional chromatographic separation methods. In this study, we explored a novel SERS method for arsenic speciation by using the separation potential of the coffee ring effect on negatively charged silver nanofilms (AgNFs). Four arsenic species, including arsenite (As^{III}), arsenate (As^{V}), monomethylarsonic acid (MMA^{V}), and dimethylarsinic acid (DMA^{V}), were measured for fingerprint SERS signals in solution and on the films. Significant enhancement of SERS signals on the dried coffee ring stains by the AgNFs was observed except for As^{III}, and more importantly, arsenicals migrated varying distances during coffee ring development, promoting better speciation. Sodium dodecyl sulfate was then introduced into the droplet to reduce the droplet surface tension, facilitating the migration of solution into the peripheral region. Under the combined interactions of arsenicals with the AgNFs, solvent, and surfactant, the enhanced separation between arsenicals was observed as a result of the formation of two concentric rings. Combining the SERS fingerprint signals and physical separation of arsenicals on the surface, arsenic speciation was achieved using the AgNFs substrate-based SERS technology, demonstrating the potential of the coffee ring effect for rapid separation and analysis of small molecules by SERS.

Keywords: Coffee ring effect, Arsenic speciation, SERS, Silver nanofilm

2.2 Introduction

Speciation analysis of toxic metals and metalloids is often performed by the separation of different species followed by detection. For arsenic speciation, the conventional method is the combination of chromatographic separation with spectrometric detection techniques. The popular separation techniques include high-performance liquid chromatography (HPLC)[64-68], ion chromatography (IC)[69, 70] and capillary electrophoresis (CE)[71], and the detection techniques include mass spectrometry[61], UV-VIS absorption[72] and hydride generation coupled with atomic fluorescence or absorption spectrometry (HG-AFS or HG-AAS)[73]. However, these popular analytical techniques have great limitations for arsenic speciation in biological matrices, since it is difficult to maintain the integrity of the arsenic species due to species transformation during sample preparation, separation, or detection[64, 74-76].

Surface-enhanced Raman spectroscopy (SERS) has been recognized as an advanced analytical technique for decades, owing to its unique advantages, e.g., fast and non-invasive detection and single-molecule sensitivity. The employment of SERS in arsenic detection has been reported recently, mainly with metallic nanoparticles[77-79] and metallic nanofilms[80-85] as substrates, while indirect detection methods use aptamers to boost the arsenic molecules selectivity[86, 87]. A review article regarding the recent advancements in arsenic detection based on SERS is available[88]. Though in theory, SERS could be used to carry out arsenic speciation using the unique fingerprint spectra of target compounds without chromatographic separation, difficulties were often encountered for the simultaneous measurement due to spectrum overlap. For example, two inorganic arsenic compounds (arsenite (As^{III}), arsenate (As^{V})) were able to be measured using SERS without significant spectrum overlapping[89]. However, two structurally similar organic arsenicals, monomethylarsonic acid (MMA^{V}) and dimethylarsinic acid (DMA^{V}), in silver colloidal suspensions could not be distinguished by SERS due to their similar Raman spectra, as reported in our recent work[90]. Therefore, when using SERS for speciation analysis, it is ideal to develop a separation method that minimizes the transformation of arsenic species and can be coupled to SERS, where SERS fingerprint signals and physical separation of arsenicals would provide a combined power for arsenic speciation.

The CRE refers to the occurrence of the ring-shaped stain left on a solid surface when a coffee drop is dried on the solid surface[1]. With the evaporation of liquid over the liquid drop surface, liquid from the center region would migrate towards the edge to replenish the loss of liquid, and the movement of liquid from the center to the edge is driven by capillary flow[1]. The CRE has been coupled with SERS measurements for the simplicity of operation to concentrate analytes towards the CRE region and to boost the detection sensitivity simultaneously[91, 92]. The CRE showed potential to separate nano/microparticles because different size particles have different accessibilities toward the contact line during the evaporation process[93, 94]. The results of these previous studies showed the potential application of using CRE as a simple platform for chemical separation/speciation.

Despite the absence of directly using the CRE for separation of small molecules, thin layer chromatography (TLC), a technique with a certain resemblance to CRE development, has been coupled with SERS for separation and detection of various analytes.

Recently, the TLC-SERS technique had been applied for the facile measurement of environmental pollutants[95], drugs[96, 97], and dyes[98]. The target analytes were usually eluted with a mobile phase and separated on a commercially available TLC plate. The analytes could be then detected by SERS after coating with silver/gold nanoparticles colloids serving as SERS substrates. Compared to TLC, the separation of analytes driven by the CRE without consumption of mobile solution offers shorter development times and would be more suitable for *in situ* analysis. It is, therefore, of our interest to use the CRE for separation of small molecules based on different interactions of the analytes with the surface and solvent, for being coupled to SERS for speciation analysis.

In this study, we explored a novel SERS method for arsenic speciation by combining the separation potential of the coffee ring effect on negatively charged silver nanofilms (AgNFs) and the Raman signal enhancement on AgNFs, through analysis of four common arsenic species, arsenite (As^{III}), arsenate (As^{V}), monomethylarsonic acid (MMA^{V}) and dimethylarsinic acid (DMA^{V}). Surfactants were introduced into the droplet to reduce the droplet surface tension and facilitate the migration of solution into the peripheral region of the droplet for enhanced separation[99-101]. Under the combined interactions of arsenicals with the AgNFs, solvent, and surfactant, arsenicals traveled different distances away from the drop center and they were partially separated on the AgNFs after drying the solution drop. Combining the SERS fingerprint signals and physical separation of arsenicals on the surface, arsenic speciation was achieved using the AgNFs substrate-based SERS technology.

2.3 Materials and Chemicals

Sodium metaarsenite, 98% (As^{III}), sodium arsenate dibasic, 99% (As^{V}), and cacodylic acid sodium salt, 98% (DMA^{V}) were obtained from Sigma-Aldrich (St. Louis, MO). Monosodium acid methane arsonate, 99.5% (MMA^{V}) was obtained from Chem Service, USA. Silver nitrate (99.99%) was purchased from STREM chemicals (Newburyport, MA). Sodium citrate dihydrate (Granular certified), NaOH, HCl, K_2HPO_4, and KH_2PO_4 were certified A.C.S grade or higher and purchased from Fisher scientific Inc. The phosphate buffer was prepared by mixing an equal volume of 0.2 mol L^{-1} of K_2HPO_4 and KH_2PO_4. Sodium dodecyl sulfate (SDS, 99.0%) and (3-Aminopropyl) trimethoxysilane (APTMS) were purchased from Sigma-Aldrich (St. Louis, MO). All solutions were prepared in deionized water (DI water) (18.2 MΩ, Barnstead Nanopure Diamond) unless with specific indication. All arsenic stock solutions were prepared in DI water at 13.3×10^{-3} mol L^{-1} (1000 ppm as arsenic atomic concentration). Glass microscope slides, purchased from Fisher Scientific (Pittsburgh, PA), were cut into 1×1 cm^2 pieces as glass substrates. Small size weighing boats were purchased from Cole-Parmer instrument (Vernon Hills, IL) and 25 ml clear glass vials with caps were purchased from Fishersci (Hampton, NH).

2.3.1 Instrumentation

The Raman spectrometer used was from Perkin-Elmer (Raman Station 400F), equipped with a diode laser operating system at 785 nm with an average power of 100 mW at the sample and 100-micron spot size. This Raman Station was equipped with the Raman Micro 300, which has a movable stage and a built-in camera monitoring the sample surface.

The laser source was focused on the sample on the stage through fiber optics cable connecting from the Raman Station 400F to the RamanMicro 300. Usually, the 20x optical lens was employed to get a better sample focus and Raman signal response. One piece of the silicon wafer was employed to calibrate the Raman system daily and the Raman signal intensity at 522 cm^{-1} was monitored to see whether the instrument was functioning normally. In a typical Raman spectrometer measurement, the optical lens was adjusted to obtain the best image of the sample surface before the measurement was performed. The SERS measurement parameters used were as follows, laser wavelength, 785 nm; exposure time, 1 second; and 4 exposures per measurement.

A Veeco multimode nanoscope III D atomic force microscope (AFM) was employed to obtain surface morphology of the prepared AgNFs and monitor the changes of surface morphology during the cleaning and salinization procedures. A transmission electron microscope (TEM, Hitachi, H-7650) was employed to study to the morphology of citrate coated silver nanoparticles. Malvern Zetasizer Nano-ZS (Westborough, MA) was employed to obtain the size and zeta potential of the nanoparticles synthesized in the laboratory. The average hydrodynamic diameters of the nanoparticles were obtained from the “Z-average” intensity peak as a function of size. UV-VIS absorption spectra of AgNFs were obtained from a Cary 300 UV-VIS spectrometer. All pH measurements were carried out on a Fisher Scientific Accumet Research AR15 pH/mV/°C Meter.

2.3.1 Fabrication and characterization of AgNFs

The fabrication process of AgNFs consists of two major steps, synthesis of citrate-coated silver nanoparticles (AgNPs-Citrate)[102] and immobilization of the AgNPs-Citrate onto glass substrates[103]. AgNPs-Citrate was synthesized by reducing silver nitrate with sodium citrate. Briefly, all glassware was emerged in Aqua Regia ($HCl/HNO_3 = 3:1$, v/v) overnight and then rinsed with a large amount of tap water and DI water, and finally dried in an oven at 80 °C before use. Then, a 250 ml round bottom flask with 50 ml of 1×10^{-3} mol L^{-1} silver nitrate was heated to boil in an oil bath under vigorous stirring with a condenser equipped to reflux. Sodium citrate solution (2 ml, 1% (w/v)) was added dropwise to the hot solution and kept boiling for 1 hour to yield a greenish-yellow AgNPs-Citrate colloidal suspension. Particle size and surface charge of the AgNPs-Citrate and pH of the colloidal suspension were obtained after the solution cooled down to room temperature.

For the process of immobilization of AgNPs onto glass substrates, all-glass substrates (about 1×1 cm^2) were soaked in Aqua Regia solution overnight and then sonicated successively in concentrated NaOH solution (2 mol L^{-1}) and HCl solution (2 mol L^{-1}) for 2 h. These glass substrates were thoroughly rinsed with a large amount of tap water and DI water to wash away excess acid or base. Finally, these glass substrates were dried in an 80 °C oven before use. Then, the AgNF was fabricated following a two-step procedure[103]. The first step was the silanization reaction on glass substrates surface to attach APTMS molecules catalyzed by a diluted acid[104]. APTMS solutions with different concentrations [0.5, 1.0, 2.5, 5.0 and 10.0% (v/v)] in anhydrous ethanol were first prepared. Then five pieces of glass substrates were soaked in a 25 ml glass vial containing

10 ml of APTMS solution and 100 µL of 1M HCl solution for 4 hours on an orbital shaker (150 rpm). After the silanization reaction, the glass substrates were cleaned with anhydrous ethanol under sonication for 3 minutes and repeated four times to remove loosely attached APTMS molecules on the glass surface. These treated glass substrates were then dried by nitrogen and heated in an oven at 80 °C for 30 minutes before the next step. The second step was to immobilize AgNPs-citrate onto the treated glass substrates. AgNPs-citrate were immobilized by electrostatic interaction with the glass surface since the amine groups were facing outwards and positively charged in the solution. The high-affinity interaction between silver nanoparticles and amine groups should further enhance the attachment[103-105]. Briefly, five pieces of glass substrates prepared from the first step were placed in a small weighing boat with no overlapping among the slides. Next, 5 ml of AgNPs solution was carefully transferred into a weighing boat and the glass slides were submerged in the solution for different periods (4, 8, and 24 h) on an orbital shaker (50 rpm). DI water was introduced to make up for the evaporation over time to prevent nanoparticles from aggregation. The resulting glass substrates were then cleaned with DI water three times, dried under N_2 gas, and stored in a freezer before use.

The prepared AgNFs were examined for SERS signal enhancement using As^{III} (1.33×10^{-3} mol L^{-1} (100 ppm as arsenic atomic concentration) in DI water) as a model arsenical, and the fabrication process of AgNFs was optimized to obtain sufficient enhancement for arsenic SERS signals. The optimization was focused on the concentrations of APTMS used in the silanization reaction and the immobilization times for AgNPs-citrate on the silanized glass surfaces. The AgNFs prepared by the optimized method was characterized by AFM to obtain surface morphology and AgNF thickness.

2.3.2 SERS fingerprint signals of arsenicals on the AgNFs

The typical fingerprint SERS signals of four commonly detected arsenicals including As^{III}, As^{V}, MMA^{V}, and DMA^{V} were measured individually in liquid droplets (0.1 mol L^{-1} potassium phosphate buffer, pH = 7.5) and on dry stain after drying out the liquid droplet. To do so, stock solutions of arsenic compounds (13.3×10^{-3} mol L^{-1} or 1000 ppm as arsenic atomic concentration) were diluted to 1.33×10^{-3} mol L^{-1} (100 ppm as arsenic atomic concentration) with 0.1 mol L^{-1} potassium phosphate buffer (pH = 7.5) as sub-stock solutions. Typically, 2 µL of arsenic solution from sub-stocks was dropped onto the AgNF, and SERS signals were collected randomly at the center region of the sessile droplet. After about 35 minutes of evaporation, the droplet was completely dry, and a ring-shaped stain was formed on the AgNF due to the coffee ring effect. The SERS signals were collected at the edge region of the stain, where the analytes should be most concentrated.

2.3.3 Arsenicals speciation on the AgNFs

Arsenic speciation on AgNFs was investigated by sequential addition of individual arsenic standards, starting from As^{V}, followed by DMA^{V}, MMA^{V}, and As^{III} to eventually have a mixture of the four arsenicals. To increase the separation, surfactant (0.05% of SDS) was added to the arsenic solutions with the purpose of extending the movement of the solvent on the surface. Arsenic standard solutions containing individual or mixed arsenicals of 1.3 × 10^{-3} mol L^{-1} (100 ppm) for each species were prepared in 0.1 mol L^{-1} phosphate buffer (pH=7.5) with 0.05 wt% of SDS. One drop (2 µL) of the solution was placed onto the AgNF surface and the sessile droplet was allowed to dry on a flat bench under ambient conditions. While the formation of only one-ring shaped stain occurs in a typical coffee ring phenomenon, two concentric-ring shaped stains were formed after drying the solution with SDS. Similar to the previous work of Brochard-Wyart et al[99, 100], the three-phase contact line did not move during the evaporation of sessile droplets containing surfactants, but the liquid in the sessile droplet permeated into the peripheral region of the sessile droplet. There was a clear boundary between these two concentric rings, named here the inner ring and outer ring, respectively. The diameters of inner and out rings were measured in multiple experiments and they ranged from 5.50 to 5.88 mm and from 3.45 to 3.90 mm, respectively, with relative standard deviations of 5-13% (**Table 1** and **Figure 2**). SERS measurements on all coffee drop stains were typically carried out from the center to the outer ring edge along the radius of the rings, and the sampling spots were performed with 100 µm increments according to the on-screen meter, and 10 µm inside and outside the ring boundary as well.

Table 1. The reproducibility of the coffee ring prepared onto AgNF with different sets of AgNPs.

AgNP set #	Nanoparticles size, nm (N=3)	The diameter of the coffee ring, mm (DMA^{V}) (N=3)			
		The inner ring, mm	Relative standard deviation,%	The outer ring, mm	Relative standard deviation,%
1st	50±5.3	5.73±0.66	11.51	3.45±0.35	10.14
2nd	48±4.5	5.88±0.78	13.26	3.70±0.30	8.10
3rd	53±6.5	5.50±0.30	5.40	3.90±0.50	12.82

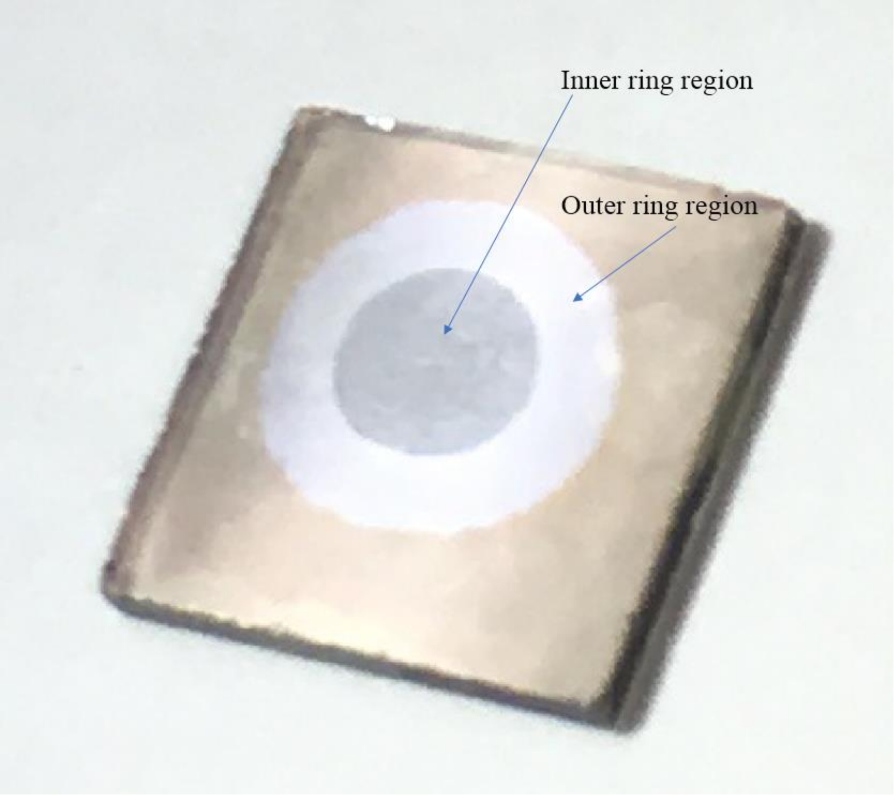

Figure 2. A typical image of the CRE (including the inner and outer rings) formed in this study.

2.4 Results and Discussion

2.4.1 Optimization of parameters for fabrication and characterization of AgNFs

Self-assembled metal colloid monolayer films have been widely used as SERS substrates. One method to prepare a stable nanofilm is to coat gold or silver colloid particles through chemical bonding on a polymer surface with pendent functional groups, such as $-NH_2$ or $-SH$. In this study, we firstly prepared AgNPs colloidal solutions, and then modified glass slides with APTMS for anchoring the AgNPs onto the surface to prepare

AgNFs. The pH of AgNPs-citrate colloidal solution was 9.0, and the surface of AgNPs was negatively charged with a zeta potential of -45.25 mV (**Figure 3**). Because the pKa value of primary ammonium ($-NH_3^+$) is greater than 10, APTMS was positively charged in the AgNPs colloidal solution[104]. Therefore, the positively charged surface can firmly bind with the negatively charged AgNPs to form stable AgNFs[104, 105].

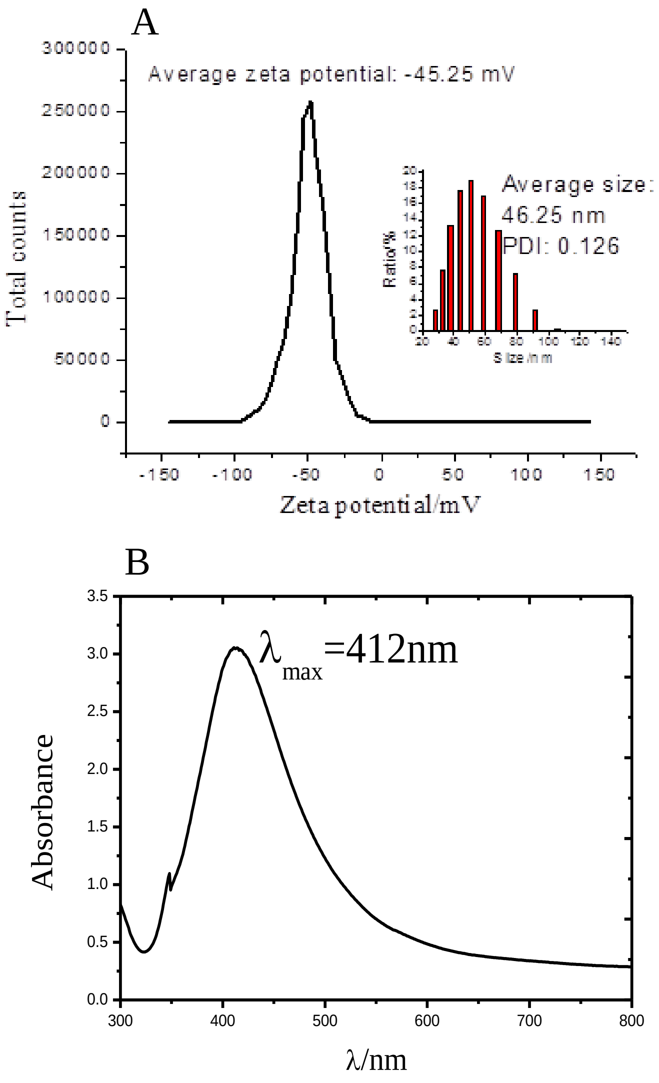

Figure 3. Properties of AgNPs-Citrate.

We first optimized the soaking time of ATPMS-modified glass slides in AgNPs-citrate solution (with 2.5% of APTMS) to get a sufficient SERS enhancement. The time of immobilization was selected as 8 hours in the later experiments for the sake of saving time and increasing signals. Further optimization on the immobilization time between 8 and 24 hours might provide a better point for balancing experimental time and signal enhancement, but was deemed not necessary at this stage for method development. No SERS signals were observed from the two control experiments, including the bare glass slide and the glass slide without APTMS treatment, and only hardly distinguishable signals were obtained by using 0.1% of APTMS. These results indicated that the AgNF serves as a critical substrate for signal enhancement and the silanization procedure is the prerequisite condition to the fabrication of AgNF. The signal intensities when using 0.5 to 10.0% of APTMS were similar, albeit varying slightly with minor baseline fluctuation. It is unclear why 2.5% of APTMS yielded the lowest signals, while both lower (0.5-1.5%) and higher (5.0-10.0%) concentrations produced higher signal intensities. It would be understandable if all concentrations higher than 2.5% resulted in lower signal enhancement, as the excessive amount of APTMS might be greater than monolayer formation on the SERS substrate surface and cause AgNPs aggregation. Although 0.5% of APTMS seemed to be sufficient for the treatment of glass The AgNF prepared with the optimized method was characterized by AFM. The glass surface was coated thoroughly, although the arrangement was not well organized. An TEM cross-section of the sample is shown in **Figure 4**. Ten random sections were selected to calculate the mean vertical distance in terms of the AgNF thickness, which was found to be 48.7 ± 6.7 nm (n=10). The size of AgNPs was about 44.6 ± 6.5 (n=9) nm according to the AFM image (**Figure 5**), suggesting that a monolayer film was formed. The minor size difference tween these two results should be originated from the surface roughness of glass slides. The average size of silver nanoparticles according to the TEM image was about 44.6 ± 6.5 (n=9) nm.

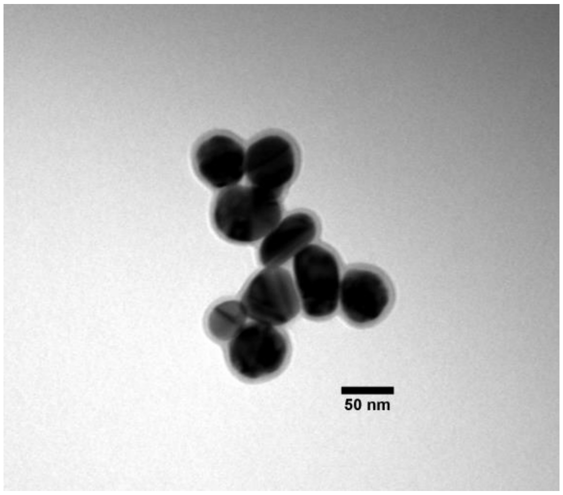

Figure 4. TEM image of silver nanoparticles.

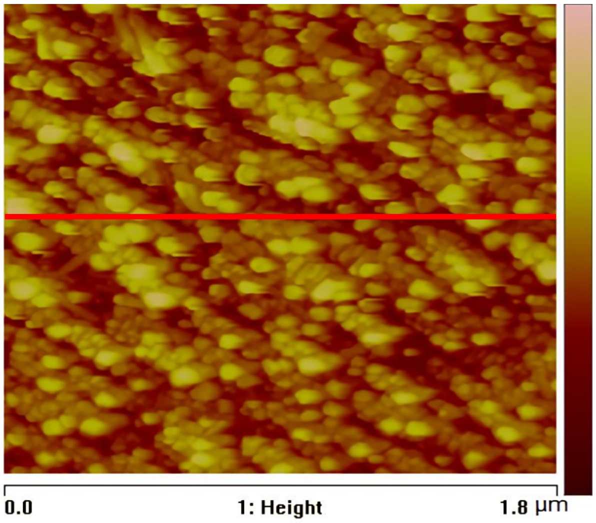

Figure 5. Typical surface morphology using AFM depth imaging.

2.4.2 SERS signals of arsenicals on the AgNFs

From the typical fingerprint SERS signals of As^{III}, As^{V}, MMA^{V}, and DMA^{V} measured in droplet and dry stain, significant interference from the buffer was not found in the Raman shift range of 1000~300 cm^{-1}. For each arsenical, similar wavenumbers of characteristic SERS signals were found between the droplet and dry stain (**Figure 6**). All signals in black curves were obtained at the center of a droplet containing 2 µL of 1.3×10^{-3} mol L^{-1} (100 ppm) arsenic in 0.1 mol L^{-1} potassium phosphate buffer (pH = 7.5).

For As^{III} (**Figure 6A**), a strong vibrational band at 730 cm^{-1} was observed in the droplet, resulting from the As─O stretch mode[106], and this characteristic vibrational band of As─O appeared at the same position after the sessile droplet dried completely. The band at 440 cm^{-1} in the droplet (shifted to 415 cm^{-1} in the dry stain) was not reported in the literature, and the vibrational mode of arsenite molecule at 440 cm^{-1} was tentatively interpreted as being the wagging of H─O bonds, with the assistance of computational chemistry. For As^{V}, fingerprint signals at 792 cm^{-1} and 782 cm^{-1} were observed in sessile droplet and on dry film, respectively, and these signals could be assigned to the As─O symmetric vibrations (**Figure 6B**)[107]. The superposition stretch of ν2 and ν5 of the arsenate molecule was not distinguishable in this buffer solution, which usually appeared around 400 cm^{-1}[107]. Similar SERS signal profiles were found for the two organoarsenicals. A vibrational band at 619 cm^{-1} due to the As─C stretch and one board vibrational band at 812 cm^{-1} from the vibrational band of As─O[108] were observed for MMA^{V} (**Figure 6C**). For DMA^{V}, the symmetric stretching of As─C appeared at 600 cm^{-1} since DMA^{V} has two As─C bonds, and the asymmetric As─O stretching was found at 830

cm^{-1} (**Figure 6D**)[82]. Based on the intensity of the characteristic signals on AgNFs, the strongest signal for each arsenical was selected as their fingerprint signal for speciation, and the wavenumbers of these signals were 730, 792, 619, and 600 cm^{-1} for As^{III}, As^{V}, MMA^{V}, and DMA^{V}, respectively.

Experiments were repeated multiple times separately to evaluate the reproducibility of the SERS spectra and signal intensities on different sets of AgNFs (prepared from different batches of AgNPs, but same sizes), the size effects of AgNPs on the formation of the coffee ring and SERS signal enhancement, and the variations of SERS signals with measuring times. It was demonstrated that the SERS spectra and signal intensities on different sets of AgNFs of the same size were highly reproducible.

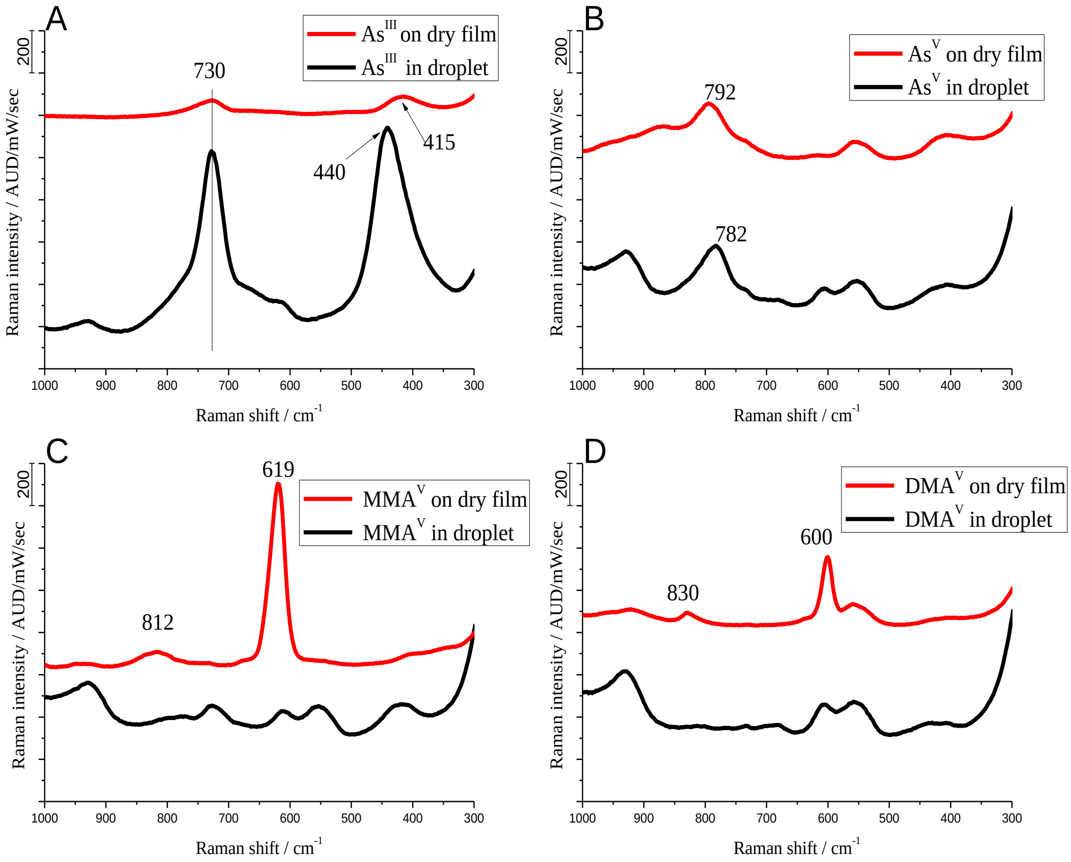

Figure 6. Typical SERS signal profiles of (A) As^{III}; (B) As^{V}; (C) MMA^{V}; and (D) DMA^{V} on the AgNFs.

While the characteristic wavenumbers were not significantly shifted, the signal intensities were found to be notably different in droplets and dry stains. Greater SERS enhancements on dry stains were observed for MMA^{V} and DMA^{V}. These organic arsenicals were negatively charged in the buffer, therefore it was difficult for them to get close to the negatively charged AgNFs to generate strong SERS signals in solution. Compared to solution droplets, stronger Raman signals were observed on dry stains because of the reduced distance to the AgNFs. The coffee ring effect also allows analytes in the droplet central area to travel to the edge with the solvent during the evaporation process, and the analytes can be concentrated in the drop stain area. Compared to the organic arsenicals, As^V and As^{III} showed an opposite trend in which the SERS signals were decreased on the dry film compared to in solution, especially for As^{III} with a significant signal decrease (**Figure 6A**). We speculated that this could be related to the As-AgNFs electrostatic interactions and the adsorption of arsenic species on AgNFs. For As^{III}, it remained in the neutral form in the buffer solution with little electrostatic repulsion or attraction by the negatively charged AgNFs, but it could be adsorbed on the nanoparticle surface (probably to the citrate molecules) via Van der Waals force. This adsorption would keep As^{III} staying close enough to the surface to generate strong SERS signals in the solution. For As^V in the buffer solution, although it was negatively charged and thus repelled by the AgNF, the adsorption through Van der Waals forces would to some degree offset the electrostatic repulsion, thus retaining As^V close to the surface for SERS signal enhancement. Since As^{III} was adsorbed on the AgNF (probably more strongly than As^V), it might not be able to move to the edge during the evaporation process and seemed to spread out in the stained area, causing the decrease in concentration at each spot. The appearance of signal for As^{III} at 730 cm^{-1} throughout the dry stain spot from the center to the edge, when examining the movement of As^{III} during drop evaporation, supported this notion (**Figure 7A**). Besides, the signal at 795 cm^{-1} was observed from the middle to the edge area (particularly at the edge of the ring) in the SERS profile of As^{III} in the dry stain, indicating the possible formation of As^V and thus causing the decrease in As^{III} signal. Such an oxidation reaction was reported in a previous study, in which more than 70% of As^{III} was oxidized to As^V in 1 mol L^{-1} of ammonium hydroxide solution after a 90 min TLC separation on cellulose plate[109]. It was suggested that the laser-excited surface plasmon resonance on the AgNPs played an important role in the oxidation reaction. The surface plasmon resonance can facilitate not only the activation of oxygen to form triplet oxygen molecules ($^3O_2$) but also electron transfer from AgNPs to the $^3O_2$ to create the anion of oxygen ($^2O_2^-$)[110]. The $^2O_2^-$ was then strongly adsorbed over the surface of AgNFs and AgO_2 was formed under a high temperature locally raised by the laser. Therefore, the resulting AgO_2 could oxidize As^{III} to As^V on the surface. The appearance of As^V was then confirmed in a SERS profile obtained by measuring the drop stain of As^V along the radius (**Figure 7B**), where As^V at 783 cm^{-1} was present in the outer ring area only.

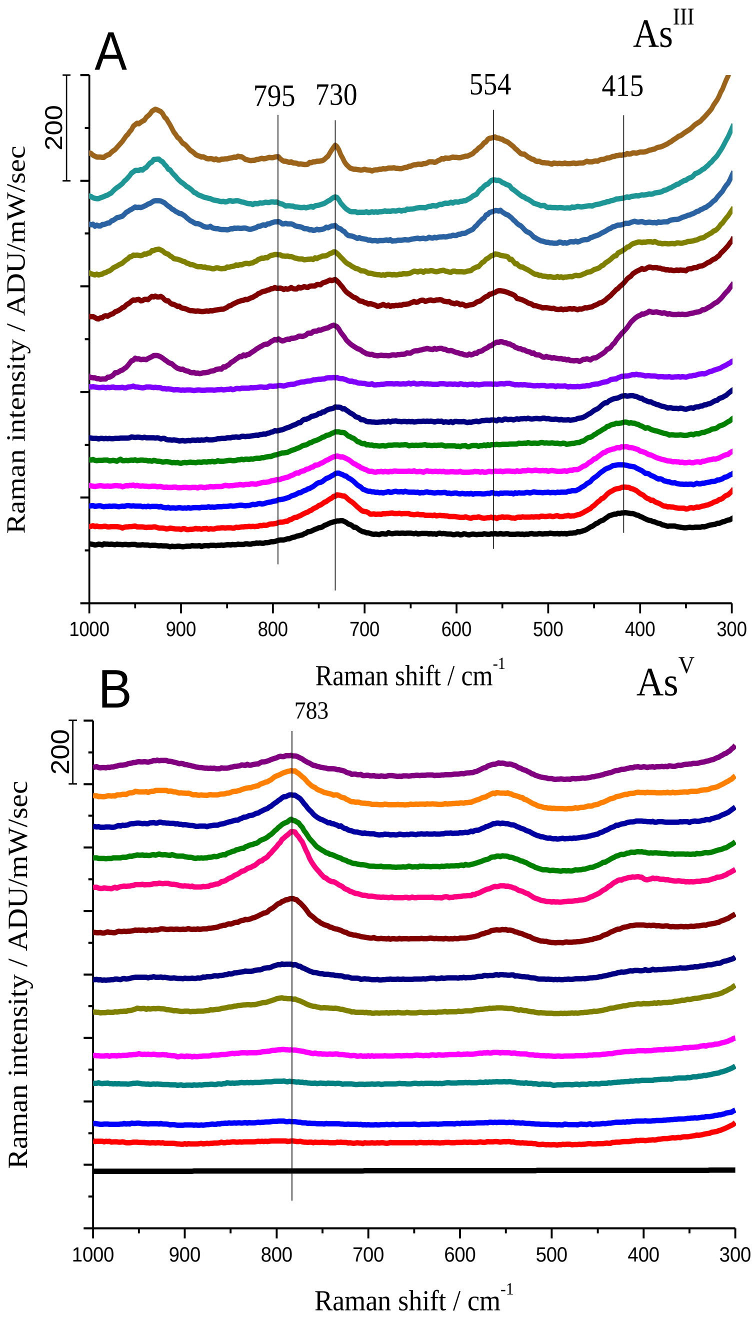

Figure 7. SERS signal profile of a drop stain after evaporation of 2 µL of 1.3 × 10^{-3} mol L^{-1} (100 ppm) (A) As^{III} and (B) As^{V} solution on the AgNF. Signals were collected along the radius of the drop stain from the center to the edge.

The results of examining SERS signals of the four arsenic species indicated that these arsenicals exhibited distinct signal profiles with fair SERS enhancement on the AgNFs. It was also observed that the arsenic compounds traveled different distances with the solvent during the evaporation process, and then deposited into different distribution patterns on the AgNFs. Taken together these results suggest that arsenic speciation could be potentially achieved by measurement of SERS signals along the radius of the ring stains.

2.4.3 Arsenic speciation on the AgNFs

Although these four arsenicals showed different fingerprint vibrational bands, the similarity of signal patterns from the two organoarsenicals caused a big problem for arsenic speciation analysis, according to our previous study by using the colloidal suspension of AgNPs as a SERS substrate[90]. Nanofilms, as an alternative substrate, could offer a great advantage due to the coffee ring effect occurring during the evaporation of the droplet. In addition to the preconcentration of the analytes, the coffee ring effect could facilitate the separation of arsenic species on the film due to the different interactions of arsenic with the substrate surface and the solvent. We thus used the AgNFs here for speciation of these four arsenicals, with the addition of 0.05% of SDS to extend the movement of the solvent and enhance separation of arsenicals on the surface. The addition of SDS did not show interference to arsenic fingerprint signals, but lowered the surface tension of droplets and indeed increased the travel distance of the solution, resulting in the formation of two concentric rings that could be helpful for species separation.

For As^V alone, the strongest signal at 783 cm^{-1} was found in the middle area of the outer ring, and there was no obvious signal in the inner ring area (**Figure 7B**). For the mixture of As^V and DMA^V, the fingerprint signals of As^V at 786 cm^{-1} were still only in the outer ring area (**Figure 8A**), but the DMA^V signals at 604 cm^{-1} were observed in the inner ring, demonstrating that As^V and DMA^V could be separated without any overlap. **Figure 8B** shows the speciation of adding MMA^V to the mixture of As^V and DMA^V on the AgNF. For As^V and DMA^V, their fingerprint signals, which were at 785 cm^{-1} and 604 cm^{-1} respectively, appeared in the same region as that in **Figure 8A**. There was a new peak appearing at 619 cm^{-1} in the outer ring, resulting from the addition of MMA^V. These results suggest that, even if the fingerprint signals of MMA^V and DMA^V were close to each other, speciation of MMA^V and DMA^V could be accomplished on AgNF because of the physical separation of these two species achieved using the coffee ring effect. Finally, the SERS profile of the mixture of As^{III}, As^V, MMA^V, and DMA^V was measured with a shortened distance of each sampling spot from the center to edge to avoid missing any fingerprint signals. The characteristic peaks at 608 cm^{-1}, assigned to DMA^V, was found in most areas of the inner ring and consistently observed in the inner ring region until the boundary (**Figure 8C**). When the sampling spots moved into the outer ring area, the peak at 618 cm^{-1} appeared and remained unchanged in the entire outer ring, indicating the presence of MMA^V. The fingerprint signal at 732 cm^{-1} appearing throughout the outer ring area can be assigned to As^{III}. Although the As^{III} signals on the AgNFs were weak due possibly to the oxidation to As^V, the peaks were still clear and distinguishable. It is worth noting that the As^{III} signals were not observed in the inner ring, different from the result for measuring As^{III} alone (**Figure 7A**), probably due to the enhanced movement by the addition of SDS.

The strongest As^{V} signals at 778 cm^{-1} were present in the middle of the outer ring, consistent with the results from the experiment for As^{V}, MMA^{V}, and DMA^{V} (**Figure 8B**). These results indicated the successful speciation of As^{III}, As^{V}, MMA^{V}, and DMA^{V} on the AgNFs, by combining the advantages of distinct fingerprint SERS signals and physical separation of arsenicals under the influence of the coffee ring effect.

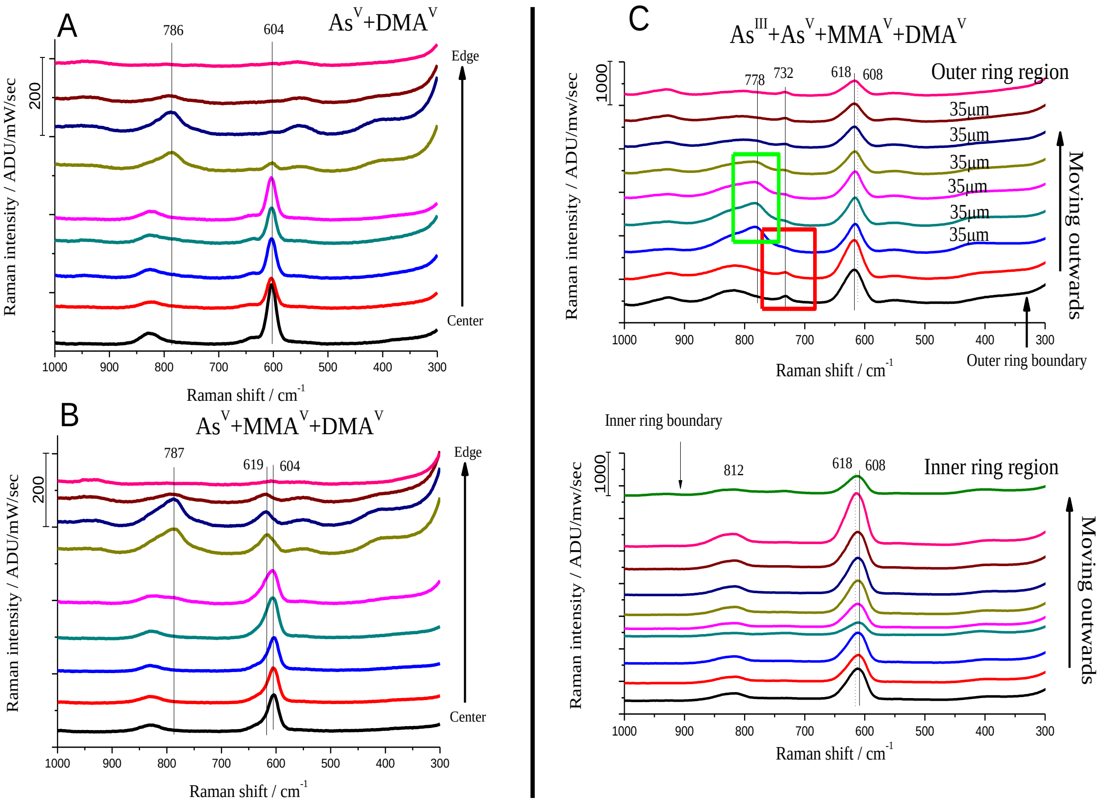

Figure 8. SERS signal profile of a drop stain after evaporation of 2 µL of 1.3 × 10^{-3} mol L^{-1} (100 ppm) (A) As^{V} and DMA^{V}, (B) As^{V}, MMA^{V}, and DMA^{V}, and (C) As^{V}, MMA^{V}, DMA^{V}, and As^{III} solution on a AgNF. Signals were collected along the radius of the drop stain from the center to the edge.

There was a significant difference between arsenic SERS profiles in the inner ring and the outer ring areas. The inner ring stain was formed by the coffee ring effect caused by an evaporation-driven capillary flow from the center of the droplet toward the contact line, while the outer ring stain was formed after adding a small amount of SDS containing buffer. The surfactant lowered the surface tension of the droplet, and consequently, the liquid could be slowly leaked out from the droplet because of capillary action caused by narrowly packed AgNPs surrounding the droplet. As a result, the arsenicals in a solution could move outward with the capillary flow to the edge of the droplet and then permeate into the periphery of the droplet with the solvent. AgNFs provided a negatively charged surface to interact with the analytes, playing an important role in the physical separation of arsenicals. For example, the strongest MMA^V signal appeared at the beginning of the outer ring, while DMA^V appeared in the edge of the inner ring (**Figure 8C**) because MMA^V (pKa = 3.6) bears more negative charges than DMA^V (pKa = 6.2) in the buffer (pH = 7.5)[111]. Surfactant could also affect the migration of arsenicals during solvent evaporation. Because of the coffee ring effect, SDS near the contact line was concentrated and the surface tension near the drop edge decreased. The difference in surface tension resulted in a Marangoni flow toward the center to push the analytes backward[112]. Most of DMA^V seemed to be trapped in the inner ring, possibly because the two methyl groups of DMA^V had a high affinity to the hydrophobic chain of SDS, leading to the deposition of DMA^V together with SDS in the inner ring area. On the contrary, MMA^V has one methyl group and should have a weaker interaction with SDS, and thus most of MMA^V was found in the outer ring area. Another factor in play here is the eluting ability of the solvent. The aqueous solution has a low eluting ability to less polar analytes such as DMA^V (in comparison to MMA^V)[113], and thus limits its migration. Under the combined interactions with the surface, SDS, and the solvent, DMA^V showed the shortest traveling distance.

2.5 Conclusion

A novel method for arsenic speciation was explored by utilizing AgNFs as SERS substrates, combing the distinct fingerprint SERS signals of arsenicals and their physical separation caused by the CRE on the AgNFs. To realize the possibility of using the CRE to separate small molecules, SDS as a surfactant was introduced, allowing varying travel distances for different arsenicals and thus successful speciation of As^{III}, As^V, MMA^V, and DMA^V. We demonstrated in this study the dual functions of AgNFs, as SERS substrates for signal enhancement and as a charged surface affecting analyte immigration. The capillary flow caused by the coffee ring effect also played a dual role, as it preconcentrated analytes into the ring edge area and meanwhile moved arsenicals to different distances on the AgNF surface. This is the very first study employing the CRE for arsenic speciation, and it does show the promising potential of the CRE for fast and *in situ* separation of small molecules. As the migration of analytes during evaporation is a complicated process controlled by various factors such as surface retention, capillary flow, and capillary action, future research will focus on understanding the role of these factors and further optimization of important factors for possible quantitative analysis of arsenic species.

Chapter 3. Speciation of thioarsenicals through application of coffee ring effect on gold nanofilm and surface-enhanced Raman spectroscopy

Part of this chapter was published in the journal Analytica Chimica Acta. Adapted with permission from Liamtsau, V., Fan, C., Liu, G., McGoron, A.J., Cai, Y., 2020. Speciation of thioarsenicals through application of coffee ring effect on gold nanofilm and surface-enhanced Raman spectroscopy. Analytica Chimica Acta, 1106: 88-95. Copyright (2020) Elsevier B.V.

3.1 Abstract

Thioarsenicals, such as dimethylmonothioarsinic acid (DMMTA^{V}) and dimethyldithioarsinic acid (DMDTA^{V}), have been increasingly discovered as important arsenic metabolites, yet analysis of these unstable arsenic species remains a challenging task. A method based on surface-enhanced Raman spectroscopy (SERS) detection in combination with the CRE for separation is expected to be particularly useful for analysis of thioarsenicals, thanks to minimal sample pretreatment and unique fingerprint Ramon identification. Such a method would offer an alternative approach that overcomes the limitations of conventional arsenic speciation techniques based on high-performance liquid chromatography separation and mass spectrometry detection. A novel analytical method based on a combination of the CRE and SERS was developed for the speciation of thiolated arsenicals. A gold nanofilm (AuNF) was employed not only as a SERS substrate but also as a platform for the separation of thioarsenicals. Once a drop of the thioarsenicals solution was placed onto the AuNF and evaporation of the solvent and the ring stamp formation onto AuNF began, the SERS signal intensity substantially increased from center to edge regions of the evaporated droplet due to the presence of the CRE. Through calculating the pKa's of DMMTA^{V} and DMDTA^{V} and accordingly manipulating the chemical environment, separation of these thioarsenicals was realized as they traveled different distances during the development of the coffee ring. The migration distances of individual species were influenced by a radial outward flow of a solute, the thioarsenicals-AuNF interactions, and a thermally induced Marangoni flow. The AuNF based CRE combined with SERS demonstrated a decent potential for the separation of arsenic species.

Keywords: Coffee ring effect; CRE; Gold nanofilm; Surface-enhanced Raman spectroscopy; Thioarsenicals

3.2 Introduction

Thioarsenicals, which contain an arsenic−sulfur bond analogous to their oxoarsenical counterpart with an arsenic−oxygen bond, have been increasingly discovered as a new class of arsenic metabolites in recent years[40, 59, 114]. Dimethylmonothioarsinic acid (DMMTA^{V}) and dimethyldithioarsinic acid (DMDTA^{V}) were widely detected in animal urine after exposure to various arsenic compounds, including dimethylarsinic acid (DMA^{V}) (**Figure 9**)[115].

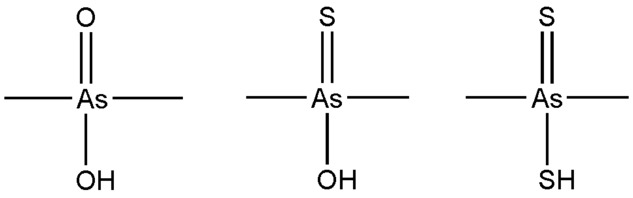

DMA^{V} DMMTA^{V} DMDTA^{V}

Figure 9. Thioarsenicals are analogous to the oxoarsenical counterpart.

Dimethylarsinothioyl glutathione (DMMTA^{V}(GS)), a conjugate of pentavalent arsenical DMMTA^{V} with glutathione (GSH), has been detected in cabbage *(Brassica oleracea)* after exposure to DMA^{V} and in human cell lines exposed to darinaparsin[58, 116]. After the introduction of DMA^{V} to *Shewanella putrefaciens*, DMMTA^{V} has been observed during arsenic biotransformation[117].

The generation of pentavalent thioarsenicals during As metabolism is of particular interest due to their ability to bind to the proteins in contrast to their oxygenated analogs. According to Pearson's hard/soft acid-base (HSAB) concept, pentavalent oxygenated As species are not likely to complex with proteins via interacting with thiol groups of peptides such as glutathione (GSH) and metallothioneins[58]. However, sulfur in thioarsenicals mitigates the hardiness of a molecule making it possible to bind to the proteins, possibly leading to higher toxicity. Previous toxicity tests confirmed that the toxicities of pentavalent thioarsenicals are similar to that of trivalent inorganic species (iAs^{III}) and are much higher than those of pentavalent oxygen-containing analogs, e.g., DMA^{V}[114, 118-122]. For instance, $DMMTA^{V}$ can bound to rat hemoglobin, illustrating that pentavalent As interacts with -SH groups of proteins and peptides[123].

Thioarsenicals appear to be among the key intermediates involved in arsenic metabolism due to their wide detection in biological samples post As exposure, the capability of binding to proteins, and potentially high toxicity[124]. Accurate speciation analysis of thioarsenicals has increasingly become demanding, albeit challenging. The speciation of thioarsenicals has been usually performed by high-performance liquid chromatography (HPLC) coupled with inductively coupled plasma mass spectrometry (ICP-MS) and/or electrospray ionization mass spectrometry (ESI-MS) methods[53-56]. However, there are some drawbacks associated with these conventional HPLC-ICP-MS or ESI-MS methods for the analysis of thioarsenicals. First, thioarsenicals are unstable species, and they could be decomposed at acidic pH and/or in the presence of oxygen during the extraction from biological samples[57, 60-63]. Second, species alteration may occur during the analysis, as observed in HPLC separation of thio-organoarsenate (2-dimethylarsinothioyl acetic acid), where the acidic mobile phase degrades the analyte momentarily, while a weak acidic solution makes it almost impossible to elute the analyte from the column[57]. Another problem with these conventional methods is the lack of precise structural information, as exemplified by the misidentification of DMMTA^{V} as DMA^{III} due to similar chromatographic properties[59]. Similarly, in the study of pentavalent thioarsenicals complexed with GSH, it is not conclusive from analyzing the ESI-MS data whether the thioarsenical is pentavalent (GSH directly bound to As through its cysteine unit) or trivalent (GSH bound through sulfur–sulfur bridge to As)[58].

Due to the drawbacks of currently available methods for the analysis of thioarsenicals, it is believed that inaccurate information (e.g., underestimation and/or speciation conversion) was associated with the analysis of thioarsenicals in previous studies. There is a need for a method that can provide researchers with detailed structural information and does not require extensive sample preparation for accurate analysis of thioarsenicals. We reason that a method based on surface-enhanced Raman spectroscopy (SERS) detection in combination with the CRE for separation could be particularly useful for analysis of unstable thioarsenicals thanks to minimal sample pretreatment and unique fingerprint Ramon identification. A CRE deposit forms through evaporation of solvent when a drop of liquid is placed on the solid surface[125]. The CRE has found its way in analytical applications, for the separation of particles and large biomolecules exploiting the size difference of analytes. Methods based on coupling the CRE with matrix-assisted laser desorption (MALDI) and Raman spectroscopy[92] were successfully applied for the separation and identification of different-sized particles[126], polymer-nanocrystal mixtures[127], and polycyclic aromatic hydrocarbons[37].

We previously applied SERS coupled with the CRE on silver nanofilms (AgNF) to speciate arsenite (As^{III}), arsenate (As^{V}), monomethylarsonic acid (MMA^{V}), and dimethylarsinic acid (DMA^{V}), four common, relatively stable arsenic species[128]. It is more important to apply SERS-based methods to the analysis of thioarsenicals, as they are unstable and could decompose when using conventional HPLC separation[57] and ESI-MS detection[58], which might be of the reasons why they have been detected only in recent years. We propose here to develop a more robust nanomaterials-based SERS analytical method for the detection of thioarsenicals, by considering the interactions of As species with the substrate surface and manipulating the CRE to facilitate the separation of thioarsenicals. As the information on the basic physicochemical properties of these compounds remains lacking, we calculated the pKa values of $DMMTA^{V}$ and $DMDTA^{V}$ and selectively adjusted pH in a way that $DMMTA^{V}$ and $DMDTA^{V}$ carried different charges and thus interacted differently with the surface during CRE formation for better separation. Although we previously reported the Raman spectra of some of thioarsenicals[129], we adjusted the theoretical calculations to the changing pH environment, considering that acidic or basic pH could considerably influence the Raman spectra of $DMDTA^{V}$. We used a gold nanofilm (AuNF) as the SERS substrate, not only to enhance an inherently wear Raman signal[24, 25] but also to avoid oxidation of thioarsenicals. Combining signature Raman spectra due to distinct chemical structures and properties and different migration distances of $DMMTA^V$ and $DMDTA^V$ in the CRE stain, we successfully differentiated these two thioarsenicals on AuNF-based SERS.

3.3 Experimental

3.3.1 Materials and chemicals

Cacodylic acid sodium salt, 98% (DMA^V), NaOH, HCl, Citric acid, Sodium citrate dihydrate (Granular certified), (3-Aminopropyl)trimethoxysilane (APTMS), glass microscope slides, weighing boats, and 25 ml glass vials were purchased from Fisher scientific Inc (Hampton, NH). The citrate buffer (pH=3) was fabricated by mixing Citric acid and Sodium citrate. All solutions were prepared in deionized (DI) water (18.2 MΩ, Barnstead Nanopure Diamond).

3.3.2 Instrumentation

The Raman spectrometer was obtained from Perkin-Elmer (Raman station 400F), which employed a diode laser at 785 nm with an average power of 100 mW. This Raman station was equipped with one Perkin-Elmer microscopy 300 with a portable stage and a camera to observe the sample surface. For optimizing resolving power, the 20 × optical lens focusing was acquired. A silicon wafer was employed to calibrate the Raman system at daily use and the Raman signal intensity at 522 cm^{-1} was monitored to check the reproducibility of the instrument. The SERS measurement parameters were laser wavelength, 785 nm; exposure time, 1 second; and 4 times of exposure per measurement. The AuNF surface was characterized by the Veeco multimode atomic force microscope

(AFM). Malvern Zetasizer Nano-ZS (Westborough, MA) was employed for the measurements of nanoparticles size (average diameter) and zeta potential. All pH measurements were carried out on a Fisher Scientific Research AR15 pH/mV/°C Meter.

3.3.3 Synthesis of thioarsenicals and determination of their respective Raman spectra

3.3.3.1 Dimethylmonothioarsenious acid (DMMTA^V)

DMMTA^V was synthesized according to the method reported by Cullen et al.[130] (**Figure 10A**). Briefly, DMA^V (2.76 g) and sodium $Na_2S * 9H_2O$ (7.60 g) was dissolved in 30 mL of water. Concentrated H_2SO_4 (1.70 mL) was added dropwise to the solution to make the molar ratio of Na_2S/H_2SO_4/DMA^V was 1.6:1.6:1. The reaction mixture was stirred for 1 hour and was extracted with ether and was dried over anhydrous Na_2SO_4. The ether was evaporated under N_2 and colorless crystals were formed. Raman spectra determined of both solid and liquid forms (citrate buffer solution, pH=3) of DMMTA^V were identical.

3.3.3.2 Dimethyldithioarsenious acid (DMDTA^V)

DMDTA^V was synthesized by two different methods. The first method for DMDTA^V synthesis was reported by Suzuki et al.[131](**Figure 10B**). Briefly, cacodylic acid (1.01 g) and Na_2S*9H_2O (4.27 g) were dissolved in water (15 ml), and concentrated H_2SO_4 (2.90 ml) was added. The molar ratio between components Na_2S/H_2SO_4/DMA^V was 7.5:7.5:1. The mixture was stirred for 3 hours, then DMDTA^V was extracted with ether and was dried over anhydrous Na_2SO_4. After ether evaporation under N_2 and colorless crystals were formed. Raman spectra determined of both solid and liquid forms (citrate buffer solution, pH=3) of $DMDTA^V$ were not identical, once a solid was dissolved into the citrate buffer, it formed a salt form that had a different vibrational fingerprint of As – S vibrations.

The second approach was reported by Fricke et al.[132](**Figure 10C**). Briefly, cacodylic acid (1.01 g) and NaOH (0.29 g) were dissolved in boiling ethanol (12.5 mL). Hydrogen sulfide was bubbled into the boiling solution for 30 min, and a white solid precipitated. After cooling, colorless crystals were isolated by filtration and air dried. Raman spectra determined of both solid and liquid forms (citrate buffer solution, pH=3) of $DMDTA^V$ (salt form) were identical.

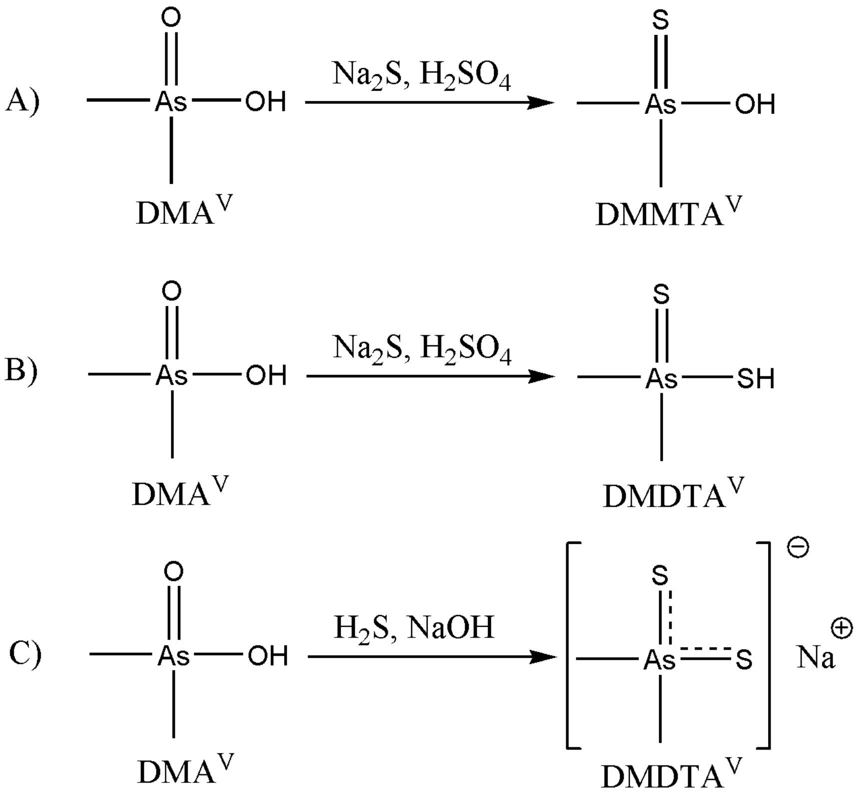

Figure 10. Synthesis of A) DMMTA^V, B) DMDTA^V (acid form), and C) DMDTA^V (salt form).

3.3.4 Theoretical calculation of Raman spectra of DMMTA^V and DMDTA^V

The theoretical calculation was completed employing Gaussian 09 at Florida International University's HPC facility. Firstly, MOLDEN visualization software[133] creates and optimizes the unique molecular vibrations for specific bonds at certain vibrational frequencies; Secondly, Multiwfn translates Raman signals from the data acquired from Gaussian output into Raman intensities, thus creating the simulated Raman graph for thioarsenicals[134]. Density functional theory (DFT) derived Raman spectra were measured by MOLDEN molecular simulation, while assignments from crystal Raman spectra were employed to verify MOLDEN assignments[135]. The results obtained with a hybrid functional B3LYP approach using the basis set 6-311++G** were proven by our research group[129] as a method that provides computational efficiency and precision in vibrational frequency prediction for computational spectra of oxygenated arsenicals, resulting in the lowest RMS value among other calculation methods tested.

The pKa's values of these thioarsenicals are important factors in determining their behavior on AuNF surface. If DMMTA^{V} and DMDTA^{V} would have pKa's that substantially differ from each other, it could be sensible to selectively deprotonate one of the thioarsenicals, leaving another uncharged. Depending on the differences in pKa's values of DMMTA^{V} and DMDTA^{V}, buffers will be used to manipulate the charges of thioarsenicals, making them have different charges. There were no reports with regards to their pKa's values[136], therefore a computational program was employed for the pKa's calculation. Marvin Sketch version 17.14 (ChemAxon Kft) was proven to perform reliable pKa's calculation based on the molecular structure of species[137, 138]. For example, calculated by this software pKa's of ibuprofen[139], ynamines[140], and CH-acids agreed with the literature value. Calculated pKa's value of inorganic pentavalent arsenic and methylated oxoarsenicals were consistent with the literature data[141, 142], as shown in **Table 2**.

Table 2. pKa's of arsenicals calculated by Marvin Sketch

Arsenical	Literature data	Calculated in this work
MMA^V	pKa_1= 4.10; pKa_2= 8.07	pKa_1= 4.20; pKa_2= 8.58
DMA^V	pKa = 6.20	pKa = 6.22
$DMMTA^V$	unknown	pKa = 4.37
$DMDTA^V$	unknown	pKa = 2.25

3.3.5 Fabrication of AuNF and application of coffee ring effect for individual identification of $DMMTA^V$ and $DMDTA^V$

The preparation of AuNF includes the synthesis of citrate-coated gold nanoparticles (AuNPs) and coating gold nanoparticles onto glass slides. AuNPs were fabricated by the reduction of chloroauric acid ($HAuCl_4$) with sodium citrate[102]. Briefly, the glassware was cleaned with Aqua Regia solution (HCl/HNO_3 = 3:1) overnight, then rinsed with DI water, followed by drying in an oven at 100°C. After heating 20 ml of 1×10^{-3} M $HAuCl_4$ chloroauric solution to the boiling point, sodium citrate (1 ml, 1%(v/v)) was introduced dropwise to this solution, and then refluxed for 30 min, following the production of red AuNPs colloidal suspension. The average size and zeta potential of AuNPs were 20 nm and -45 mV, respectively.

The fabrication of AuNF was performed by the silanization of the glass substrates, followed by the deposition of nanoparticles onto the silanized surface. AuNF was prepared according to the literature[143] with a slight modification of increasing the immersion time to 24 hours.

DMMTA^V and DMDTA^V solutions 100 ppm solutions of thioarsenicals were prepared by dissolving thioarsenicals in citrate buffer (pH=3). Immediately after preparation 2 µL of DMMTA^V and DMDTA^V citrate buffer solution was deposited onto AuNF. Once the droplet was completely dried and a ring-shaped stain was formed on the AuNF, SERS signals were measured from center to edge regions of the ring stain.

3.4 Results

3.4.1 Comparison of experimental and theoretically calculated Raman spectra of DMMTA^V and DMDTA^V Raman spectra

DMMTA^V (solid/liquid form) Raman spectra exhibits three major vibrational modes observed at 469 cm^{-1}, 611 cm^{-1} and 643 cm^{-1}. These represent As = S stretch, symmetric vibrational mode of C – As – C, and asymmetric vibrational mode of C – As – C respectively[144] as in **Figure 11A**.

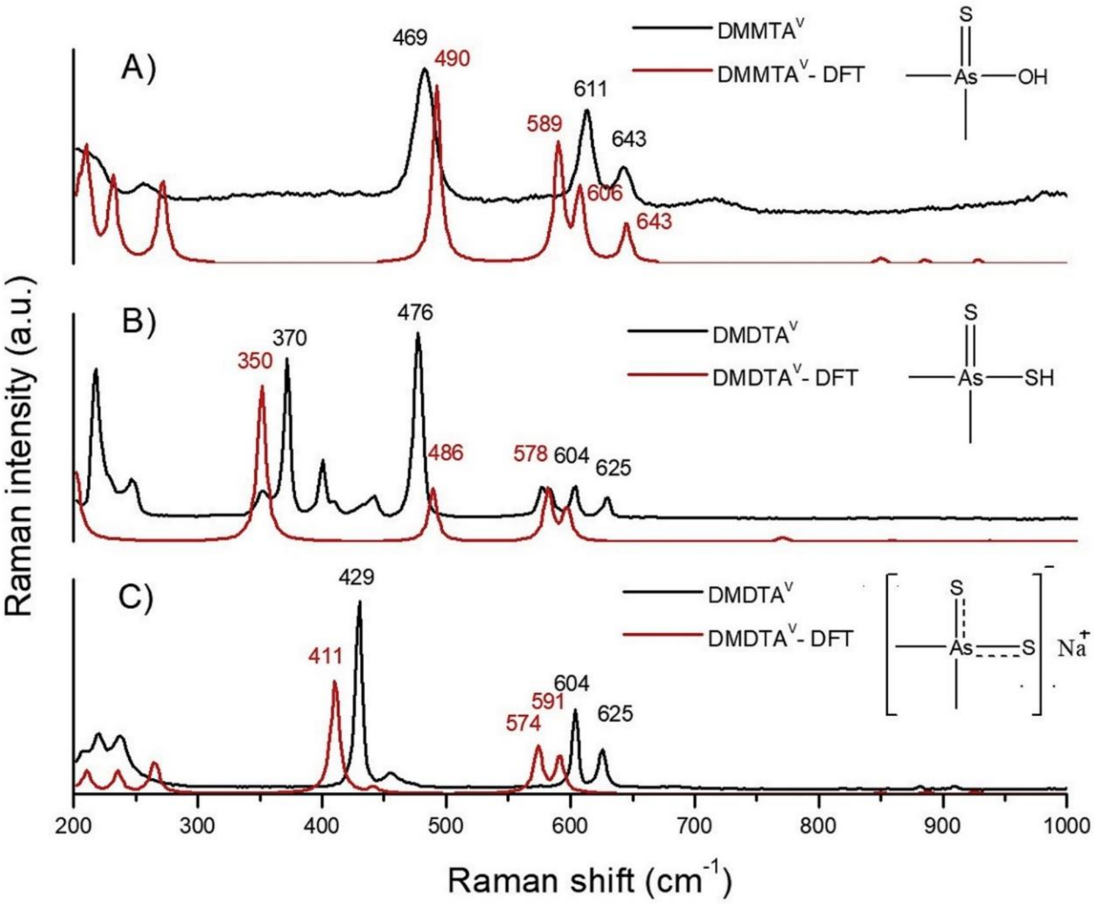

Figure 11. Raman spectra (experimental and theoretical) of A) DMMTA^V, B) DMDTA^V (acid form) and C) DMDTA^V (salt form).

DMDTA^V in acid form (solid/liquid form) was synthesized by Method #1[131], showing two major bands (**Figure 11B**) represented by As – S stretch at 370 cm^{-1} and As = S stretching at 475 cm^{-1}[145]. Other vibrations are associated with the C – As – C symmetric mode (573, 601 cm^{-1}) and C – As – C asymmetric mode (625 cm^{-1}) respectively[146].

The Raman spectra of DMDTA^V(salt form), synthesized using Method #2[132] (**Figure 11C**) shows three major arsenic vibrational bands at 429 cm^{-1}, 604 cm$^{-1,}$ and 625 cm^{-1}. However, in contrast to the three As – S vibrations of DMDTA^{V} synthesized by Method #1, there is only one As – S (429 cm^{-1}) band represented by delocalized distribution π-electron cloud over S – As – S fragment in dimethyldithioarsinato anion[145],[147]. The bands at 604 cm^{-1} and 625 cm^{-1} are symmetric and asymmetric C – As – C vibrations, respectively[144]. Notably, after the addition of the NaOH to the acidic form of DMDTA^{V}, the salt form occurred. Following this neutralization reaction, vibrational modes of As – S (370 cm^{-1}) and As = S (476 cm^{-1}) bands in the acidic form of DMDTA^{V} merged into the delocalized π-electrons bond in the salt form of DMDTA^{V} having the main signal at 429 cm^{-1}. The salt form of DMDTA^{V} is readily soluble in water in comparison to the acidic DMDTA^{V}[145].

3.4.2 Identification of individual DMMTA^{V} and DMDTA^{V} using AuNF-SERS

The difference between the Raman spectra of DMMTA^{V} (citrate buffer solution) and DMMTA^{V} (adsorbed onto AuNF) was observed during SERS measurements. Indeed, the wavelength red shift occurred for all DMMTA^{V} vibrational frequencies, namely: from 469 cm^{-1} to 464 cm^{-1} for As=S stretching, from 611 cm^{-1} and 643 cm^{-1} to 594 cm^{-1} for As – C symmetrical and asymmetrical stretching's respectively (**Figure 12A**)[148]. The probable reason for this is the partial adsorption of DMMTA^{V} onto AuNF surface, following a charge transfer effect between the AuNF surface and DMMTA^{V}. This most intense SERS signal of As=S vibration at 464 cm^{-1} has been chosen for tracing DMMTA^{V} across the coffee ring deposit. Regarding DMMTA^{V} migration behavior, there was an increase in SERS intensity (As=S) from the center to middle regions, however, despite the coffee ring effect, the decrease in SERS signal occurred in the edge region. Similar to the DMMTA^V, the Raman spectra of DMDTA^V vary greatly from the DMDTA^V – AuNF. Due to the charge transfer effect, all DMDTA^V shifted to the red region: from 429 cm^{-1} to 410 cm^{-1} for π-delocalized S – As – S stretching, from 604 cm^{-1} and 625 cm^{-1} to 591 cm^{-1} for As – C symmetric and asymmetric stretching respectively (**Figure 12B**). A typical coffee ring phenomenon (an increase of SERS intensity from the center to edge regions) was observed for DMDTA^V deposition onto AuNF surface. Indeed, the SERS signal of S – As – S stretching at 410 cm^{-1} increases from the center to the edge region.

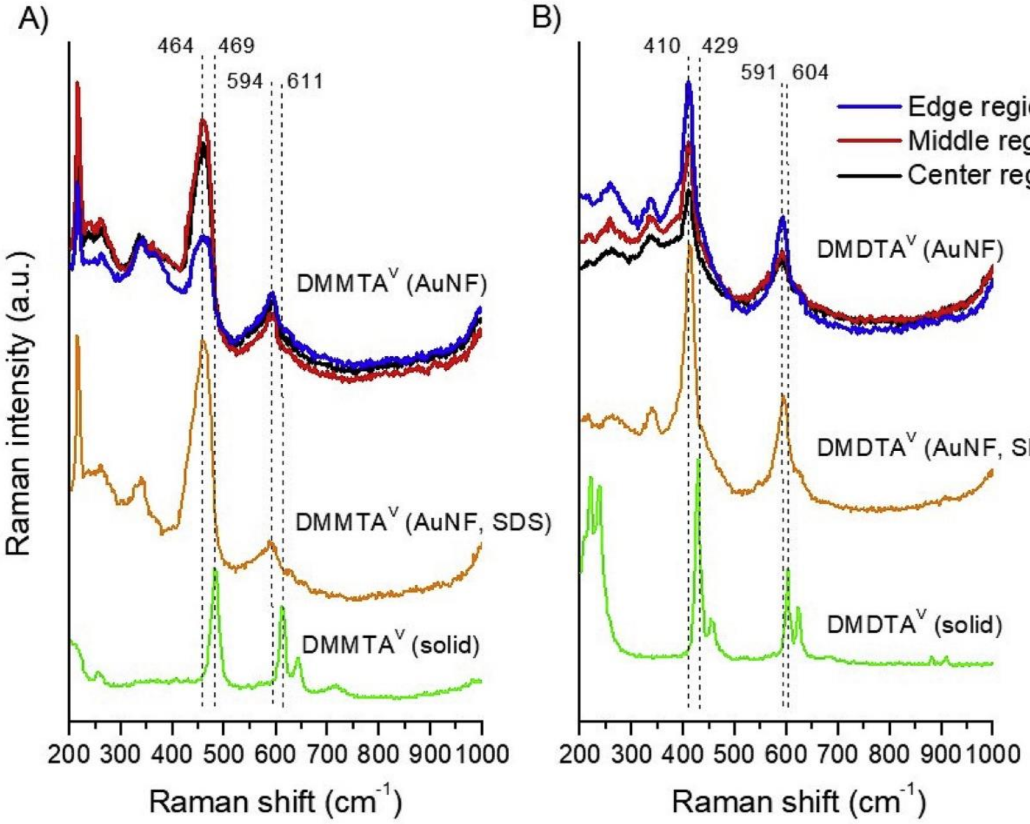

Figure 12. The coffee ring – SERS of 100 mg L^{-1} A) DMMTA^V and B) DMDTA^V onto AuNF.

3.4.3 Application of the coffee ring effect on AuNF surface for separation and identification of DMMTA^V and DMDTA^V

As for individual thioarsenicals adsorbed onto AuNF, the mixture of DMMTA^V and DMDTA^V also demonstrated a similar red shift for all vibrational modes (**Figure 13**). For DMDTA^V from 429 cm^{-1} to 412 cm^{-1} (S – As – S stretching), from 604 cm^{-1} and 625 cm^{-1} to 596 cm^{-1} for As – C symmetric and asymmetric stretching respectively. Regarding DMMTA^V, As=S vibrational frequency shifted from 469 cm^{-1} to 465 cm^{-1}, As – C from 604 cm^{-1} to 596 cm^{-1} respectively. For the separation part, the SERS signal of DMDTA^V increased constantly from the center to edge regions, in contrast to the DMMTA^V, which was decreasing across the ring stain. The broad SERS signal at 276 cm^{-1} was attributed to the Au-citrate vibrational stretching, indicating the presence of citrate coated gold nanoparticles onto the nanofilm surface[149].

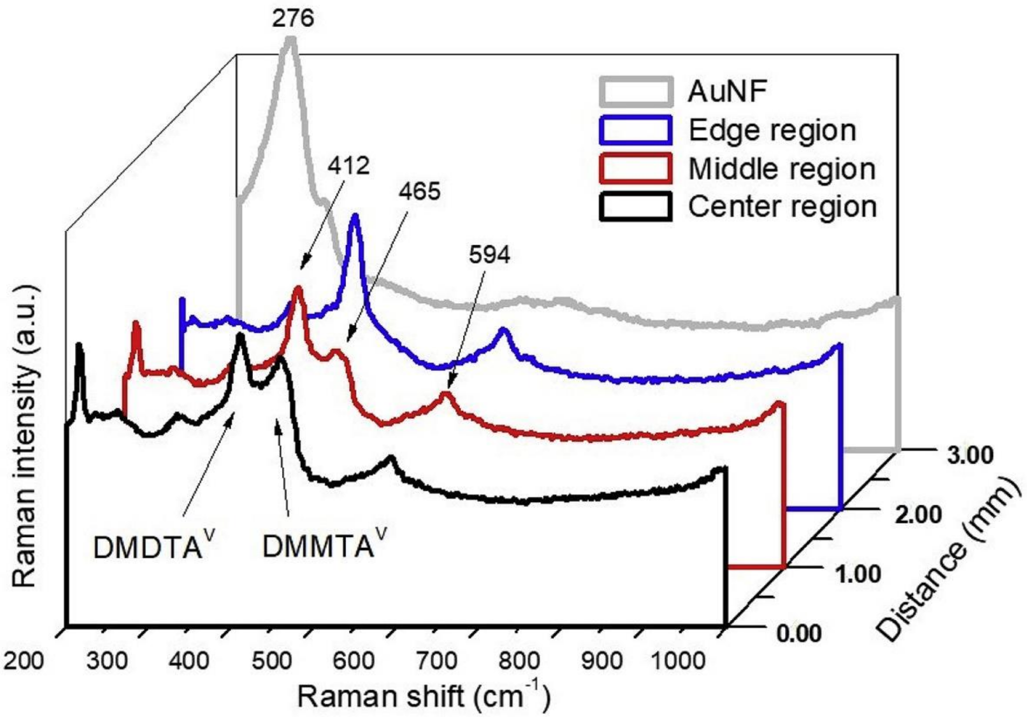

Figure 13. The CRE – SERS of 100 mg L^{-1} $DMMTA^V$ and $DMDTA^V$ onto AuNF.

3.5 Discussion

Generally, the CRE is created by reducing the surface tension of the sessile droplet and enhancing the capillary action generated by closed packing nanoparticles at air, solid, and liquid interphase[1]. In a CRE, a drop of a liquid is placed on AuNF surface, and as the solvent begins evaporating, the liquid is driven to the edge of the evaporating droplet by a radial outward flow.

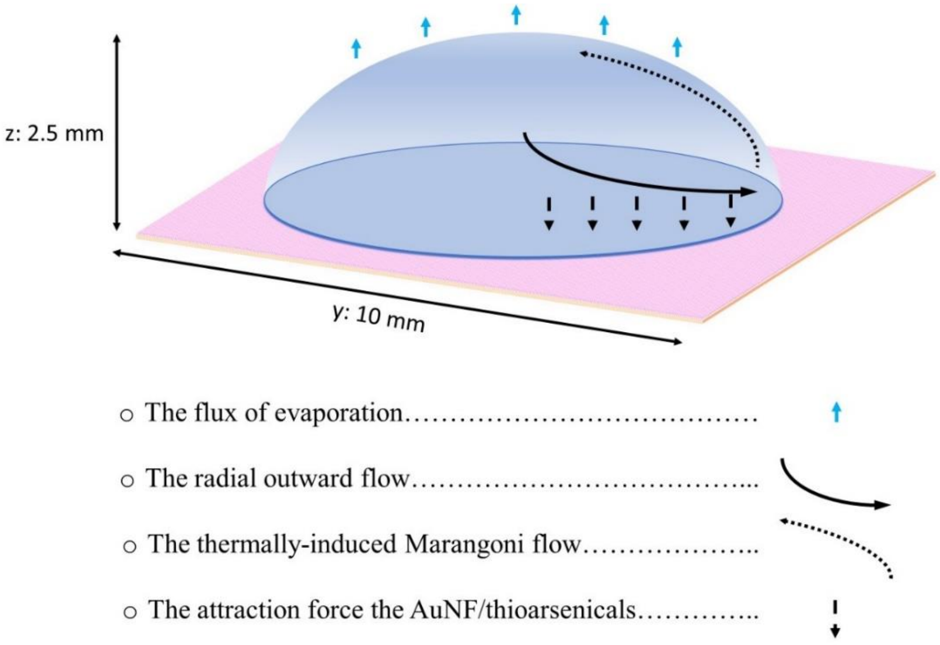

Figure 14. The diagram illustrating the processes influencing the CRE deposit formation.

The key structural element of the developed method is nanofilm. This functioned not only as a surface for separation but also as a SERS substrate. Indeed, silica surfaces coated with nanoparticles are among typical SERS substrates and they are usually used only for the amplification of Raman signal[150, 151]. However, it is possible to use them as a stationary phase for chromatographic separation because of their strong resemblance to the ion exchange TLC plates. Indeed, the surface of the SERS substrate has negative or positive charges depending on the method of preparation of nanoparticle colloidal solution. pKa could influence the charges of thioarsenicals in the buffer solution causing a difference in migration distances for each thioarsenical during the formation of the CRE. The calculated pKa's for DMMTA^{V} and DMDTA^{V} were 4.37 and 2.25, respectively. According to these results, citrate buffer (pH=3.0) was used to selectively deprotonate the sulfhydryl group of DMDTA^{V}. Since charged and neutral species would have distinct interactions with negatively charged SERS surface, their traveling distances could be different. It is expected that negatively charged DMDTA^{V} could preferentially stay in the inner ring of the dried droplet because of the strong interaction with AuNF surface in contrast to neutral DMMTA^{V} that has lesser AuNF surface attraction and would be driven by radial outward flow from the center to the edge. The CRE regions are illustrated in **Figure 15**.

In a previous study[152] we used AgNF to separate four major oxoarsenicals (As^{III}, As^{V} , MMA^{V}, DMA^{V}) based on their distinct pKa's values. The CRE was evident upon introducing arsenicals onto AgNF surface because the SERS signal intensity of individual species increases from the center to the edge of the evaporated droplet. MMA^{V} and DMA^{V} were present across AgNF, in contrast to the As^{III} and As^{V} that traveled long distances and were detected in the outer region. This indicates that oxoarsenicals interact with the AgNF surface differently, and we attempted to extrapolate this method for the speciation of thioarsenicals, however, no SERS signal of the arsenic-sulfur bond was found onto AgNF, only DMA^{V}. It was assumed that AgNPs can catalyze the electron capture by O_2 resulting in the formation of the anion of oxygen ($^{2}O_2^{-}$)[153]. Also, the AgO_2 could be formed under the laser irradiation, oxidizing As-S to As-O onto the AgNF surface. Indeed, the vibrational fingerprint of Ag-$^{2}O_2^{-}$ and AgO_2 was found on the AgNF surface. Thus, AgNF was not suitable for easily oxidizable species and we opted for the more inert and biocompatible gold nanofilm (AuNF)[154].

Considering the application of the CRE for the separation of DMMTA^{V} and DMDTA^{V}, the formation of the coffee ring deposit was influenced by three major factors: the radial outward flow, drawing the thioarsenicals from the center to the edge of the evaporating droplet; attractive/repulsive interactions between thioarsenicals and AuNF that mainly govern the adsorption of thioarsenicals onto AuNF; and thermally induced Marangoni convection that reverses the solute movement as opposed to the radial flow and promotes the deposition of thioarsenicals in the center region.

The first factor that affected the CRE deposit formation is the radially outward flow. The construction of a CRE stain begins as a droplet placed onto the AuNF and solvent (water) evaporation initiates (**Figure 14**). The radial outward flow transfers the liquid to the wetting contact line of the drying drop to replenish the solvent that vanishes during evaporation, thus, initially driving both $DMMTA^V$ and $DMDTA^V$ out of the center to the edge region. The evaporation velocity is linearly proportional to the height of the evaporating droplet and inversely proportional to the total evaporation time[155]. The height of the droplet, which is radius-dependent, accounted for 2.5×10^{-3} m. The total evaporation time of 2 µL droplet is 30 min, thus the calculated evaporation velocity throughout drying was 5×10^{-2} mg/min (data not shown). Moreover, the radial outward flow is linearly related to evaporating flux[156] and inversely proportional to the viscosity of the solution[17]. In previous studies, the radial outward flow considerably affected the separation of particles of various sizes[126, 157], however in the case of small molecules as an example of thioarsenicals, which size are negligibly small, the radial flow itself is assumed to equally affect their velocities and, thus traveled distances.

The second factor is the attractive/repulsive forces between the thioarsenicals and AuNF that influenced the adsorption of thioarsenicals onto AuNF. As $DMMTA^V$ and $DMDTA^V$ mixture drove to the edge of the droplet by the radial flow, thioarsenicals begins to interact with the AuNF surface. At pH=3 the AuNF surface displays a negative γ surface potential because the major surface constituents are H_3Citrate and H_2Citrate$^-$ that stabilizes the outer layer of AuNPs onto the AuNF surface[158]. It is widely recognized that thiols and sulfur-containing ligands can substitute the citrates onto the surface of the nanoparticles [159-162]. Besides, pH determines the dissociation of thioarsenicals in the solution, thus leading to the distinct adsorption constants, such as negatively charged thiolates are much more active nanoparticle substituents than neutral thiols, the binding energies of neutral thiols is 3-4 times smaller than that of thiolates[163]. Another factor that must be considered is the effect of the electron density delocalization across the arsenic sulfur-containing active binding site of thioarsenicals, which may lead to substantial Raman shifts upon adsorption onto AuNF. The importance of this phenomenon was demonstrated upon the aromatic thiols adsorption onto AuNP that exhibits gigantic Raman shifts due to the d-electron transitions[164].

As soon as the mixture was deposited onto AuNF surface, DMDTA^V immediately anchors onto AuNF replacing the citrate ligand at the nanofilm surface leading to the remarkable red shift from 429 cm^{-1} to 412 cm^{-1} (**Figure 13**) for the delocalized π-electrons bond in DMDTA^V salt form. Because of the strong attraction between DMDTA^V and AuNF, the DMDTA^V predominantly occupied the inner region. Exploiting the delocalization effect across S – As – S binding site is the major reason why we intentionally manipulated pH in the way to ionize DMDTA^V, thus in this form of DMDTA^V has a substantially higher affinity to the AuNF surface than the neutral DMDTA^V. Even though for the individual DMDTA^V the coffee ring effect was detected: the radial outward flow has driven some of DMDTA^V to the edge, in the mixture the DMDTA^V's behavior was different, representing its uniform distribution across AuNF. As a result, the SERS signal intensity of DMDTA^V was relatively constant from the center to the edge due to its immediate adsorption onto the AuNF surface by substituting citrate that stabilized AuNPs.

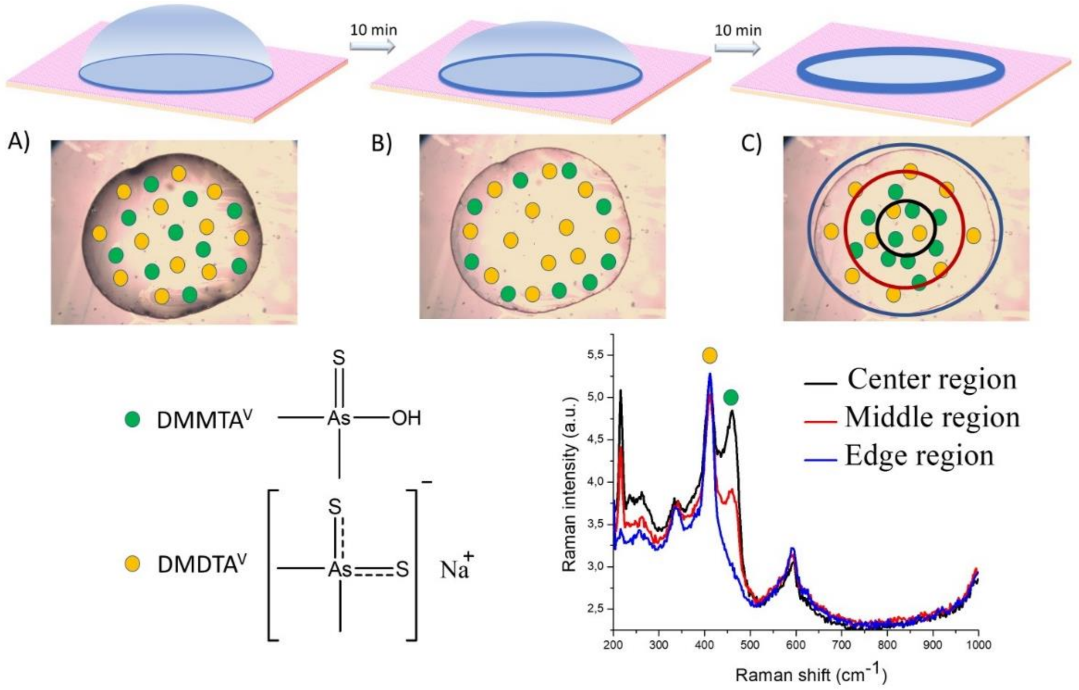

Figure 15. The formation of the CRE: analysis of thioarsenicals traveled mode. Phase A) A 2 µL drop contained 100 mg L^{-1} DMMTA^V and DMDTA^V (citrate buffer solution, pH=3) is placed onto the AuNF surface.

In contrast to the ionized form of DMDTA^V, we selectively left DMMTA^V neutral, consequently, it initially traveled a long distance across the drying droplet because it has not been attracted to the AuNF surface as much as DMDTA^V, thus facilitating the separation between thioarsenicals. For DMMTA^V, the SERS signal intensity at 464 cm^{-1} (As=S symmetric stretching) was decreasing from the center to the edge indicating that neutrally charged DMMTA^{V} has not been as strongly retained onto the AuNF surface as DMDTA^{V}. As a result, DMMTA^{V} was more affected by the radial flow than DMDTA^{V}, and was driven to the edge region. Considering the interaction between DMMTA^{V} and AuNF, the red shift occurs from 469 cm^{-1} to 465 cm^{-1} due to the charge transfer effect between its molecule and the AuNF surface[165]. However, in contrast to DMDTA^{V} the SERS shift was significantly smaller, 17 cm^{-1} for DMDTA^{V} and 4 cm^{-1} DMMTA^{V} respectively. This data provides evidence that DMMTA^{V} has a lesser affinity to the AuNF and has not been adsorbed as much as DMDTA^{V}. Another evidence for the adsorption of the thioarsenicals onto AuNF surface can be drawn from the appearance of the Au – S vibrational stretching at 267 cm^{-1}[166].

The third key factor is the thermo-capillary Marangoni flow that drives the liquid back to the center of the drop[156, 167, 168]. During the evaporation of the drying droplet, the thermally induced Marangoni flow carries out thioarsenicals back from the edge to the center region, however, DMDTA^{V} having higher affinity to the AuNF than DMMTA^{V}, was preferentially deposited in the edge region in contrast to the DMMTA^{V}, which was transferred back to the center of the evaporating drop. As a result of the predominant repulsion/attraction interaction over radial flow and Marangoni convection, DMDTA^{V} was deposited uniformly from the center to the edge of the evaporating droplet[17]. Indeed, the temperature profile increases from the center to the edge of the droplet deposited onto the flat surface, meaning that the thermal field gradient in the drop varies considerably as evaporation proceeds[169], might be resulting in the reverse direction of Marangoni flow that drives DMMTA^{V} back from the edge to the center region[156].

Overall, considering all three factors, it can be concluded that outward radial flow initially drives the analytes to the edge of the drying droplet, at that region DMDTA^V interacts stronger with the AuNF, considering substantial Raman shift (17 cm^{-1}) in contrast to this of DMMTA^V (4 cm^{-1}) (**Figure 13**). Then, thermally-induced Marangoni flow reverses the movement of both analytes affecting the deposition of DMMTA^V that eventually was detected in the center of the droplet, whereas DMDTA^V was anchored gradually across AuNF providing a relatively constant SERS signal of S÷As÷S stretching at 412 cm^{-1} (**Figure 13**).

3.6 Conclusion

The CRE coupled with SERS is an alternative technique for the separation and identification of thiolated arsenicals. The separation was achieved due to the combination of three mechanisms influencing the formation of CRE deposits: radial outward flow, attraction/repulsion interactions between the AuNF and thioarsenicals, and the thermally induced Marangoni flow. The AuNF was employed not only for separation via the CRE but also as a substrate for SERS identification. The separation employing the CRE can be manipulated not only by varying pH that controls the interactions between AuNF and analytes achieving different travel distances, but also by tuning nanoparticles size, droplet volume, and other parameters. Overall, the combination of the CRE and the detection method such as SERS is a promising technique for the speciation of thiolated arsenicals. This work will significantly expand the nanofilm application for speciation analysis concerning speciation of unstable and easily oxidizable species. Separation by the CRE in mild condition coupled with the nondestructive SERS detection method is a powerful tool for the speciation of small molecules.

Chapter 4. Chromatographic framework for coffee ring effect-driven separation of small molecules in surface-enhanced Raman spectroscopy analysis

Part of this chapter has been submitted to the journal Analytica Chimica Acta for publication, as the following manuscript: Liamtsau, V., Liu, G., Alexander, M., Mebel, A., Cai, Y., Chromatographic framework for coffee ring effect-driven separation of small molecules in surface enhanced Raman spectroscopy analysis.

4.1 Abstract

The applications of the coffee ring effect (CRE) in analytical chemistry have been increasingly expanded from particles and macromolecules to small molecules, in particular, coupled to surface-enhanced Raman spectroscopy (SERS). Herein, we have developed a theoretical framework to describe the CRE-driven separation process of small molecules, using SERS analysis of dimethylarsinic acid (DMA^V), dimethylmonothioarsinic acid ($DMMTA^V$), and dimethyldithioarsinic acid ($DMDTA^V$) on gold nanofilm (AuNF) as an example. By combining the CRE theory for the radial flow and the Extended Derjaguin-Landau-Verwey-Overbeek (XDLVO) theory for mass transfer between solution and AuNF surface, we adapted the conventional chromatographic theory to derive a modified van Deemter equation for the CRE-driven separation. By using this model, we predicted the travel distances of arsenicals based on the different affinity of analytes to the AuNF and evaluated the possibility of separation of unknown analytes by CRE-based SERS, demonstrating the successful adaptation of classic chromatographic theory to CRE-driven nanochromatography.

Keywords: Coffee ring effect, Gold nanofilm, XDLVO, Raman spectroscopy, arsenic, nanochromatography

4.2 Introduction

The evaporation process of a sessile droplet containing suspended or nonvolatile particles normally leads to a ring-shaped formation on a flat substrate. These stains are produced by CRE that has been firstly explored by Deegan et al.[1], where the author described the transport of solid particles to the edge of the drying droplet during the solvent evaporation. To replenish the solvent loss at the three-phase contact line, the radial outward flow was generated from the center to the edge regions of the evaporating droplet[1, 125, 170]. The major application of CRE was commonly attributed to the enrichment and separation of nanoparticles and macromolecules in the ring region by coupling CRE with fluorescence[171], matrix-assisted laser desorption (MALDI)[21], and Raman spectroscopy[172] enabling a relatively low limit of detection of polymeric nanocrystals[127], proteins[173], and polycyclic aromatic hydrocarbons[37]. In these applications the separation capability of the CRE was based on the size differences in particles or molecules. Generally, the larger the molecular size, the lesser the influence of the radial outward flow and thus, the molecule would travel a shorter distance. This approach was applied for the separation of IgG antibodies and E-Coli cells[126], silicon nanocrystals (SiNCs)[127], platinum nanoclusters (PtNCs)[21], polystyrene bids[127], silica microparticles[4], and nanorods polymer monoliths[174].

The separation capability of the CRE was further exploited for small molecules, albeit challenging and in a limited number of studies. It is of particular interest to couple the CRE with surface-enhanced Raman spectroscopy (SERS), as this provides an approach that does not require major sample preparation and allows simultaneous detection of analytes thanks to their separation by CRE and distinct vibrational fingerprints[23]. The nanofilm surface can be used not only for the separation of analytes but also for the Raman signal enhancement. In previous studies, we have applied CRE coupled with SERS on the silver nanofilm for the speciation of stable oxoarsenic species (As^{III}, As^{V}, DMA^{V}, MMA^{V})[152] and unstable thioarsenicals (DMMTA^{V}, DMDTA^{V}) onto the gold nanofilm (AuNF)[175]. Manipulating the chemical environment (e.g., pH and buffer solution) enabled us to control the traveled distances of the arsenicals across the drying droplet, aiding in their identification besides their distinct Raman shifts. Indeed, the selective deprotonation of target compounds induces the unique interactions of molecules with the AuNF surface resulting in their distinct traveled distances. Besides, the hydroxyl of DMA^{V}, thiol of DMDTA^{V,} and thionyl of DMMTA^{V} functional groups have a different affinity to the AuNF surface, leading to specific interactions with AuNF, controlling their adsorption on the surface and traveled distances during the formation of the CRE stain. Eventually, the molecular charge and the chemical composition of individual arsenicals enabled us to predict the deposition of each molecule at the specific region across the CRE deposit.

The expanded applications of CRE-driven separation from particles to macromolecules and small molecules prompt us to consider the theory behind this new nanochromatography. The theory behind the single drop evaporation onto the dry surface and colloidal particle accumulation in the ring regions is well established and theoretical approaches have been developed[155, 167]. Three major factors affect the formation of the CRE deposit: the radial outward flow, particle-surface interactions, and the reversed Marangoni flow, where the last one is relatively weak in the aqueous solutions and can be neglected[168]. The radial outward flow mainly depends upon the solvent evaporation flux, solution density, and the total evaporation time of the drying droplet, while the attraction/repulsion interactions govern the particles-substrate adsorption/desorption processes. These forces could be described by Derjaguin-Landau-Verwey-Overbeek theory (DLVO) that encompasses the interactions by the attractive van der Waals (LW) and repulsive electrostatic (EL) forces[17, 176, 177], and later the DLVO method was transposed into the extended DLVO theory (XDLVO) that introduced the new type of particle-particle interactions: the Lewis acid-base (AB) forces[178]. The XDLVO theory defines the stability of a colloidal solution as a function of Gibbs free energy interactions between particles summarizing repulsive EL, attractive LW, and donor-acceptor AB interactions as functions of particle separation and obtaining total free energy of interaction for a colloidal system. Typically, in aqueous media, the donor-acceptor interactions are 10-100 times greater than EL and LW interactions stabilizing the colloidal suspension by hydration effects[179]. With the recent expansion of CRE-driven separation to small molecules, it becomes increasingly intriguing to relate the theory of coffee ring formation and particle-surface interaction to the separation process and ideally to resemble the classic plate and rate theories of chromatographic separation.

Herein, we have developed a theoretical framework to describe the CRE-driven separation process of small molecules, using SERS analysis of dimethylarsinic acid (DMA^V), dimethylmonothioarsinic acid ($DMMTA^V$), and dimethyldithioarsinic acid ($DMDTA^V$) on AuNF as an example. We created the theoretical approach for the CRE-based separation by encompassing the theoretical background of the CRE, XDLVO, and traditional chromatographic theory[17]. We have applied the general chromatography theory for the development of the CRE providing that the radial outward flow in a drying droplet resembles the mobile phase of thin layer chromatography (TLC), gas chromatography (GC), and high pressure liquid chromatography (HPLC) systems. We further adapted the classic van Deemter equation for the quantification of radial flow and mass transfer parameters influencing separation efficiency by employing the XDLVO theory to consider arsenicals-AuNF surface interaction. We investigated both theoretically and experimentally the traveled distances of arsenicals across AuNF by changing the pH environment to find the optimal conditions for the separation. We then adjusted the radial outward flow for each compound obtained from the van Deemter curves for the individual arsenicals. By using this model, we predicted the traveled distances of arsenicals and evaluated the possibility of separation of unknown analytes by the coffee ring-SERS, demonstrating the successful adaptation of classic chromatographic theory to CRE-driven nanochromatography.

4.3 The CRE-SERS chromatographic theoretic framework

To develop the theoretical approach for the speciation of small molecules by SERS-CRE we have incorporated the CRE and XDLVO approach into the general chromatography theory. In the first part, we provided the mathematical description of the radial outward flow, following the introduction of the mass transfer equations for the arsenicals partition from the bulk to the nanofilm surface. In the second part, we modified the van Deemter equation by introducing the radial flow as the mobile phase and the adsorption constants as mass transfer parameters.

The solvent evaporation rate of a droplet placed onto the flat support is a quasi-steady process that is dominated by diffusion from the droplet surface to the atmosphere[12] and mainly depends upon the evaporation time[9]. The velocity of evaporation remains constant most of the time[13] even though it is nonuniform and maximized at the pinned contact line[1]. To describe the evaporation rate J, the following assumptions were made: the shape of the droplet is a semispherical cap[14], suspended particles are uniformly distributed, the contact line remains pinned during the evaporation[15], and temperature, electrostatic, and gravity effects—are negligible[1, 16]. The radial flow is linearly proportional to the evaporation flow and inversely related to the density of the solution[17]:

$$u_r \sim \frac{J}{\rho} \tag{4.1}$$

where J is the evaporation rate, ρ is the density of the solution, u_r is the radial outward flow.

XDLVO theory considered the nanoparticle-nanoparticle interaction forces, and we extrapolated this approach to the small molecule-nanoparticle interactions. The mass transfer of thioarsenicals from the bulk to the AuNF surface depends upon the adsorption constant (K_{ad}), which is determined by the Gibbs free energy of the interaction between the AuNF and arsenicals. XDLVO theory proposed that the stability of the colloidal suspension is summarized as a combination of the attractive interactions (van der Waals forces), the electrical double layer repulsive energy (EL)[180], and the polar surface interaction energy (AB). The total interaction energy between particles is[181] is given as

$$\Delta G(tot) = \Delta G(EL) + \Delta G(LW) + \Delta G(AB) \tag{4.2}$$

Even though the magnitude of $\Delta G(AB)$ is 10-100 times greater than that of EL and LW[179], the $\Delta G(EL)$ and $\Delta G(LW)$ terms govern the adsorption of analytes onto the AuNF in the absence of $\Delta G(AB)$, thus they could not be neglected. The total Gibbs free energy could be calculated as

$$\Delta G(tot) = -RT \ln e^{\frac{-\Delta G(tot)}{RT}} = -RT \ln K_{ad} \tag{4.3}$$

here K_{ad} is the adsorption constant of arsenicals onto the AuNF. Generally, the adsorption of thiols at micromolar concentrations onto the AuNF was reported to be diffusion limited in comparison to the adsorption to the nanoparticles colloidal solution because of the surface area saturation difference between the nanofilm and nanoparticles[182-185], thus the 2nd Fick's law can be applied for the adsorption of the arsenic ligand from the bulk to the nanofilm surface as

$$\frac{\partial C}{\partial t} = \frac{D_s}{R} \frac{\partial^2 C_s}{\partial x^2} \tag{4.4}$$

where D_s is the diffusion coefficient to the stationary phase and R is the retardation factor. The retardation factor is proportional to the adsorption constant K_{ad}[186, 187]. Assuming equal diffusion paths of analytes from the bulk to the AuNF surface, the distribution coefficient can be expressed as

$$D_s = \frac{\partial C}{\partial t} \frac{\partial x^2}{\partial^2 C_s} * R = \frac{\partial C}{\partial t} \frac{\partial x^2}{\partial^2 C_s} (1 + \rho\, K_{ad}/\theta) \tag{4.5}$$

where ρ is solution density, θ is surface porosity. Assuming the uniform porous distribution of the cavities (active sites) on the AuNF, density of water (1 g/cm^3), and plugging eq 4.5 into the van Deemter general chromatographic equation, we obtain

$$H = 2\varphi d_p + \frac{2\gamma D(m)}{u_R} + \left(\frac{wd^2}{D(m)} + \frac{R{d_f}^2}{\frac{\partial^2 C_s\, \partial t}{\partial C\, \partial x^2} * (1 + K_{ad})} \right) u_R \tag{4.6}$$

where H is the plate height, φ is the shape of the nanoparticles, d_p is the diameter of AuNPs, $D(m)$ is the diffusion coefficient of the mobile phase; γ, w, R are constants, d_f is AuNF thickness. Assuming that $D(m)$'s in liquid chromatography are relatively small in contrast to the gas chromatography, d_f is uniform, the equal speed of the arsenicals to be adsorbed on the AuNF surface, and the equal diffusion length of their adsorption path, one can simplify eq 4.6 into

$$H = A + \frac{B}{u_R} + (C_m + C_S)u_R \tag{4.7}$$

4.4 Experimental procedures

4.4.1 Materials and chemicals

Cacodylic acid sodium salt, 98% (DMA^{V}), NaOH, HCl, Citric acid, Sodium citrate dihydrate (Granular certified), (3-Aminopropyl)trimethoxysilane (APTMS), glass microscope slides, weighing boats, and 25 ml glass vials were purchased from Fisher scientific Inc (Hampton, NH). The citrate buffer (pH=3-7) was fabricated by mixing Citric acid and Sodium citrate. All solutions were prepared in deionized (DI) water (18.2 MΩ, Barnstead Nanopure Diamond).

4.4.2 Instrumentation

The Raman spectrometer was purchased from Jasko (NRS-4100), with a diode laser at 785 nm and average power of 33 mW. For optimizing resolving power, the 100 × optical lens focusing was used. A silicon wafer was employed to calibrate the Raman system at daily use and the Raman signal intensity at 520 cm^{-1} was monitored to check the reproducibility of the instrument. The SERS measurement parameters include the laser wavelength, 785 nm, exposure time, 4 seconds, and 1 time of exposure per measurement. The synthesis of thioarsenicals and determination of their respective Raman spectra were performed in the previous reports[130, 131].

The fabrication of AuNF was performed through the silanization of the glass substrates, followed by the deposition of nanoparticles onto the silanized surface[143]. Immediately after the droplet contained 100 mg L^{-1} of arsenic ligands deposition onto the gold nanofilm, the droplet was freeze-dried and the Raman spectra were collected. The adsorption of arsenic species onto the AuNF was carried out at pH = 3 and pH = 7, in the concentration range from 10^{-3} to 10^{-9} mol L^{-1}.

4.5 Adsorption of arsenicals

The adsorption of analytes onto the nanoparticles in colloidal solution significantly differs from the adsorption onto nanofilms. To ensure the uniform adsorption (without the CRE), the freeze-drying pretreatment was performed before SERS measurements once the 2µL arsenicals buffer solution was placed onto the AuNF. The average SERS signal of arsenicals was acquired from the center to the edge of the dried deposit (n=3). The SERS intensities for the quantitative analysis were normalized by the background correction.

4.5.1 Computation on Geometry optimization of arsenic ligands on a flexible Au(111) cluster.

We have performed the DFT calculations to assess the interactions energies of arsenicals with AuNF surface. This allowed us to estimate the affinity of arsenicals to AuNF, and thus, to predict the traveled distances of analytes during the formation of a coffee ring stain. Eventually, this theoretical model will be used for estimating the separation capability of the coffee ring-based approach: whether the developed method would separate target molecules or not.

Possible structures of the arsenical ligands complexed on an Au(111) gold cluster were modeled using Density Functional Theory (DFT). The B3LYP hybrid functional[188, 189] combined with the LANL2DZ-ECP basis set for Au[190], and the 6-31G* basis set for As, C, O, S and H atoms[191] was employed in the DFT calculations. The initial guess of wave functions was obtained using Hartree-Fock (HF) calculations followed by the stability check of a wave function. After the geometry optimization, the character of the optimized structures was checked by running frequency calculations to ensure absence of imaginary frequencies. The gas phase free energy of species, including zero-point energy (ZPE), was calculated at T = 298.15 K and p = 1 atm. All calculations including Raman frequencies of the ligand – gold complexes were carried out using the Q-Chem 4 electronic structure modeling package[192]. The pH effects on the arsenical-gold cluster interactions were modeled by simulating adsorption of neutral and negatively charged arsenic ligands. In the absence of the experimental structure, the starting geometry of the neutral (DMA^{V}, DMMTA^{V}) and deprotonated arsenicals (DMA^{V-}, DMMTA^{V-}, DMDTA^{V-}), and 28-gold atoms two layers cluster[193] were created manually by placing the optimized ligand above the gold surface in the vicinity of the gold surface binding sites. Experimentally, during the adsorption of a ligand onto a gold surface, the distortion and deformation of the gold surface occur; for this reason, in our calculations, the gold atoms in the cluster were not frozen and upon optimization formed adatom-like structures[194]. The solvation contribution to the free energy was estimated using the Self-Consistent Reaction Field method (SCRF)[195] in Truhlar's SMD implementation as a single point solvation free energy of the gas-phase optimized structures. The water-cluster thermodynamic cycle[196] was employed to improve SCRF calculations of the solvation free energy of ionic species. Specifically, the charged centers of arsenicals were solvated by three water molecules to saturate the lone pairs.

4.5.2 Theoretical computation on Gibbs free energy of Au-arsenicals complexes

To calculate the adsorption isotherms of the arsenicals onto the AuNF surface by the SERS method, the most intense SERS vibrational bands of individual species were chosen. For the calculation of the Gibbs free energy of adsorption, the Langmuir isotherm was employed[197], using the following equation[198]:

$$\vartheta = \frac{I}{I_0} = \frac{K_{ad}[A]}{1 + K_{ad}[A]} \tag{4.8}$$

where ϑ is relative coverage of AuNF surface by arsenical, I is SERS intensity at the concentration [A], I_0 is SERS intensity at the saturation of AuNF surface coverage, K_{ad} is adsorption constant, and [A] is the concentration of arsenical.

Adsorption of thiols onto the gold nanofilm is a diffusion-limited process in comparison to the adsorption to the nanoparticles in colloidal suspension because of the difference in the length between nanoparticles; in solution, the distance between nanoparticles is on the micrometer scale while the flat nanofilm exhibits the nanometer scale[182, 183]. The Gibbs free energies of complexation (DFT) of arsenical-Au clusters were calculated as shown below[193].

$$\Delta G_{tot}(\text{gold-arsenical}) = \Delta G_{tot}(\text{gold-arsenical}) - \Delta G_{tot}(\text{gold}) - \Delta G_{tot}(\text{arsenical}) \tag{4.9}$$

4.6 Results and Discussion

4.6.1 Computational mechanism of arsenicals adsorption onto the AuNF surface.

As the adsorption of arsenicals onto the AuNF surface controls the mass transfer from the bulk to the AuNF, we investigated the pH dependent arsenicals adsorption both theoretically and experimentally, allowing us to predict the pH influence on the traveled distances of arsenicals. We employed the QChem 4 software for the geometry optimization and energy calculations of arsenic-gold cluster complexes. Analyzing the gas phase optimized structures of arsenicals, we observed that negatively charged DMA^{V-}, $DMMTA^{V-}$ and $DMDTA^{V-}$ formed three bonds upon adsorbing onto the gold cluster in contrast to the neutral species that coordinated through a single interaction. To mimic the aqueous environment and to compensate for the solvation effects upon adsorption of negatively charged species onto the gold cluster, three molecules of water were added to each negatively charged arsenical. The energies of adsorption of neutrally charged arsenic ligand (DMA^{V}, $DMMTA^{V}$, $DMDTA^{V}$) were not affected by the solvation experiment with three water molecules, whereas the adsorption energies of negatively charged ligands (DMA^{V-}, $DMMTA^{V-}$ and $DMDTA^{V-}$) were considerably decreased after the solvent addition (**Table 3**). Thus, hydrogen bonding between the water and negatively charged ligands lowers the complexation energies.

The adsorption mechanism of thioarsenicals ($DMMTA^{V}$, $DMMTA^{V-}$ and $DMDTA^{V-}$) is similar to the adsorption of thiols and disulfides onto the AuNF. It starts with physisorption, with the H atom remaining within the hydroxyl group and is followed by chemisorption leading to the breakage of the OH bond and formation of Au-O or Au-S bonds[199]. The adsorption mechanism included the hybridization of p-like S orbitals with d-like Au orbitals producing both bonding and antibonding occupied orbitals. The process is well described by a model for the interaction of localized orbitals with narrow-band dispersive electron states at the bridge site between two surface Au atoms[200]. The Au-S bond is van der Waals dominated with lesser coordination and smaller directional input[201]. The neutral Au (0) $d^{10}s^0$ state dominates the nanofilm surface and the Au – Au bonding and reduces the covalent character of the Au – S bond. This is the cause of the directional change and the gold super exchange[202] leading to the S – Au adatom binding systems[203].

4.6.2 Chromatographic theory for the separation of small molecules by CRE-SERS

We have incorporated the theories of CRE and XDLVO into the general chromatography theory (van Deemter equation) to develop the theoretical approach for the separation of small molecules by CRE-SERS analysis. The velocity of radial outward flow (mobile phase) was calculated through the CRE theory, while the mass transfer for the arsenicals partition from the bulk to the nanofilm surface was characterized by the XDLVO theory. We extrapolated the XDLVO approach from its original nanoparticle-nanoparticle interaction forces to the small molecule-nanoparticle interactions. The mass transfer of arsenicals from the bulk to the AuNF surface depends upon the adsorption constant (K_{ad}), which is determined by the Gibbs free energy of the interaction between the AuNF and arsenicals, including the attractive interactions (van der Waals forces), the electrical double layer repulsive energy (EL)[180], and the polar surface interaction energy (AB). The 2nd Fick's law was then applied for the adsorption of the arsenic ligand from the bulk to the nanofilm surface, where the diffusion coefficient to the stationary phase (D_s) is related to K_{ad} through the retardation factor (R)[186, 187]. By introducing the radial flow as the mobile phase and the adsorption constants as mass transfer parameters and assuming the uniform porous distribution of the cavities (active sites) on the AuNF, we obtained the following modified van Deemter equation.

$$H = 2\varphi d_p + \frac{2\gamma D(m)}{u_R} + \left(\frac{wd^2}{D(m)} + \frac{j{d_f}^2}{\frac{\partial^2 C_s \, \partial t}{\partial C \, \partial x^2} * (1 + K_{ad})} \right) u_R \qquad (4.10)$$

where H is the plate height, φ is the shape of the nanoparticles, d_p is the diameter of AuNPs, $D(m)$ is the diffusion coefficient of the mobile phase; γ, w, j are constants, d_f is AuNF thickness. Assuming that $D(m)$ in liquid chromatography is relatively small in contrast to the gas chromatography, d_f is uniform, the equal speed of the arsenicals to be adsorbed on the AuNF surface, and the equal diffusion length of their adsorption path, we can simplify eq 4.10 into eq 4.11, realizing the adaption of classic chromatographic theory to the CRE-driven separation process.

$$H = A + \frac{B}{u_R} + (C_m + C_S)u_R \qquad (4.11)$$

4.6.3 Theoretical and experimental Gibbs free energy of Au-arsenicals complexation

The Langmuir isotherm was employed[197, 198] for the calculation of the Gibbs free energy of arsenicals adsorption onto the AuNF surface. The structures of Au-arsenicals complexes, their SERS spectra, corresponding adsorption isotherms, and the Gibbs free energies of complexation (DFT) of arsenical-Au clusters were calculated as shown below[193] and are summarized in **Table 3.**

The adsorption of arsenicals onto the AuNF surface is pH dependent. The negatively charged arsenic-Au complexes (DMA^{V-}-Au, DMMTA^{V-}-Au, DMDTA^{V-}-Au) demonstrate the lower Gibbs free energy and, consequently, the higher binding affinity to the AuNF in contrast to the neutral adsorbates (DMA^{V}-Au, DMMTA^{V}-Au).

$$\Delta G_{tot}(\text{gold-arsenical}) = \Delta G_{tot}(\text{gold-arsenical}) - \Delta G_{tot}(\text{gold}) - \Delta G_{tot}(\text{arsenical}) \qquad (4.12)$$

The calculated energies were lower than the literature data for the similar sulfur-containing compounds mainly because of the computational limitations; only three molecules of water were employed for the solvation simulation of the arsenicals-AuNF complexes. However, even with the limited solvation, the experimental data correlate with the theoretical values. Considering the experimental data, it is clear that the adsorption of the sulfur-containing arsenicals (DMMTA^{V}-Au, DMMTA^{V-}-Au, DMDTA^{V-}-Au) regardless of the molecular charge was a chemisorption process in agreement with the literature data for the thiols and sulfides chemisorption adsorption onto the AuNF surface (6-14 kcal), whereas oxygen-containing arsenicals (DMA^{V}-Au, DMA^{V-}-Au) demonstrated physisorption (with Gibbs free energies less than 6 kcal)[184, 204]. The binding capacity of negatively charged thiolates (DMDTA^{V-}) is generally higher than that of neutral thiones (DMMTA^{V})[199]. The general trend for the adsorption of arsenicals from the highest to the lowest adsorption values is the following: DMDTA^{V-}-Au > DMMTA^{V-}-Au > DMMTA^{V}-Au > DMA^{V-}-Au > DMA^{V}-Au (**Figure 16**).

Table 3. The adsorption energies of arsenicals onto the AuNF surface.

Arsenical	ΔG_{tot} (DFT) (in vacuo) (kcal/mol)	ΔG_{tot} (DFT) (water) (kcal/mol)	ΔG_{tot} (Experimental) (kcal/mol)	K_{ad} (Experimental) (mol^{-1})
DMA^{V}-Au	-7.1	-7.1	-4.8	3.7×10^{3}
DMA^{V-}-Au	-31.5	-24.5	-5.2	7.0×10^{3}
$DMMTA^{V}$-Au	-19	-19	-6.1	3.0×10^{4}
$DMMTA^{V-}$-Au	-45	-30.4	-8.7	2.5×10^{6}
$DMDTA^{V-}$-Au	-40.5	-44.2	-11.4	1.5×10^{8}

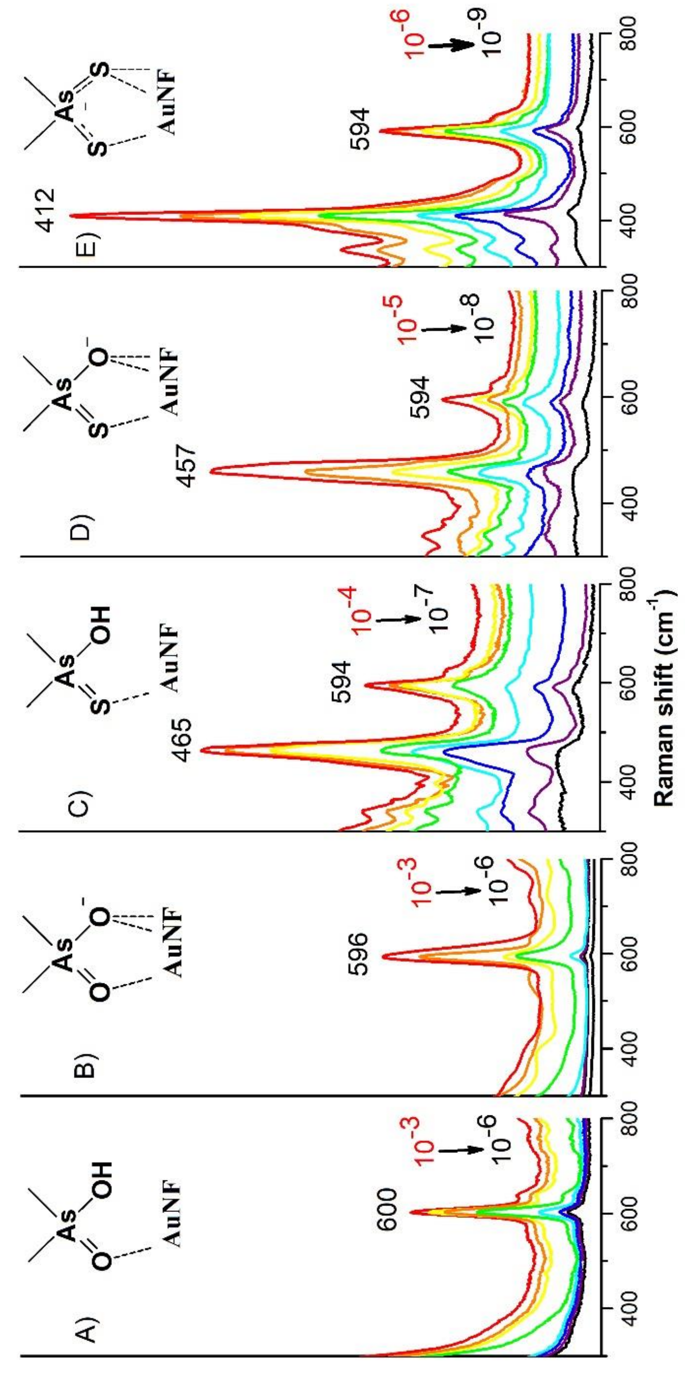
Raman intensity (a.u.)
Raman shift (cm^{-1})
A)
600
10^{-3}
10^{-6}
B)
596
10^{-3}
10^{-6}
C)
465
594
10^{-4}
10^{-7}
D)
457
594
10^{-5}
10^{-8}
E)
412
594
10^{-6}
10^{-9}
As
O
OH
S
AuNF
400
600
800

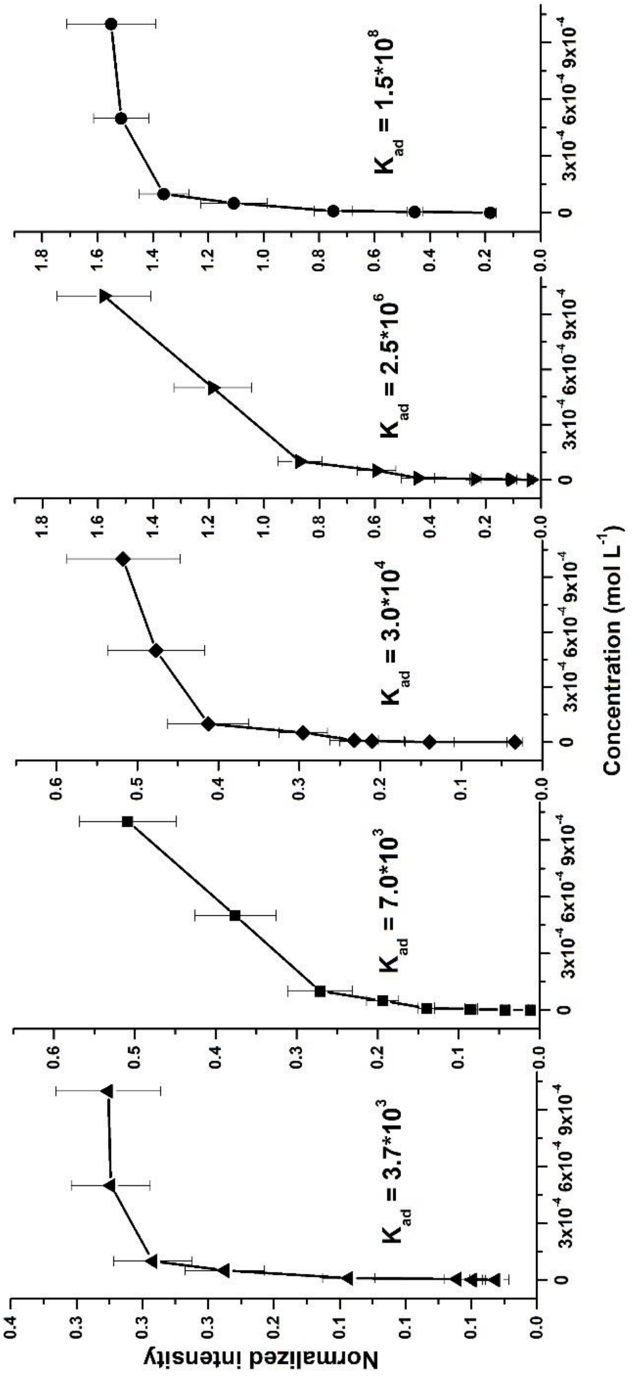

Figure 16. The adsorption isotherms of arsenicals upon complexing with the AuNF and the corresponding SERS spectra of A) DMA^{V}, 600 cm^{-1} and B) DMA^{V-}, 596 cm^{-1} (the As – C symmetric stretching); C) DMMTA^{V}, 465 cm^{-1} and D) DMMTA^{V-}, 457 cm^{-1} (the As=S stretching); E) DMDTA^{V}, 412 cm^{-1} (the As÷S delocalized stretching).

4.6.4 Travel distances of arsenicals under different pHs

The travel distances of arsenicals were estimated in the pH range from 3 to 7 as shown in **Table 4** (τ_{evap}=35 min), where a relative retention, t_R (compound))/ t_R (solvent), was defined and used for describing the travel distances of each analyte. To trace DMA^V we have recorded the SERS signals for the As – C stretching at 600 cm^{-1} for neutral, and 598 cm^{-1} for the deprotonated forms across the CRE stain. In the pH range from 3 to 5, the neutral form of DMA^V (pKa=6.20) traveled a long distance from the center to the edge regions of the drying droplet, however, as the pH increases, the length of the movement decreased, which can be attributed to the stronger interactions between DMA^{V-} and citrate anions through the hydrogen bonding resembling As^{III}-AuNF complexation[205]. Similarly, $DMMTA^V$ (the As=S stretching, 469 cm^{-1} for neutral – 457 cm^{-1} for the deprotonated forms) having pKa of 3.5 covered a longer distance in contrast to the deprotonated compound. Once the pH increases, the $DMMTA^V$ becomes more ionic decreasing its Gibbs free energy of adsorption (**Table 3**) and substituting the citrate onto the AuNF surface. Considering $DMDTA^V$'s (the As÷S stretching, 412 cm^{-1}, pKa = 2.25) traveled distance it was not considerably affected by the pH changes. Regarding the higher adsorption energy of $DMDTA^V$ onto the AuNF surface than those of DMA^V and $DMMTA^V$, this arsenical was immediately adsorbed onto the AuNF surface, representing the constant SERS signal across all regions. Overall, it is implied that the higher attraction of the arsenicals to the surface, the shorter migration distance, and the larger the Raman shift.

Table 4. The dependence of arsenicals traveled distances on the AuNF upon pH.

Relative retention, $\frac{t_{R\,(compound)}}{t_{R\,(solvent)}}$				$t_{R\,(solvent)}$, mm
pH	DMA^V(As-C)	$DMMTA^V$(As=S)	$DMDTA^V$(As÷S)	H_2O/buffer
3	0.81±0.09	0.40±0.03	0.46±0.04	6.20±0.74
4	0.81±0.07	0.39±0.03	0.47±0.03	
5	0.65±0.08	0.37±0.03	0.47±0.05	
6	0.57±0.08	0.36±0.02	0.47±0.03	
7	0.50±0.08	0.35±0.02	0.48±0.02	

4.6.5 Optimizing parameters for the derived van Deemter equation: pH and radial flow velocity

We started the separation optimization by selectively tuning the pH of the mobile phase to maximize the difference in traveled distances of each arsenical. Thus, the retention factor (k) normalized by the mobile phase front and the selectivity factor (α) were plotted against the pH to obtain the pH windows for each pair of arsenicals as shown in **Figure 17A** and **Figure 17B** respectively. The highest selectivity for $DMA^V/DMMTA^V$ and $DMA^V/DMDTA^V$ was achieved at pH=4.0.

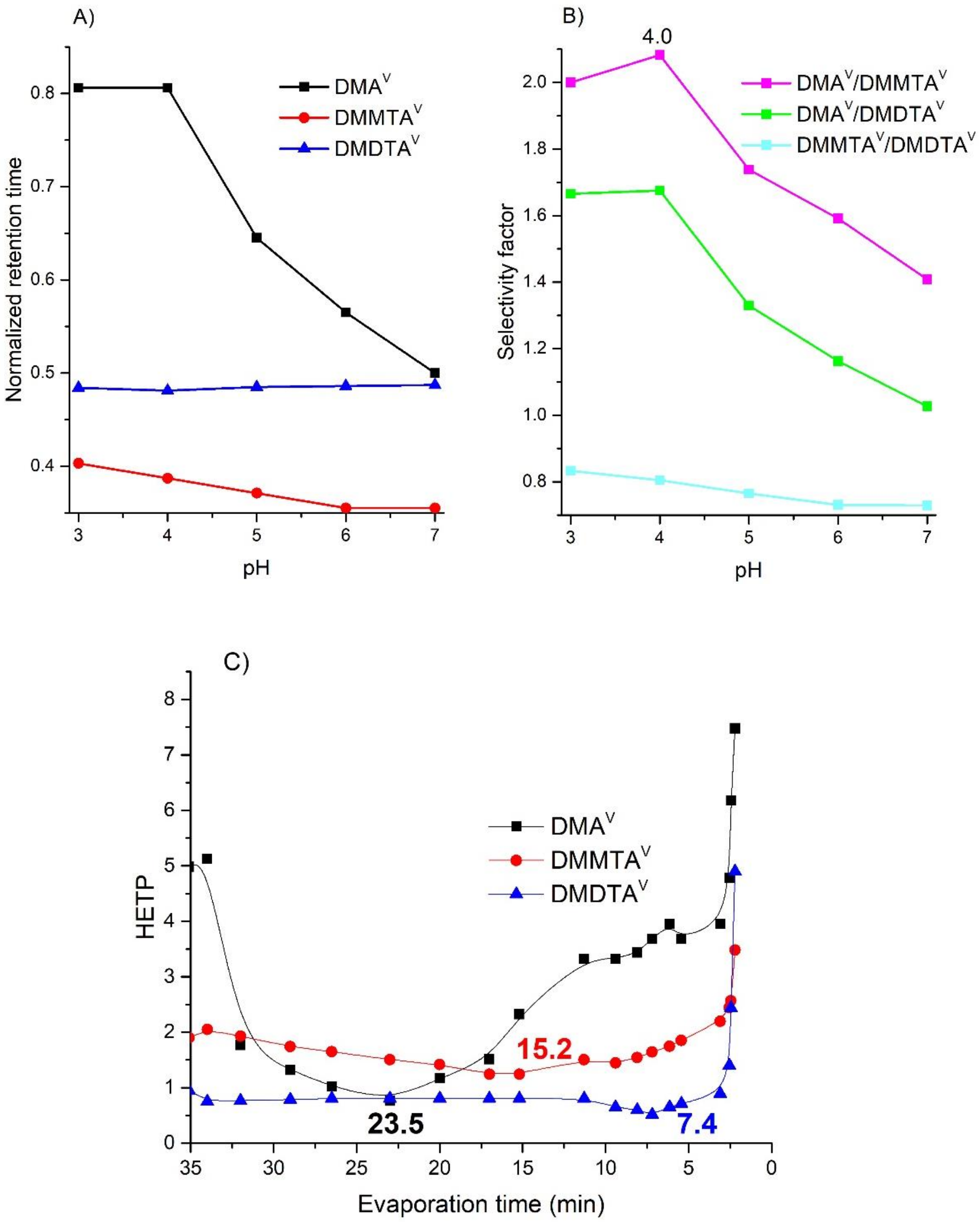

Figure 17. A) The retention factor (k) and B) the selectivity factor (α) for CRE-driven separation of arsenicals under different pHs; C) HETP curves of individual arsenicals obtained from the modified van Deemter equation to calculate the optimal mobile phase velocity rate for DMA^V, DMMTA^V , and DMDTA^V.

The graph of the HETP vs the radial flow velocity was constructed in **Figure 17C**. Analyzing the van Deemter curves of the individual arsenicals it is seen that the increase of the mobile phase rate at the higher evaporation times significantly affects the HETP of DMA^{V}, in contrast to that of thioarsenicals DMMTA^{V} and DMDTA^{V}. This could be because of the difference in the retention factors of DMA^{V} and thioarsenicals. At lower speeds of the mobile phase, DMA^{V} is much more influenced by the radial movement resulting in the minimum of the HETP at 23.5 min. Interestingly, that radial flow considerably affects HETP's of thioarsenicals, only at the fastest rates providing the minimum of HETP at 15.2 and 7.4 for DMMTA^{V} and DMDTA^{V}, respectively. The optimal velocity of the radial flow was computed to be 15.4 min.

The resolution calculation of each pair of compounds was summarized in **Figure 18**. For DMA^{V}/DMMTA^{V} and DMA^{V}/DMDTA^{V} the peak resolution was found to be 1.5 which is the minimum method resolution that allowed the proper peak identification. However, for DMMTA^{V}/DMDTA^{V} the resolution accounted only for 0.6 at optimized separation conditions. Even though the peak resolution was not enough to identify components based on their retention time, SERS provides a unique advantage by providing the unique fingerprint and allowing the identification of thioarsenicals based on their arsenic sulfur vibrations: DMDTA^{V} (As÷S stretching at 412 cm^{-1}) and DMMTA^{V} (As=S stretching at 465 cm^{-1}) in **Figure 19**.

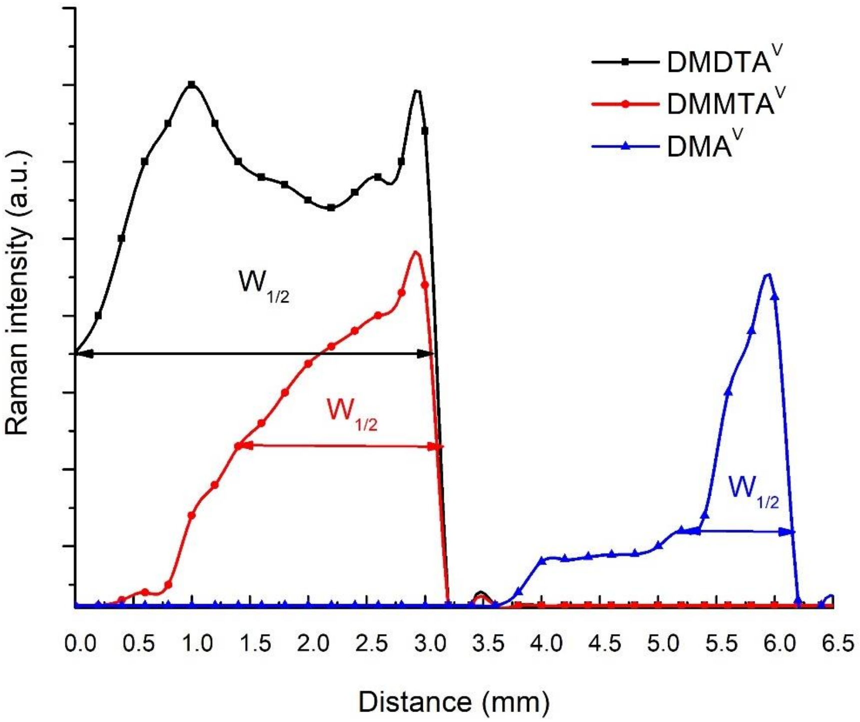

$$R_{\frac{DMA^V}{DMDTA^V}} = \frac{t_{R_{DMA^V}} - t_{R_{DMDTA^V}}}{W_{DMA^V} - W_{DMDTA^V}} = 1.5$$

$$R_{\frac{DMA^V}{DMMTA^V}} = \frac{t_{R_{DMA^V}} - t_{R_{DMMTA^V}}}{W_{DMA^V} - W_{DMMTA^V}} = 1.5$$

$$R_{\frac{DMMTA^V}{DMDTA^V}} = \frac{t_{R_{DMMTA^V}} - t_{R_{DMDTA^V}}}{W_{DMMTA^V} - W_{DMDTA^V}} = 0.6$$

Figure 18. The resolution calculations. A 2D diagram was drawn to calculate the retention time of the arsenicals and the resolutions.

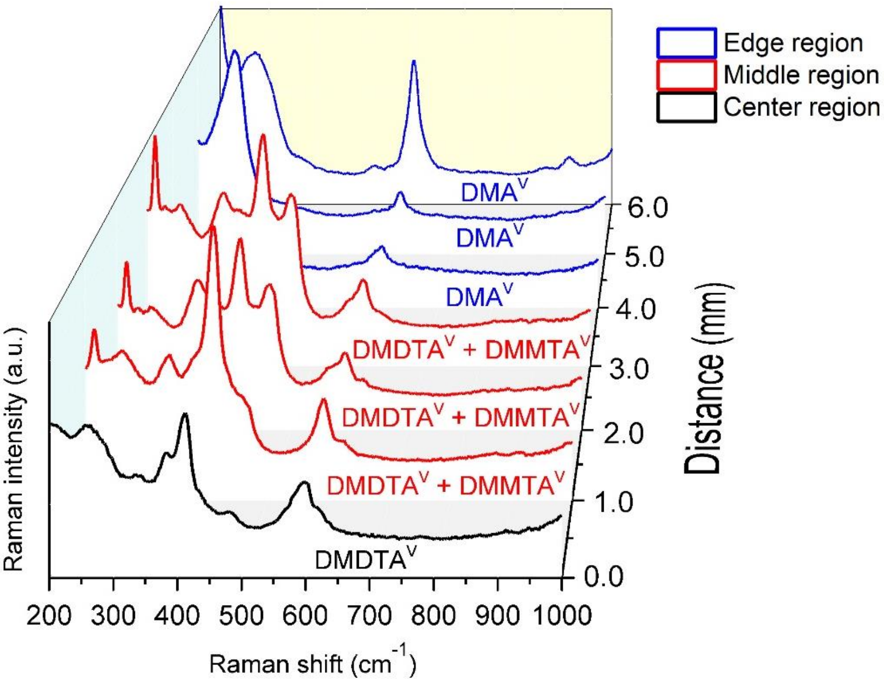

Figure 19. The CRE of DMA^V, DMMTA^V, DMDTA^V onto the AuNF at the optimized separation conditions (pH=4.0, u_R = 15.4 min).

4.6.6 General application of the developed theoretical framework to CRE-SERS of small molecules.

The developed theory can be used to predict the traveled distances of analytes by the pH and radial flow, expanding its applications for the CRE-driven separation of small molecules in general. As pH plays a crucial role in mass transport of compounds to the nanofilm surface, the pKa's of analytes (if unknown) needs to be calculated, e.g., by Marvin Sketch software that was deemed reliable here, followed by the optimization of pH to adjust the retention time and selectivity factor. Normally, as pH increases exceeding the pKa of an analyte, the adsorption constant of the species increases and the Gibbs free energy becomes more negative, resulting in the increased retardation factor that magnifies the diffusion coefficient and sorption of analytes (diffusion flux) onto the surface, thus the increased mass transfer from the bulk to the surface. The charged molecules usually travel shorter distances than the neutral ones do. The radial flow can also be adjusted to guide the molecule into the specific region of the coffee ring. This could be tuned by manipulating the atmospheric pressure evaporation of the sessile droplet. The lower the atmospheric pressure, the higher the evaporation rate, and thus the higher the radial outward flow, increasing the traveled distances.

To selectively apply this theory to small molecules, the following questions need to be considered: 1) What are the differences in molecular structures of target analytes that may trigger different interactions of these analytes with the negatively charged gold nanoparticles? and 2) What types of interactions do the target molecules have with the gold nanofilm (electrostatic, van der Waals, or donor-acceptor)? The final locations of analytes after the solvent evaporation could be expected in 1) the center region, where a molecule of interest is not significantly affected by the radial outward flow because it is hydrophobic or has a very high affinity to the AuNF surface through electrostatic attraction (positively charged molecules) or donor-acceptor interactions (like DMDTA^{V-} and DMMTA^{V-} here); 2) the middle region, where a compound is affected by the radial flow as it could be a neutral molecule that has relatively high AuNF surface attraction (like DMMTA^{V} and DMA^{V-}); or 3) the edge region, where an analyte is considerably affected by the radial flow as it might have the predominant neutral charge and a hydrophilic character (like DMA^{V}).

For the analytes that might not be completely separated by the CRE, SERS provides an additional advantage to identify the species through fingerprint Raman shifts.

4.7 Conclusion

A theoretical approach based on the combination of the CRE-driven separation and SERS detection on AuNFs has been developed for the speciation of small molecules. Considering the major factors affecting the formation of the CRE deposit, i.e. radial outward flow, analyte-AuNFs interactions, and Marangoni flow, the traditional chromatographic theory was adapted to derive a modified van Deemter equation for the CRE-driven separation, by combining the CRE theory for the radial flow and the XDLVO theory for the analyte-surface interactions. Through manipulating pH and the radial flow to find optimal conditions for the separation of DMA^V, DMMTA^V, and DMDTA^V, we demonstrated that the theoretical model could predict the travel distances of small molecules during the formation of the CRE deposit based on the different affinity of analytes with the AuNFs. This theoretical framework adopts a unified approach for both the conventional chromatographic techniques (e.g., GC and HPLC) and the CRE-based nanochromatography which employs a stationary phase on the nanometer scale to enable the separation at a very short distance (~5 mm). CRE-SERS analysis requires minimal sample pretreatment and allows for nondestructive and simultaneous detection of multiple species, thus presenting an alternative approach for potential in situ detection of fragile compounds.

Chapter 5. Application of gold nanofilm –based coffee ring effect and surface-enhanced Raman spectroscopy for speciation of Darinaparsin and its metabolite

Part of this chapter has been submitted to the Journal of Chromatography A for publication, as the following manuscript: Liamtsau, V., Liu, G., Cai, Y., Application of gold nanofilm–based coffee ring effect and surface-enhanced Raman spectroscopy for speciation of Darinaparsin and its metabolite.

5.1 Abstract

Darinaparsin ($DMA^{III}GSH$, DAR) is a novel arsenic-based anticancer drug consisting of dimethylated arsenic conjugated to glutathione (GSH) that found to be effective against acute promyelocytic leukemia (APL) and exhibits less toxicity comparing to commonly used arsenic trioxide (ATO). After exposure of DAR to the NB4 cancer cell line, its major breakdown product, dimethylarsino-cysteine ($DMA^{III}Cys$, DMAC), enters the cells and causes the therapeutic effect. The speciation of these S-conjugated arsenicals is challenging due to the sample alteration occurring during the extensive sample preparation and the speciation methods (LC/MS) that fail to provide the structural molecular information of DAR and DMAC. To address these issues, we have applied the nanochromatography method for the speciation of DAR and DMAC, which combines the coffee ring effect (CRE) and surface-enhanced Raman spectroscopy (SERS). SERS coupled with CRE requires minimal sample pretreatment and allows a nondestructive and simultaneous detection of multiple species due to their distinct vibrational fingerprints, thus presenting an alternative approach for the detection of fragile compounds. Once a sessile droplet is placed onto the gold nanofilm surface (AuNF) and the solvent evaporation started, the formation of a CRE stain begins. Two major factors that affect the formation of the CRE deposit were the radial outward flow and analyte-AuNF interactions. In the final CRE deposit, DAR was detected in the center and the middle regions, whereas DMAC traveled longer distances across the CRE stain and was in the middle and the edge regions. Despite the overlap of DAR and DMAC's Raman spectra, we were able to identify each compound due to their unique SERS fingerprint. Overall, the developed method was able not only to

separate and identify the S-conjugated arsenicals, but at the same time preserve the DAR and DMAC's As^{III} oxidations state and the fragile As – S moiety, thus providing an alternative speciation method for unstable thioarsenicals.

Keywords: Coffee ring effect, Gold nanofilm, Darinaparsin, SERS, Thioarsenicals

5.2 Introduction

Darinaparsin (S-dimethylarsino-glutathione, $DMA^{III}GSH$, DAR) is a novel arsenic-based anticancer drug consisting of dimethylated arsenic conjugated to glutathione[206]. This compound is more effective against acute promyelocytic leukemia (APL) than its toxic analog, arsenic trioxide (ATO)[207], and currently in phase 2 clinical trial. The Dar's molecule was initially designed by linking dimethylarsenic to glutathione (GSH) conjugate and demonstrated significant activity against cancers in mice providing that the Dar is less toxic, with a tolerated dose of is 50-fold higher than ATO[208]. DAR's possible mechanisms of action include interruption of the mitochondrial life cycle, an increase in reactive oxygen species (ROS), and disruptions of signal transduction resulting in cell apoptosis[209, 210]. The cellular uptake is a critical step for DAR's therapeutic efficacy. It was initially speculated that the major metabolic pathway for the As-GSH complexes is the hydrolysis of the fragile As – S bond leading to the formation of dimethylarsinous acid (DMA^{III}) resulting in further oxidation to dimethylarsenate (DMA^{V})[211]. A recent study, however, suggests that DAR is hydrolyzed by glutamyl transferase (g-GT) to cysteine S-conjugates, then further cleaved by cysteinylglycine dipeptidase (DP) to its major breakdown product, dimethylarsino-cysteine ($DMA^{III}Cys$, DMAC), which enters the cells through cystine/cysteine cellular import system (**Figure 20**)[212]. Interestingly, other potential DAR's metabolites, DMA^{III} or DMA^{V}, were not observed inside the NB4 cell line after DAR's uptake as they might not be generated or detected. The exposure of the NB4 cell lines to the extracellular GSH and thiols resulted in the decreased DAR uptake, suggesting that thiols might compete for cystine transporters, which appeared to be critical in DAR's transport leading to the decrease of DAR-induced intracellular arsenic uptake and the prevention of DMAC-induced intracellular accumulation of arsenic[213].

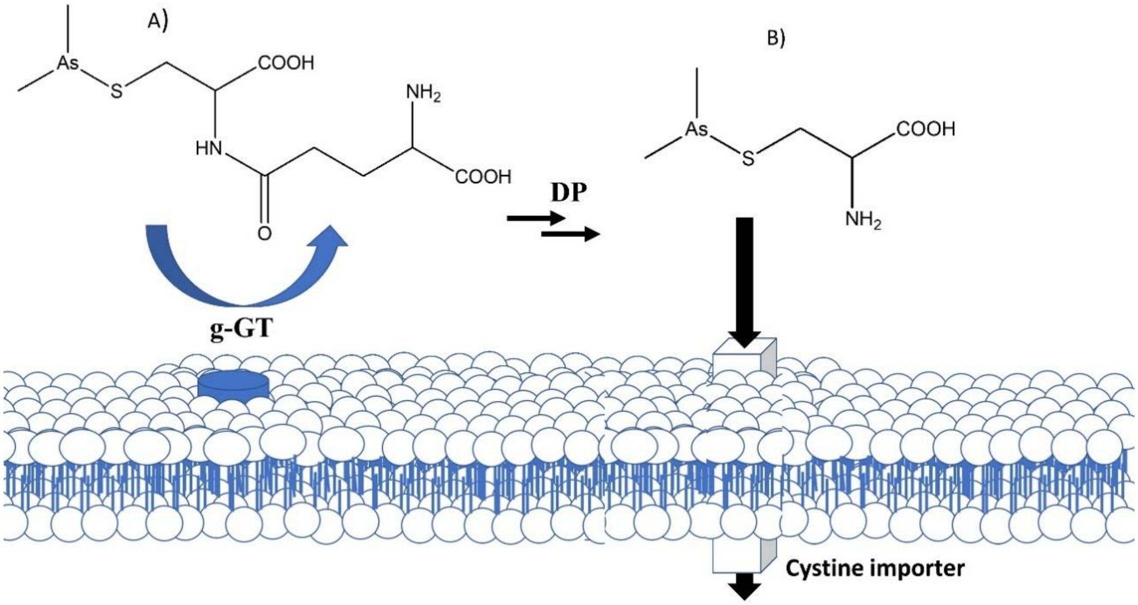

Figure 20. A) DAR and B) DMAC, and the proposed uptake pathway.

S-conjugated trivalent arsenicals sparked the interest in the chemistry of metabolomics thanks to their ability to bind to proteins via complexing with Cys residues resulting in the APL cell disfunctions[214]. Recently, DAR's exposure to the NB4 cell line leads to the disruption of histone H3.3 protein function resulting in nucleosomes destabilization. Interestingly, ATO was not detected in the cell's nuclei neither bonded to histone H3.3[215]. Thus, considering the high GSH cell levels (up to 10 mmol), As^{III}-GSH complexes are of key interest as they are omnipresent in the cell media and likely to bind to nuclei proteins and cause the therapeutic effect. It is therefore critical to determine the speciation of the S-arsenic conjugates, DAR and DMAC, to further investigate their complexation with biologically active molecules, which may offer new insights into the transformation and toxicity of arsenicals.

The speciation of arsenic compounds is commonly performed by high-performance liquid chromatography (HPLC) coupled with inductively coupled plasma mass spectrometry (ICP-MS) or electrospray mass spectrometry (ESI-MS), as exemplified by the detection of thirteen common arsenic metabolites (including S-conjugated arsenicals) present in humans[116]. These methods, however, require extensive sample preparation including acid-based extraction that might result in the sample alteration due to the hydrolysis and/or oxidation of unstable trivalent and thiolated arsenicals to pentavalent and oxoarsenicals[216]. The active binding site of DAR and DMAC is the As-S moiety that could be quickly decomposed during the extraction from the biological samples[57]. Furthermore, during the separation of As-GSH complexes by ion chromatography (IC), analytes transformation could occur resulting in species misidentification[211]. ESI-MS may have limited ability to detect S-conjugated arsenicals, as some As species do not have high ionization efficiency and/or could get oxidized during the electrospray ionization, or provide the exact structural information of the compounds, as exemplified by failing to differentiate As^{III} and As^{V} sulfur bonded species[217]. Investigating the complexation of

DAR to histone H3.3, arsenic-bonded protein, gel electrophoresis inductively coupled plasma mass spectroscopy (GE-ICP-MS) failed to provide specific structural information of the arsenic-protein complex neither determined the valence state of bonded to proteins arsenicals[215]. Since As-GSH complexes might be essential intermediates for As methylation[56], their explicit structural identification is critical to elucidate the potential pathways of As metabolism.

Considering the aforementioned drawbacks of the commonly used methods in As speciation, alternative methods that do not require rigorous sample treatment and offer detailed structural information are needed for accurate analysis of As-GSH complexes. A nanochromatography approach previously developed in our laboratory, employing surface-enhanced Raman spectroscopy (SERS) coupled with the CRE, could be optimal for the analysis of S-conjugated arsenicals, including DAR and DMAC, due to minimal sample pretreatment, mild CRE based separation and unique fingerprint Raman identification. CRE-SERS methods were previously employed for the separation of oxoarsenicals on silver nanofilm (AgNF)[175] and thioarsenicals onto gold nanofilm (AuNF)[218] enabling to preserve and detect a labile As-S moiety. CRE allows separating compounds by exploiting their different migration distances due to distinct interactions of analytes with the nanofilm during the formation of the CRE stain[21]. To the best of our knowledge, no method has been developed for the speciation of DAR and DMAC, yet it is necessary to identify individual DAR and DMAC and obtain their explicit structural molecular information to further investigate the mechanism of DAR anticancer activity and understand the protein binding efficiency of arsenic S-conjugates[123].

In this work, we aimed to extrapolate the CRE-SERS nanochromatography approach developed for the speciation of small arsenic-based molecules to more complex, peptide conjugated arsenicals, specifically DAR and DMAC. We have applied this method for the speciation of DAR and DMAC by selectively adjusting two major factors affecting the formation of CRE deposit: the pH influencing the interactions of analytes with AuNF and the radial outward flow governing speciation of DAR and DMAC. Due to the different DAR/DMAC-AuNF interactions, the separation was achieved enabling identification of each metabolite. The key advantage of the CRE-SERS is the preservation of the labile DAR and DMAC' As-S-Au moiety and As^{III} oxidation state, which is critical for the identification of S-conjugated arsenicals.

5.3 Experimental

5.3.1 Materials and chemicals

Cacodylic acid sodium salt, 98% (DMA^{V}), NaOH, HCl, Sulfuric acid, Citric acid, Sodium citrate dihydrate (Granular certified), (3-Aminopropyl)trimethoxysilane (APTMS), glass microscope slides, weighing boats, and 25 ml glass vials were purchased from Fisher scientific Inc (Hampton, NH). The citrate buffer (pH = 3-7) was prepared by mixing citric acid and sodium citrate. All solutions were prepared in deionized (DI) water (18.2 MΩ, Barnstead Nanopure Diamond).

5.3.2 Instrumentation

The Raman spectrometer was obtained from Jasco (NRS-4100), which has a diode laser at 785 nm with a maximum power of 33 mW. For optimizing resolving power, the 20 × optical lens focusing was acquired. A silicon wafer was employed to calibrate the Raman system at daily use and the Raman signal intensity at 522 cm^{-1} was monitored to check the reproducibility of the instrument. The SERS measurement parameters were laser wavelength, 785 nm; exposure time, 1 s; and 4 times of exposure per measurement. The AuNF surface was characterized by the Veeco multimode atomic force microscope (AFM). Malvern Zetasizer Nano-ZS (Westborough, MA) was employed for the measurements of nanoparticles size (average diameter) and zeta potential. All pH measurements were carried out on a Fisher Scientific Research AR15 pH/mV/°C Meter. The AuNF was fabricated based on the previous procedure[218].

5.3.3 Synthesis of S-conjugated arsenicals and determination of their respective Raman spectra

DMAC complex was prepared by reduction using a mixture of DMA^{V} (0.66 mmol) with L-cysteine (0.33 mmol) in 10 ml of degassed DI water under nitrogen[129]. The reaction was carried out at room temperature using magnetic stirring for three hours[19]. After the reaction, the solution was centrifuged, and the supernatant was collected. After the supernatant evaporation, the white residue powder was carefully collected for further analysis.

DAR was synthesized according to previously published procedures with minor modifications[219]. Briefly, DMA^V (2 mmol) and GSH (6 mmol) were dissolved in 10 mL deionized water, and the solution was stirred overnight under a nitrogen atmosphere. Then, the water was evaporated under reduced pressure without heating using a centrifugal concentrator. DAR was then extracted from the residue using ice-cold methanol. A white powder was obtained after methanol evaporation, following the further drying and storage into a desiccator.

5.3.4 Separation and identification of Dar and DMAC on the AuNF surface

The Dar and DMAC 100 ppm solutions were freshly prepared in the citrate buffer (pH=3-7). Then, a 2µl drop of the individual DAR and DMAC citrate buffer solutions was deposited onto the AuNF surface. After the droplet evaporation, the SERS signals of the individual compounds were obtained across the CRE stain regions (center – middle – edge regions). Similarly, with the speciation of individuals analytes, a 2µl drop of 100 ppm citrate buffer DAR and DMAC mixture was placed on the AuNF surface and once solvent evaporated, the SERS measurements were obtained from the center to the edge region of the CRE.

5.4 Results

5.4.1 Comparison of DAR and DMAC Raman spectra

Raman spectra of individual DAR and DMAC (solid/liquid) were acquired in the range from 200 cm^{-1} to 1000 cm^{-1} providing the vibrational fingerprint of each molecule (**Figure 21**). Both DAR and DMAC exhibits three major Raman peaks: symmetrical As – S, As – C, and C – S vibrational stretchings corresponding to 370 cm^{-1}, 610 cm$^{-1,}$ and 650 cm^{-1} respectively. The Raman As – S and As – C vibrational modes were similar to recently reported thioarsenicals[218]. The vibration at 220 cm^{-1} is likely to be attributed to sulfur crown vibrational stretching of S_8 as of a synthesis biproduct[220], the peak at 825 cm^{-1} might be originated from the As-OH symmetrical stretching due to the traces of nonreacted DMA^{V}[175]. The other less intensive Raman signals at 780 cm^{-1}, 450 cm^{-1} , and 510 cm^{-1} are attributed to the impurities.

The major difference between Dar and DMAC's Raman spectra is the ratio between the As – S (370 cm^{-1}) and As – C (610 cm^{-1}) Raman vibrational intensities. Indeed, DAR demonstrated a higher As-C / As-S ratio of about 7, whereas DMAC's As-C / As-S was found to be 1.1. The identification of individual DMAC and DAR by Raman spectroscopy is hardly possible due to the overlap of their vibrational fingerprint (**Figure 24**), so it is necessary to apply the separation step before detection.

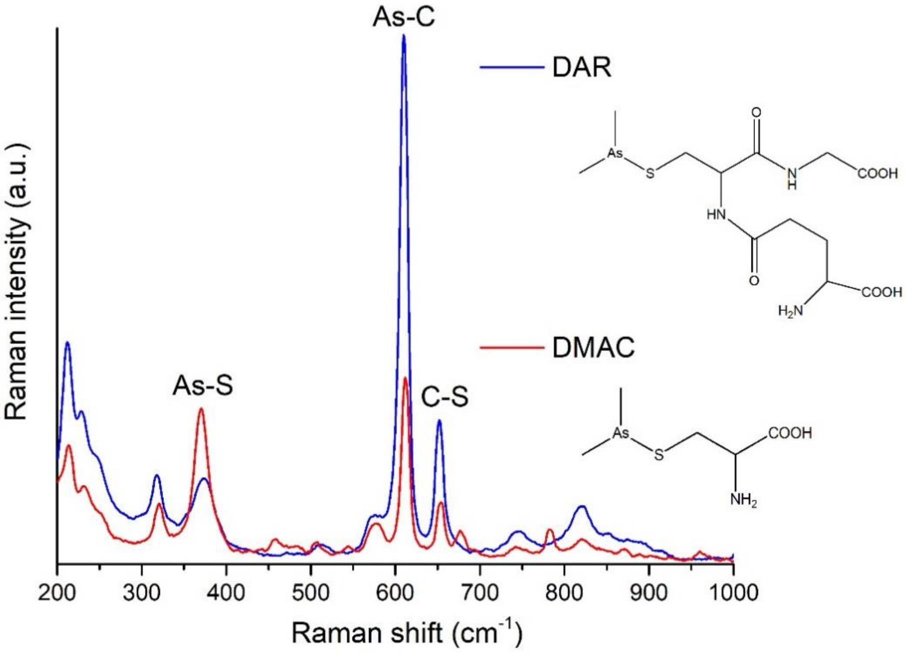

Figure 21. Raman spectra of DAR and DMAC.

5.4.2 Identification of individual DAR and DMAC using CRE-SERS

To track the formation of the CRE for DAR and DMAC separately, we have chosen the most intense SERS signal corresponding to the As – C symmetrical vibrational stretching at 594 cm^{-1} and 598 cm^{-1} for DAR and DMAC, respectively. DAR's SERS signal increased from the center to the middle regions following a slight decrease at the edge region suggesting the nontypical CRE stain formation (**Figure 25A**), while DMAC (**Figure 25B**) was mostly detected at the edge region and was absent in the center and the middle regions, demonstrating a typical CRE.

The differences between the Raman/SERS spectra of solid/liquid DAR and DMAC (adsorbed onto AuNF) were observed after SERS measurements at optimized separation conditions: pH=4, ν_{rad}=20 min. Comparing the Raman and SERS spectra of DAR, the Raman shift occurred for both fingerprint vibrational stretchings: As – C (610 cm^{-1} → 594 cm^{-1}) and As – S (375 cm^{-1} → 370 cm^{-1}), which indicates the charge transfer effect between the DAR molecule and the AuNF surface(**Figure 22A**)[148]. Similarly to DAR, DMAC's redshift was observed for the As – C (611 cm^{-1} → 594 cm^{-1}) and the As – S (375 cm^{-1} → 370 cm^{-1}) symmetrical stretchings (**Figure 22B**).

The broad signal at 245 cm^{-1} is attributed to the background signal of AuNF (the Au-OOC vibrational stretching) that is citrate bonded to AuNP onto the AuNF surface[149]. The SERS signal of the Au-S bond was pronounced at the ring region (265 cm^{-1}) which is associated mainly with the interaction of As-S-Au moiety with Au atoms of AuNPs by substituting citrate ligand onto the AuNF surface[161].

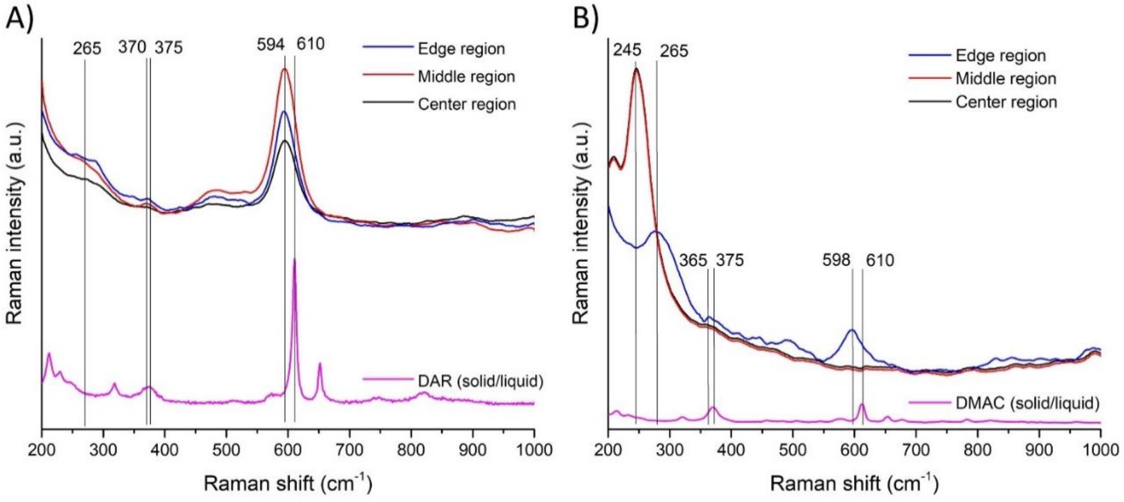

Figure 22. The CRE-SERS of individual A) DAR and B) DMAC onto AuNF. pH=4, ν_{rad}=20 min.

5.4.3 Application of CRE-SERS on AuNF surface for separation and identification of DAR and DMAC

The CRE for the DAR and DMAC mixture was similar to that of the individual compounds. Indeed, the SERS intensities of the As – S (365 cm^{-1}, 370 cm^{-1}) and As – C (594 cm^{-1}, 598 cm^{-1}) symmetrical vibrational stretchings increase from the center to the edge region of the CRE stain (**Figure 23**). Considering the Raman shift of the As – S vibrations, it is clear that DAR demonstrated a larger red shift accounting for 10 cm^{-1} (375 cm^{-1} → 365 cm^{-1}), which was detected in the middle region, in contrast to 5 cm^{-1} (375 cm^{-1} → 370 cm^{-1}) of DMAC's, presented mostly in the edge region. The additional evidence for DAR and DMAC final locations is the SERS peak at 265 cm^{-1} (the Au – S vibrational stretching), which increases from the center to the edge regions and might be originated due to the adsorption of the DAR and DMAC onto the AuNF surface trough the complexation of As – S moiety with Au surface atoms. As a result, only DAR was found at the center region, following the mixture of analytes in the middle and mostly DMAC in the edge region.

Raman shift variations of the major DAR and DMAC vibrations (the As – S and the As – C symmetrical vibrational stretchings) appeared mainly due to the adsorption of their molecules onto the AuNF surface providing high affinity of individual S-conjugates to Au[221] atoms leading to the formation of the Au – S – As cluster, which might orient the As – C bonds in out of plane direction (vertically) resulting in the relatively large Raman shift of the As – C stretching (610 cm^{-1} → 594 cm^{-1}) for DAR and (610 cm^{-1} → 598 cm^{-1}) for DMAC[222]. Interestingly, the Raman shift for DMAC' As – S stretching was larger than that of DAR: 10 cm^{-1} vs 5 cm^{-1} suggesting that DMAC might interact stronger with AuNF than DAR.

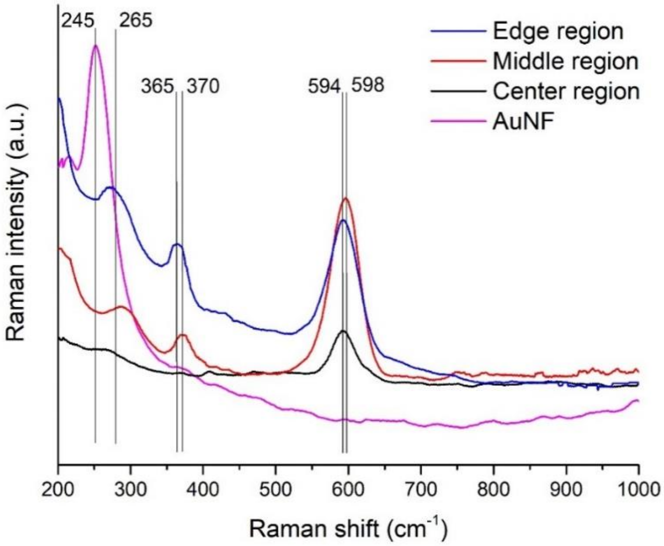

Figure 23. The SERS-CRE of the 100 ppm mixture Dar and DMAC onto AuNF (pH=4).

5.5 Discussion

Previously, we have created the theoretical model for speciation of the small molecules by the CRE-SERS method that enabled us to predict analytes' traveled distances and corresponding Raman shift. Using this method, we determined that the radial outward flow and the AuNF-analytes interactions are two major factors affecting the mass transport of arsenic compounds to AuNF during the formation of the CRE deposit. The radial flow is generally manipulated by changing the atmospheric pressure, which influences the solvent evaporation rate and, consequently, the magnitude of the radial outward flow replenishing the evaporating liquid at the edge of the drying droplet. Considering the arsenical-AuNF interactions, we have shown, that once the arsenicals are deprotonated (pH > pKa), the interactions between analytes and AuNF become stronger (Gibbs free energy turn out to be more negative). This increases the retardation factor that enhances the diffusion coefficient and sorption of analytes (diffusion flux) to the AuNF surface, leading to the increase of mass transfer from the bulk to the surface and the decrease of the traveled distance of the individual arsenic compounds. In this work we have applied this theoretical approach for the DAR and DMAC speciation, thus providing the alternative method for the successful identification of the arsenic-based S-conjugated peptides.

The capillary flow or the radial outward flow is the major factor affecting the CRE deposit formation[1]. Once a droplet is placed onto the solid substrate and the solvent evaporation started, the radial outward flow is generated to replenish the solvent loss at the three-phase contact line[8]. This flow is linearly proportional to the evaporation rate of the droplet solvent and inversely proportional to the density of the solution[17]. Generally, as the evaporation time decreases, the radial flow rate increases, increasing the individual compounds traveled distances across AuNF. Furthermore, we have investigated the decrease of the evaporation time (30min → 2 min) onto the traveled distances of the individual DAR and DMAC (**Table 5**). As expected, this led to the increase of both DAR and DMAC traveled distances, even though the DAR's rise was smaller than DMAC's suggesting that other factors might have influenced the final deposition of DAR and DMAC as well. Then, to maximize the separation efficiency, we have determined the optimal evaporation time, and, thus the radial flow velocity of the individual compounds. The optimal radial flow rate was found at 20 min corresponding to the maxima of the selectivity factor (**Figure 24**).

Table 5. The influence of the evaporation time onto the traveled distances of DAR and DMAC.

Radial flow (time of evaporation)	Distance traveled (from the center to the edge)		
	DMAC, mm	Dar, mm	Solvent front, mm
35 min	4.20	3.20	
30 min	4.30	3.50	
25 min	4.30	3.60	
20 min	4.70	3.70	5.00
15 min	4.80	4.50	
10 min	4.90	4.80	
5 min	4.90	4.80	

The travel distances of DAR and DMAC depend upon the radial flow velocity, which is linearly proportional to the evaporation rate of a droplet solvent. By reducing the atmospheric and, in turn increasing the evaporation rate from 35 to 2 min, we have detected the travelled distances increase for both DAR and DMAC: 1.60 mm (3.20-4.80 mm) and 0.70 mm (4.20-4.70 mm), respectively.

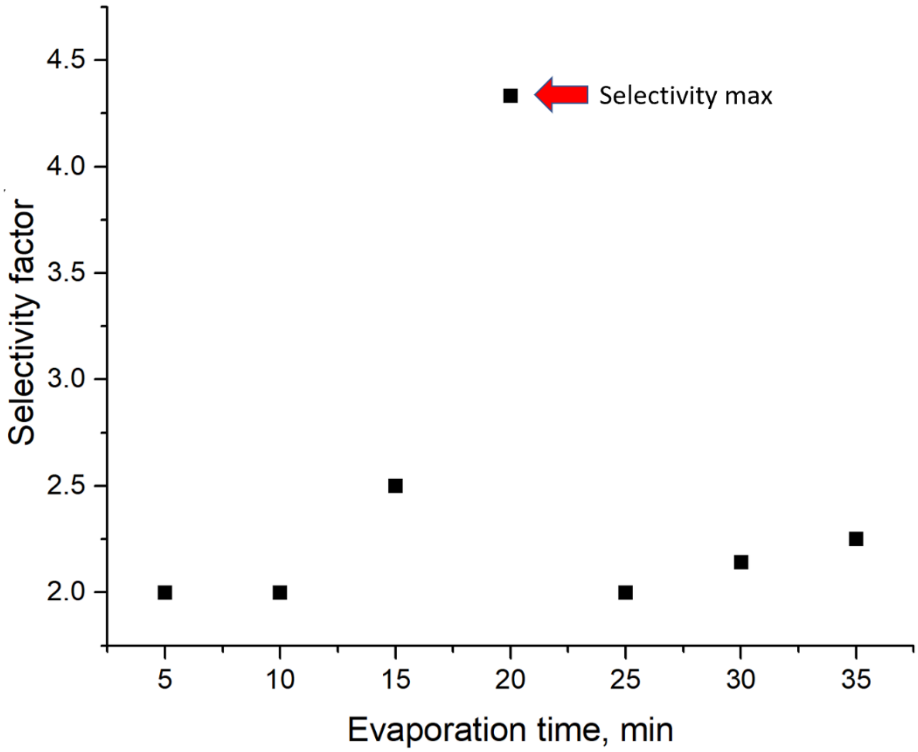

Figure 24. The influence of the evaporation time onto the Dar and DMAC's selectivity factor.

After plotting a selectivity factor (alpha) against the evaporation time, we have obtained the selectivity maxima (20 min) DMAC and DAR' mixture. which corresponds to the optimal radial velocity rate of the solvent across AuNF. The travel distances of DAR and DMAC depend upon the radial flow velocity, which is linearly proportional to the evaporation rate of a droplet solvent. By reducing the atmospheric and, in turn increasing the evaporation rate from 35 to 2 min, we have detected the traveled distances increase for both DAR and DMAC: 1.60 mm (3.20-4.80 mm) and 0.70 mm (4.20-4.70 mm), respectively.

Besides the radial outward flow, DAR/DMAC-AuNF interactions significantly influence the DAR and DMAC's migration distances. In the previous study, we have shown that the Au – S donor-acceptor interactions considerably affect the adsorption of thioarsenicals to the AuNF surface. Indeed, As – S can complex with the AuNF surface through the formation of As – S – Au adsorbate as thiol and sulfur-containing compounds readily adsorbed onto Au atoms forming a covalent Au – S conjugates.

Table 6. The pKa's of DMAC and DAR.

pKa	DMAC	DAR
-COOH (1)	1.95	3.58
$-NH_2$ (1)	9.14	13.42
-COOH (2)	-	1.47
$-NH_2$ (2)	-	9.31

Both DAR and DMAC have shown the adsorption to the AuNF surface resulting in the SERS peak at 265 cm^{-1} associated with the Au – S symmetrical stretching. In addition to covalent interactions, electrostatic repulsion/attraction between neutral/deprotonated forms of DAR/DMAC and negatively charged AuNF surface might influence the analytes' migration distances, thus, by calculating pKa's of DAR and DMAC functional groups (**Figure 25**) we explored the effect of pH (from 3 to 7) onto the traveled distances of individual DAR and DMAC (**Table 6**).

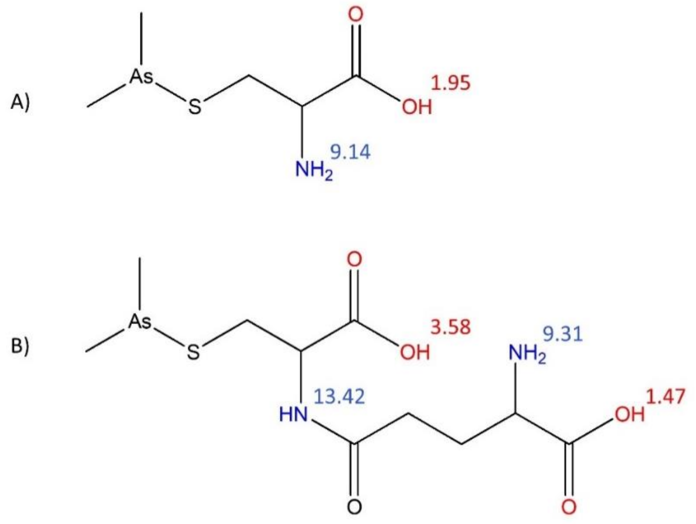

Figure 25. The structures of A) DMAC and B) DAR with calculated pKa’s.

Computed pKa’s of DMAC and DAR are summarized in the **Table 6**. pKa’s of DMAC and DAR were calculated by the Marvin Sketch[223], a computational software that was previously employed for the As^{V}, DMA^{V}, $MMA^{V,}$ and As^{III} pKa’s analysis. The data reported are in agreement with the experimental values of the oxoarsenicals[128].

Table 6. The influence of the pH on the travel distances of DAR and DMAC.

pH	Distance traveled (from the center to the edge)		
	DMAC, mm	DAR, mm	Solvent front, mm
3	4.90	4.70	5.00
4	4.80	3.40	
5	4.50	3.20	
6	4.20	3.20	
7	4.20	3.20	

The traveled distances of DMAC and DAR were evaluated in the pH range from 3 to 7. The traveled distance of the solvent (water) accounted for 5.00 mm. Once pH increases, deprotonation of DAR and DMAC resulted in a decrease of their traveled distance, which is in agreement with the previous data for thioarsenicals and oxoarsenicals[152].

In the previous studies we have determined that once pH increases and molecules are deprotonated, the traveled distances become shorter. Considering DAR and DMAC traveled behavior, this implies that as pH increases, the traveled distances of individual molecules become shorter which night attributed to the electrostatic interactions between the charged COO^- / NH_3^+ ionic pairs and the AuNF surface citrate molecules resulting in the formation of the hydrogen bond conjugates[205]. We propose that the number of the ionic COO^- / NH_3^+ pairs might contribute to the adsorption of DMAC and DAR onto the AuNF surface. Thus, Dar bears two COO^- / NH_3^+ ionic pairs whereas DMAC has only one group. By creating pH windows, we plotted the selectivity factor(alpha) against pH, and we determined that pH=4 of the mobile phase corresponds to the max resolution of the CRE-SERS chromatographic system (**Figure 26**).

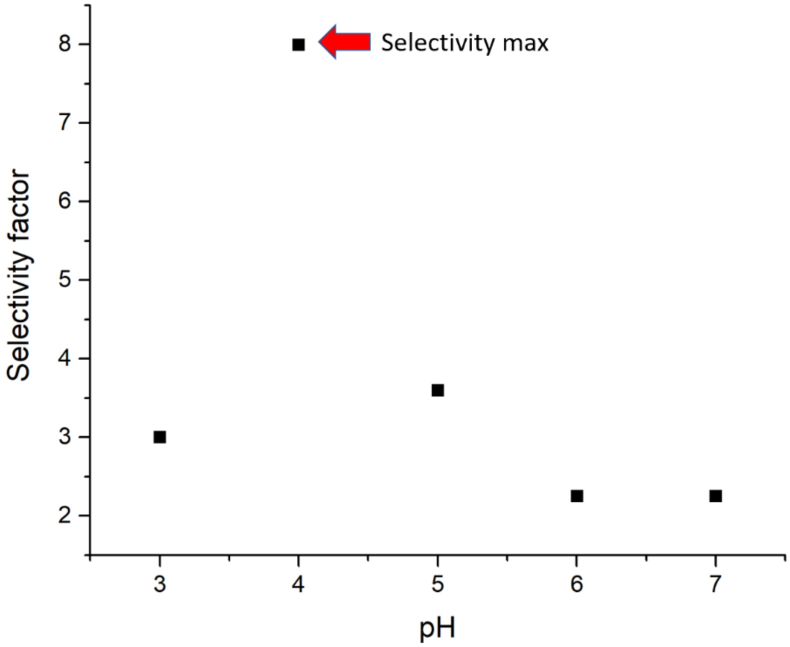

Figure 26. pH windows for Dar and DMAC for the optimal pH We have created the pH windows for the optimization of the DMAC and DAR separation by plotting the chromatographic selectivity factor (alpha) against pH.

We hypostasize that the discrepancy in the molecular size of DAR and DMAC could contribute to the separation as well. Typically, the smaller the molecule, the longer distance it would travel as it would be more affected by the radial outward flow[224]. Even though in the previous studies we have not considered this factor due to the similarity and minimality of small molecules, in the case of peptides (DAR and DMAC) separation, however, the larger molecular size of DAR (10.484 Å) might result in its shorter traveled distance in contrast to smaller DMAC (6.696 Å) that might have been more influenced by the radial flow and be detected mostly in the edge region, while DAR was found mostly in the center and the edge regions (**Figure 27**).

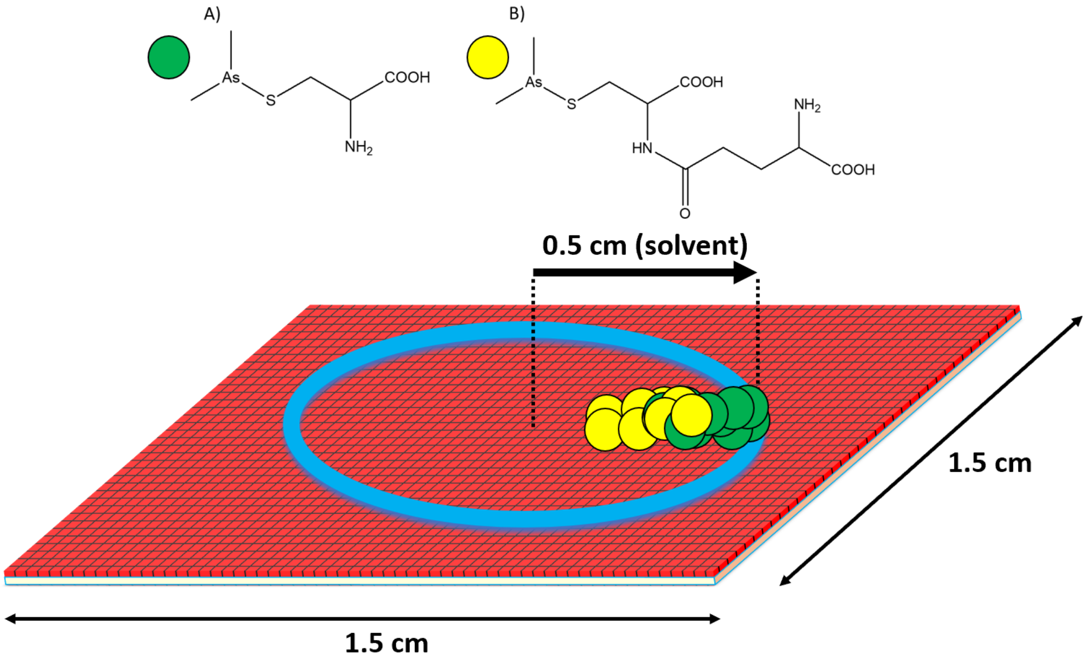

Figure 27. The final positions of the DAR and DMAC. Once the droplet dried, the SERS measurements were carried out from the center to the edge across the CRE stain.

Overall, we have successfully separated DAR and DMAC by exploiting their distinct interactions with AuNF. We have determined the optimal conditions for the separation of these analytes: pH=4, ν_{rad} = 20 min. Even though the SERS spectra of DAR and DMAC overlapped to some extent, SERS allows us to selectively identify each compound by comparing the Raman shift and the SERS intensities of the As – C and As – S symmetrical stretchings. Also, we calculated the SERS ratio of the As – C /As – S vibrational stretching of each compound: 12 and 0.9 for DAR and DMAC respectively. Based on the unique Raman shift and the SERS intensity of As – C and As – S symmetrical stretchings, we were able to identify each analyte in their mixture.

5.6 Conclusion

DAR is a novel organic arsenic compound that is being developed to improve the efficacy and therapeutic index of arsenic as an antineoplastic agent. DAR as an anticancer drug was successfully applied in APL treatment. The speciation of sulfur-containing drugs, DAR, and DMAC was investigated by the CRE– SERS method which comprises the coffee ring effect (CRE) and surface-enhanced Raman spectroscopy (SERS). SERS coupled with CRE requires minimal sample pretreatment and allows a nondestructive and simultaneous detection of multiple species due to their distinct vibrational fingerprints, thus presenting an alternative approach for the detection of fragile compounds. The application of the gold nanofilm enabled us to preserve the As^{III} oxidation state providing insight into the metabolism of unstable arsenicals. Once a sessile droplet is placed onto the gold nanofilm surface (AuNF) and the solvent evaporation started, the formation of a CRE stain begins. Two major factors affect the formation of the CRE deposit: the radial outward flow, the analyte-gold nanofilm (AuNF) interactions. We believe that the more ionic DAR (pH=4) interacted stronger with AuNF, resulting in the shorter traveled distance in comparison to DMAC, which was less attracted to the AuNF surface. In the final CRE deposit, we have found DAR in the center and the middle regions, whereas DMAC was detected primarily in the middle and the edge regions the final CRE deposit, DAR was detected in the center and the middle regions, whereas DMAC traveled longer distances across the CRE stain and primarily was detected in the middle and the edge region. We were able to identify individual DAR and DMAC despite the overlap of their Raman spectra due to the unique Raman intensity of the individual compounds. For the analytes that might not be separated by the CRE, SERS provides an additional advantage to identify the species, by selectively adjusting the pH of mobile phase to induce the SERS shift of the adsorbed species onto AuNF allowing the detection of the species with a similar Raman shift and those that cannot be separated by the CRE. The key advantage of the application of this method for the peptide's separation is the separation coupled with the mild detection providing the rich structural information of each metabolite.

Chapter 6. pH-dependent Raman shift: theory and experiment

6.1 Abstract

Surface-enhanced Raman scattering (SERS) is a very sensitive technique that reveals structural molecular information based on the unique vibrational fingerprint. While the SERS sensitivity mostly relies on the plasmonic nanomaterials electromagnetic enhancements, chemical enhancement mechanisms that are more sensitive to molecular adsorption and intermolecular interactions have been less exploited for molecular detection. The citrate coated gold nanoparticles are the mostly employed nanomaterials for the development of the nano-based sensors. Raman shift is the key parameter for the evaluation of the molecular adsorption onto the nanomaterial surface. Here I present the unified approach to predict the Raman shift variations of the small molecules adsorbed onto a gold nanofilm (AuNF). I have employed three common arsenic species: DMA^{V}, $DMMTA^{V}$, and $DMDTA^{V}$ as a model for theory development. By theoretically calculated interactions energies of species with Au cluster, I extrapolated this to the predictions of the pH dependent Raman shift variations for the unknown arsenic species. Moreover, I have classified the interactions of the various molecules with the citrate coated gold nanoparticles. As pH increases and especially when it overcomes pKa, charge transfer becomes more favorable leading to the stronger interactions of molecules with AuNF surface. I also defined the interactions of molecules with AuNF surface, and experimentally determined the molecule-AuNF covalent and electrostatic interactions, providing a model for the prediction of the interactions based on the molecular charge and the variations of the Raman shift.

Keywords: SERS, Raman shift, adsorption, spectroscopy

6.2 Introduction

Surface-enhanced Raman spectroscopy (SERS) is a non-destructive and sensitive method for the detection of biological compounds based on their distinct vibrational fingerprint. Exploring the ultra-sensitive Raman capability, there is a growing interest in the single-molecule detection in a complex biological matrix[225], design of the immunoassays for disease monitoring[226], including the development of the analytical applications for chemical warfare agents, small molecules, and pollutants sensing[227]. The unique SERS effect emergences from the ability of the metallic substrate to support the propagation of surface plasmons electromagnetic waves[228]. These surface plasmons enable amplification of the inherently weak Raman signal by providing an increased electric field in the vicinity of the target molecule and the nanomaterial. SERS enhancements result from excitation of these surface plasmons by the incident radiation: at the plasmon frequency, the metal becomes highly polarizable, resulting in large field-induced polarizations. The origin of the enhanced Raman signal related to the two major mechanisms: (a) an electromagnetic enhancement (EE) originated in the vicinity of the metal surfaces caused by electromagnetic resonances and (b) a chemical enhancement (CE) involving a process related to the chemical or physical adsorptions between the molecule and the metal surface. The major contribution to EE is associated with the surface plasmons propagation by the collective oscillations of surface conductive electrons onto the metal surface involving the localization and amplification of incident light fields by a surface plasmon resonance enabling a single molecule detection with EF up to 10^{14}[229]. That is, a close interaction of two or more plasmonic objects provides the concentration of an incident electromagnetic field and effectively amplifies the near field between and around the nanostructures[230]. The CE occurs by the charge transfer effect associated with the overlap of metal and adsorbate electronic orbitals, which induces a light-dependent electron density transfer process. In this model, an electron of the metal, excited by the incident photon, transfers into an excited state of the adsorbed molecule resulting in the distinct adsorbate geometry comparing to the of the neutral adsorbate molecule. Therefore, the charge-transfer induces a nuclear relaxation in the adsorbate molecule which promotes the emission of a Raman dependent eradiation[231].

The EE of the plasmonic nanomaterial has been extensively investigated and is well understood. Other aspects, such as the contribution of CE, are less known and are currently topics of intensive research. Previous single-molecule studies have provided important understandings into the EE mechanism[232]; however, little is known about the practical implementations of the Raman shift related to the chemical enhancement. It is widely known that pH governs the red and the blue Raman shift of the SERS spectra[233], providing insights into the specific interactions between the nanomaterial and the adsorbates. However, the unified theoretical approach regarding the pH dependence of the Raman shift is lacking. In most of the studies, the time-consuming approaches were employed for the theoretical calculations of the geometrical constraints of the adsorbate-molecule complexes before the experimental procedures[234, 235]. Also, the theoretical models often fail to predict the exact molecular orientation of the analytes onto the surface of the nanoparticles as in the computational studies they consider only the metal cluster without the adsorbed stabilizers that might influence the interactions of analytes with nanoparticles surface[236]. For example, the citrate gold coated gold nanoparticles often regarded as a bare gold cluster Au(111) omitting the negatively charged citrate molecules due to the computational limitations, thus the information of how citrate influence the adsorption, and what types of the interactions it is responsible for of the analytes onto the AuNPs surface remain unknown[237].

Previously, we have determined the pH dependency of the Raman shift in arsenical-AuNF interactions. We have shown that the traveled distance in nano chromatographical separation dependent upon the molecular charge, guiding the adsorption of the analytes onto the surface of the nanoparticles[238]. Typically, once pH overcomes pKa the analytes traveled distances across the AuNF surface decreases, thus in contrast to the neutral ones, deprotonated molecules adsorbed stronger onto the AuNF surface. We have shown that the adsorption of the analyte is related to the Gibbs free energy of the analytes-AuNF interactions providing the highest Raman shift values for charged molecules. We hypostasize that pH dependent variations of the Raman shift might be the key components to investigate the adsorption mechanisms of the analytes onto the nanoparticles surface and to provide an understanding of the type of molecule-nanomaterials interactions (donor-acceptor, covalent, electrostatic, hydrogen bonding) occurred near and onto the surface of the nanoparticles.

In this paper, we have developed the theoretical approach that allows us to predict the interactions between adsorbates and AuNF based solely on the experimental values of the Raman shift. Firstly, we have calculated the energy of the adsorbate-AuNF complexes, following the pH changes, then we have related the adsorption of the analytes and their

Raman shift dependence. We have found that the adsorption of arsenicals depend upon the nature of the atomic makeup which governs the donor-acceptor interactions if the molecule is adsorbed directly to the AuNPs leading to the covalent bond formation, and the charge that enables the charge transfer from the adsorbates to the gold surface, and the electrostatic interactions in the case where a molecule does not directly bind tp the Au surface but is placed in the vicinity of the bare Au cluster interacting primarily with the negatively charged citrate molecules. That would allow us to recognize the binding energies and predict the value of the analytes' Raman shift based on the structure of the analyte in the different environments understanding the metabolism of the specific compounds. Here we propose to selectively tune the Raman shift variations to investigate and predict the interactions between the AuNF and the arsenicals, based on those observations we can predict the pKa of the individual compounds and their adsorption allowing us to assess through what forces adsorption occurred providing insights upon the binding mechanisms of analytes to the AuNF surface, without prior calculations and based solely onto the experimental approach. The typical models were developed for the comparison between the experimental and the theoretical values to support the experimental values of the Raman shift.

6.3 Experimental procedures

6.3.1 Materials and chemical

Cacodylic acid sodium salt, 98% (DMA^V), NaOH, HCl, Citric acid, Sodium citrate dihydrate (Granular certified), (3-Aminopropyl)trimethoxysilane (APTMS), glass microscope slides, weighing boats, and 25 ml glass vials were purchased from Fisher scientific Inc (Hampton, NH). The citrate buffer (pH=3-7) was fabricated by mixing Citric acid and Sodium citrate. All solutions were prepared in deionized (DI) water (18.2 MΩ, Barnstead Nanopure Diamond).

6.3.2 Instrumentation

The Raman spectrometer was purchased from Jasko (NRS-4100), with a diode laser at 785 nm and average power of 33 mW. For optimizing resolving power, the 100 × optical lens focusing was used. A silicon wafer was employed to calibrate the Raman system at daily use and the Raman signal intensity at 522 cm^{-1} was monitored to check the reproducibility of the instrument. The SERS measurement parameters include the laser wavelength, 785 nm, exposure time, 4 seconds, and 1 time of exposure per measurement. The synthesis of thioarsenicals and determination of their respective Raman spectra were performed in the previous reports[130, 131].

The fabrication of AuNF was performed through the silanization of the glass substrates, followed by the deposition of nanoparticles onto the silanized surface[143]. Immediately after the droplet contained 100 mg L^{-1} of arsenic ligands deposition onto the gold nanofilm, the droplet was freeze dried and the Raman spectra were collected. The adsorption of arsenic species onto the AuNF was carried out at pH = 3 and pH = 7, in the concentration range from 10^{-3} to 10^{-9} mol L^{-1}.

6.3.3 Synthesis of thioarsenicals and determination of their respective Raman spectra

6.3.3.1 Synthesis of Dimethylmonothioarsenious acid (DMMTA^{V})

DMMTA^{V} was synthesized according to the method reported by Cullen et al[130]. Briefly, DMA^{V} (2.76 g) and sodium $Na_2S * 9H_2O$ (7.60 g) was dissolved in 30 mL of water. Concentrated H_2SO_4 (1.70 mL) was added dropwise to the solution to make the molar ratio of Na_2S/H_2SO_4/DMA^{V} was 1.6:1.6:1. The reaction mixture was stirred for 1 hour and was extracted with ether and was dried over anhydrous Na_2SO_4. The ether was evaporated under N_2 and colorless crystals were formed. Raman spectra determined of both solid and liquid forms (citrate buffer solution, pH=3) of DMMTA^{V} were identical.

6.3.3.2 Dimethyldithioarsenious acid (DMDTA^{V})

Dimethyldithioarsenious acid (DMDTA^{V}) was synthesized by the approach reported by Fricke et al.[132] Briefly, cacodylic acid (1.01 g) and NaOH (0.29 g) were dissolved in boiling ethanol (12.5 mL). Hydrogen sulfide was bubbled into the boiling solution for 30 min, and a white solid precipitated. After cooling, colorless crystals were isolated by filtration and air-dried. Raman spectra determined of both solid and liquid forms (citrate buffer solution, pH=3) of DMDTA^{V} (salt form) were identical.

6.3.3.3 Synthesis of DMAC

DMAC complex was prepared by reduction using a mixture of DMA^V (0.66 mmol) with L-cysteine (0.33 mmol) in 10 ml of degassed DI water under nitrogen[129]. The reaction was carried out at room temperature using magnetic stirring for three hours[19]. After the reaction, the solution was centrifuged, and the supernatant was collected. After the supernatant evaporation, the white residue powder was carefully collected for further analysis.

6.3.3.4 Synthesis of DAR

DAR was synthesized according to previously published procedures with minor modifications[219]. Briefly, DMA^V (2 mmol) and GSH (6 mmol) were dissolved in 10 mL deionized water, and the solution was stirred overnight under a nitrogen atmosphere. Then, the water was evaporated under reduced pressure without heating using a centrifugal concentrator. DAR was then extracted from the residue using ice-cold methanol. A white powder was obtained after methanol evaporation, following the further drying and storage into a desiccator.

6.3.4 Adsorption of arsenicals

Once the 2μL arsenicals buffer solution of pH range from 2 to 7 was placed onto the AuNF, the average SERS signal of arsenicals were acquired from the center to the edge of the dried deposit (n=3). The SERS intensities for the quantitative analysis were normalized by the background correction.

6.4 The theory development

Typically, charged and neutral species differ in their adsorption process onto the surface of the nanoparticles: this process involves the addition or removal of nonbonding electrons contributing to the distinct structures of adsorbates. To quantify structure-change-related CE rate effects, two parameters are required: the vibrational frequency, ν, and the unitless normal-coordinate displacement, Δ. Note that a displacement value of 1 corresponds to one standard deviation of the Gaussian probability distribution of the ground-state vibrational wave function. Furthermore, we need this information for every Franck-Condon active vibrational mode that is, every vibrational mode that experiences a change in normal coordinates when an electron is transferred. In **Figure 28**, the normal-coordinate displacement is represented as a displacement of reactant and product curves along the horizontal axis, i.e., the traditional reaction-coordinate axis. For the metal-ligand complexation, the energy barrier needed to be overcome is illustrated as follows[239]:

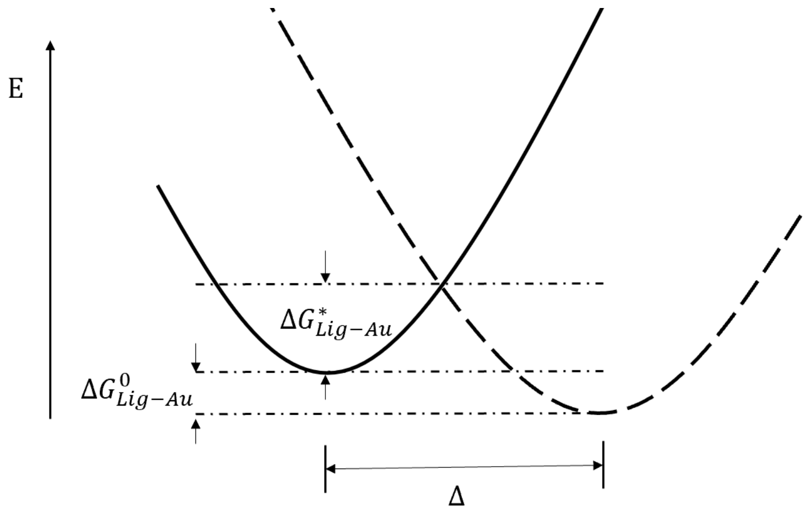

Figure 28. Energy surface and its relationship to the free energy driving force (ΔG^{0}_{Lig-Au}), classical activation energy (ΔG^{*}_{Lig-Au}) and vibrational mode displacement (Δ) for electron transfer.

The frequency, on the other hand, is reflected in the degree of curvature of the energy surfaces. To describe the charge transfer reactions, we need to determine the bond reorganization that originates from the oxidation state changes during the adsorption process. The charge transfer occurs when the displacement of the coordinates varies by reduction or stretching of the bonds. The energy required to overcome the vibrational barrier can be computed from the vibrational coordinate displacement (Δ_k) of the vibrational frequency (v_k) as

$$\Delta G_v^{*} = \frac{1}{8}\sum_k \Delta_k^2 v_k \tag{6.1)}$$

or by the bond displacement (Δa_j) of the force constant (f_j) as

$$\Delta G_v^{*} = \frac{1}{2}\sum_j b_j\left(\Delta {a_j}^2\right) f_j \tag{6.2)}$$

the individual normal coordinate distribution is given[233] as

$$\Delta G_v^* = \frac{1}{2}\Delta_k^2 v_k \qquad 6.3)$$

Thus, the free energy driving force of Gibbs free energy is proportional to the corresponding to vibrational coordinate displacement (Δ_k) and the vibrational frequency (v_k) or the adsorption Gibbs free energy, that defines the difference between the ligand and the ligand-adsorbate Raman shift.

6.5 Results

6.5.1 Theoretical and experimental Gibbs free energy of Au-arsenicals complexation.

The Gibbs free energy of arsenicals adsorption onto the AuNF surface was calculated based on their adsorption Langmuir isotherms. To compare with the experimental values of arsenical-Au complexes, we have computed (DFT) the theoretical Gibbs free energy and summarized in **Table 7**. The negatively charged arsenic-Au complexes (DMA^{V-}-Au, DMMTA^{V-}-Au, DMDTA^{V-}-Au) showed the lower Gibbs free energy and, thus, the higher binding affinity to the AuNF in contrast to the neutral adsorbates (DMA^{V}-Au, DMMTA^{V}-Au). The calculated energies were lower than the literature data for the similar sulfur-containing compounds mainly because of the computational constraints; only three molecules of water were added for the solvation simulation of the arsenicals-AuNF complexes. However, even with the limited solvation, the experimental data correlate with the theoretical values: the adsorption of the sulfur-containing arsenicals (DMMTA^{V}-Au, DMMTA^{V-}-Au, DMDTA^{V-}-Au) regardless of the molecular charge was chemisorption like the process in agreement with the literature data for the thiols and sulfides chemisorption adsorption onto the AuNF surface (6-14 kcal), whereas oxygen-containing arsenicals (DMA^{V}-Au, DMA^{V-}-Au) demonstrated physisorption (with Gibbs free energies less than 6 kcal)[184, 204].

Table 7. pH dependent Raman shift.

Arsenical	ΔG_{tot} (DFT) (in vacuo) (kcal/mol)	ΔG_{tot} (DFT) (water) (kcal/mol)	ΔG_{tot} (Experimental) (kcal/mol)	K_{ad} (Experimental) (mol^{-1})	Raman shift, cm^{-1}	
					As – C	As – S
DMA^{V}-Au	-7.1	-7.1	-4.8	3.7×10^{3}	1±1.0	-
DMA^{V-}-Au	-31.5	-24.5	-5.2	7.0×10^{3}	-5±1.5	-
$DMMTA^{V}$-Au	-19	-19	-6.1	3.0×10^{4}	16±2.0	4±2.0
$DMMTA^{V-}$-Au	-45	-30.4	-8.7	2.5×10^{6}	20±2.0	14±2.0
$DMDTA^{V-}$-Au	-40.5	-44.2	-11.4	1.5×10^{8}	27±2.0	18±2.0

6.5.2 The regression model for the understanding of the correlation between the charge transfer effect and the pH

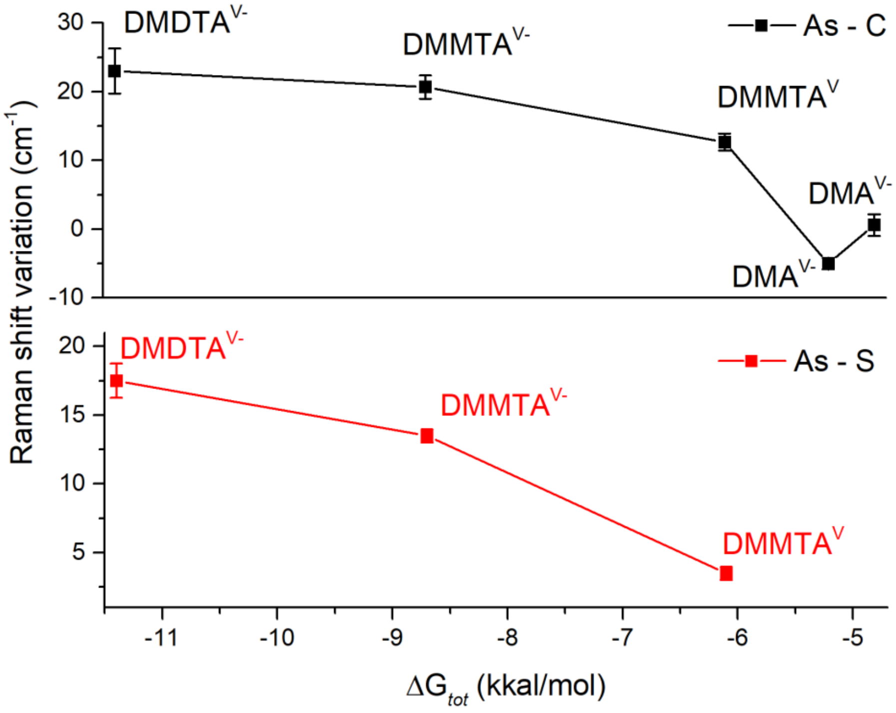

Figure 29. The relationship between the Gibbs free energy and the Raman shift variations for the As – S and the As – C vibrational stretching's of DMDTA^{V}—Au, DMMTA^{V}—Au, DMMTA^{V}-Au, DMA^{V}—Au, and DMA^{V}-Au.

According to the Heraberg-Teller selection rule, the charge transfer occurs only when the excitation energy approaches the charge-transfer resonance[240]. The adsorption of thiols onto the Au(111) cluster is very well studied, those HOMO/LUMO interactions of the thiols and the substrate typically involve the charge transfer from the HOMO 3pz of the sulfur and the Au 6s orbitals[241]. It is seen that the major contributions to energy levels nearest the HOMO-LUMO gap arise from the gold cluster 5d and 6s bands. The sulfur 3s contributions to the LUMO and HOMO-1 levels are small in comparison to the gold orbital contributions[242]. Besides, we have performed Mulliken population analysis to examine the atomic charges of the arsenical-Au complexes. The charge variation on the sulfur atom in the range of DMDTA^{V-}—Au, DMMTA^{V-}—Au, DMMTA^{V}-Au in comparison to free thioarsenicals (DMDTA^{V-}, DMMTA^{V-}, DMMTA^{V}) were found to be -0.11e, -0.43e, -0.44e indicating the theoretically calculated charge transfer between the S and Au atoms which is in correspondence with the Raman shift variation with Gibbs free energy changes displayed in **Figure 29**. The charge transfer value on sulfur is in agreement with previous studies of Sellers et al. who found a charge of 0.40 electron (MBPT2/DZ) on sulfur[243] and Beardmore et al. who obtained a charge of 0.42 electron (B-LYP/6-31G*) on the sulfur atom[244]. The potential discrepancies in the computed S atomic charges on sulfur might be due to the various theoretical methods and the different basis sets employed (**Figure 30**).

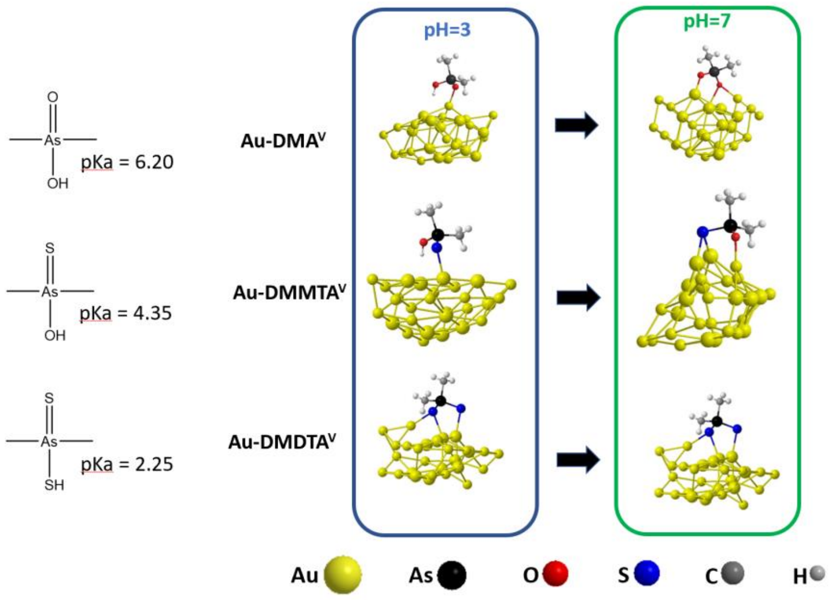

Figure 30. Structure optimization Ligand-Au clusters by Q-Chem 4 with a hybrid functional B3LYP, LANL2DZ-P), and their pH dependent adsorption onto the Au(111) cluster at pH=3 and pH=7.

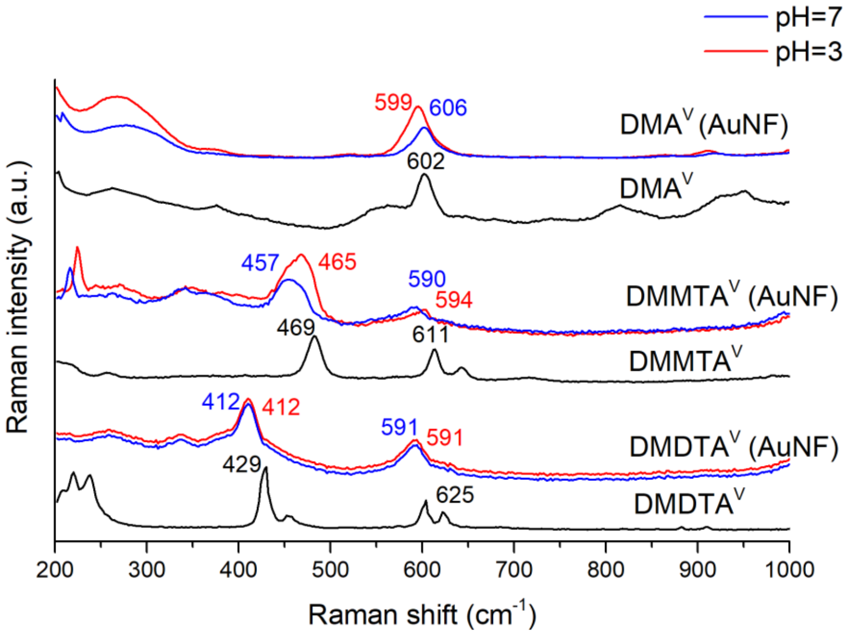

Figure 31. Raman shift of DMA^{V}, DMMTA^{V}, and DMDTA^{V} onto the AuNF at pH = 3, and pH = 7.

The Raman shift indicates the magnitude of the charge transfer between the AuNF surface and the adsorbates. The higher the Raman shift, the stronger interactions between the analytes and the AuNF. We have ranged the pH from 3 to 7 and compared the SERS spectra of DMA^{V}, DMMTA^{V}, and DMDTA^{V} with the Raman spectra of the solid compounds. The SERS signal for each compound was obtained from the CRE stain formed after the deposition of the droplet contained 2 µl of the citrate buffer at pH ranging from 3 to 7, after the solvent evaporation the CRE deposit was stained across the center, middle, and the edge region and the most intense signal very taken into consideration.

As seen from the **Figure 31**, Raman spectra of solid DMA^{V} exhibit two major bands, corresponding to As – C asymmetric stretching (602 cm^{-1}) and As – O stretching (830 cm^{-1}) Regarding DMA^{V} neutral form (pH=3), the Raman shift of the As – C symmetrical stretching occurred at (602 cm^{-1} to 600 cm^{-1}), however as the pH increases, the shift changed significantly, increasing by up to 606 cm^{-1} as shown in **Table 3**. Interestingly, the As – O stretching (830 cm^{-1}) disappeared from the SERS spectra with adsorption to AuNF, which might be because of the out of plane orientation of As – O stretching on the AuNF or even because that DMA^{V} could not bind to the surface of the nanoparticles and remains located in the vicinity of the AuNF interacting with the AuNF surface via citrate molecules through hydrogen bonding.

Considering the DMMTA^{V} adsorption in the pH range from 3 to 7, the pH greatly affects the Raman shift of the As=S stretching through the interaction with the AuNF. In contrast to the solid form of DMMTA^{V} having the As=S stretching at 469 cm^{-1}, at pH=3 the major vibration band was shifted to 465 cm^{-1}. As the pH increases, the Raman shift becomes larger (12 cm^{-1}) illustrating stronger adsorption of the deprotonated form than that of the neutral $DMMTA^{V}$. This is supported by the theoretical calculations of $DMMTA^{V}$'s neutral and negatively charged forms via adsorption onto the Au cluster (**Table 7**). The binding energy of the deprotonated form of $DMMTA^{V}$ is considerably higher than that of the neutral form, thus, binding to the gold surface via S – Au interactions influenced the Raman shift. Similar to As=S stretching, the As – C stretching exhibited the Raman shift of (17 cm^{-1} – 20 cm^{-1}) as the pH increases from 3 to 7 indicating a stronger interaction of $DMMTA^{V}$ with the AuNF surface.

$DMDTA^{V}$ did not exhibit any significant variation in the SERS adsorption behavior throughout the pH range. The main reason for the Raman shift stability is the highest binding energy among all arsenicals tested, which corresponds to the highest Raman shift of the As÷S bond from 429 cm^{-1} as a solid to 412 cm^{-1} as adsorbed onto AuNF. The presence of two delocalized electronic structures of the S÷As÷S fragment greatly enhances the binding capacity of $DMDTA^{V}$ to the AuNF surface. Even though the Raman shift of As – C vibrational stretching was larger than those for DMA^{V} and $DMMTA^{V}$, it does not change with increasing pH. In Figure 34, $DMDTA^{V}$ As – C stretching showed a mixed Raman shift from As – C asymmetrical stretching at 625 cm^{-1} and symmetrical stretching at 604 cm^{-1} to 591 cm^{-1}, which is the largest Raman shift among all analytes due to the highest affinity to the AuNF. In addition, the Raman shift of As – C asymmetrical stretching of DMA^{V} was much smaller (3 cm^{-1}) than that of thioarsenicals: $DMMTA^{V}$ (17 cm^{-1}) and $DMDTA^{V}$ (27 cm^{-1}).

6.5.3 The prediction of the Raman shift or the DAR and DMAC. SERS spectra

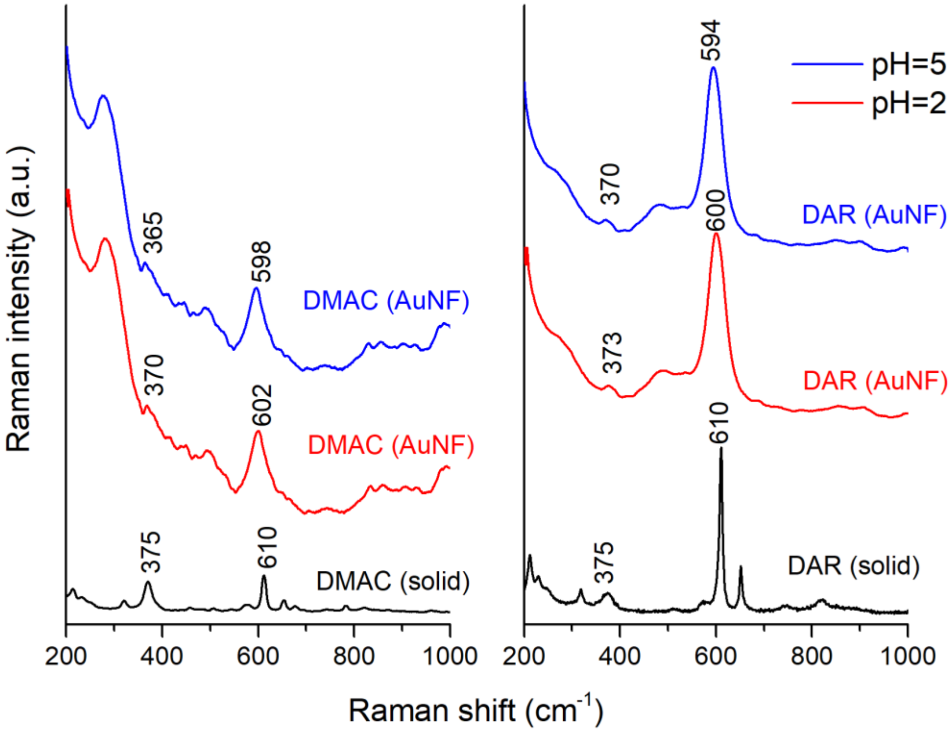

Figure 32. A) DMAC and DAR Raman and SERS spectra onto the AuNF surface at pH=2, 5.

Comparing the Raman and SERS spectra of DAR, the pH dependent red Raman shift occurred for As – C fingerprint vibrational stretching's: 10 cm^{-1} (610 cm^{-1} → 600 cm^{-1}) and 16 cm^{-1} (610 cm^{-1} → 594 cm^{-1}) at pH=2 and pH=5 respectively. Similarly to DAR, DMAC's As – C frequency change was 8 cm^{-1} (610 cm^{-1} → 602 cm^{-1}) at pH =2, and 12 cm^{-1} (610 cm^{-1} → 598 cm^{-1}) at pH =2 and pH =5 respectively, which indicates the charge transfer effect between the DAR molecule and the AuNF surface (**Figure 32**)[148]. Considering the As – S vibrational stretching's, DAR's the red shift accounted for 2 cm^{-1} (375 cm^{-1} → 373 cm^{-1}) and 5 cm^{-1} (375 cm^{-1} → 370 cm^{-1}) at pH=2 and pH=5 respectively.

DMAC's As – S was shifted to the lower frequency as well: 5 cm^{-1} (375 cm^{-1} → 370 cm^{-1}) and 10 cm^{-1} (375 cm^{-1} → 365 cm^{-1}) at pH=2 and pH=5 respectively. It is clear that the DMAC's As – S and As – C Raman vibrational shift was higher than that of DAR's indicating that DMAC might interact stronger with the AuNF. The final positions of the arsenicals at pH=3 and pH = 7 are depicted in **Figure 33**.

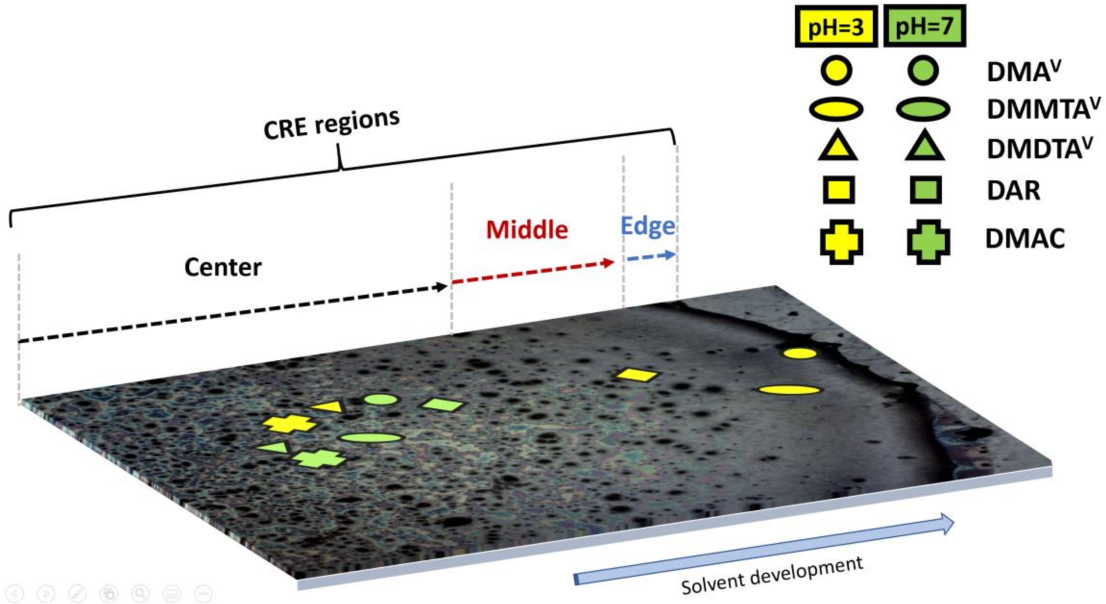

Figure 33. SERS signal spectra obtained at the various spots across the CRE regions corresponding to the maximum SERS intensity.

6.6 Discussion

In this paper, we have presented the theory behind the pH driven Raman shift by examining the various types of interactions driven by the charge transfer of the arsenic ligands to the AuNF surface. Generally, once the analytes pKa's were calculated, we have manipulated solution pH to deprotonate arsenicals, which in turn induced their adsorption onto the AuNF leading to pH dependent Raman shift. The specificity of the arsenical-AuNF interactions governs the adsorption of molecules onto the AuNF surface and the charge transfer between the molecules and the Au atoms through replacement of the citrate or the electrostatic or hydrogen bonding interaction with negatively charged citrate molecules. The Raman shift values allow us to identify each of the metabolites and to determine the value of the Raman shift corresponding to the specific interaction types, following the determination of the interactions of the unknown arsenicals (DAR and DMAC).

According to the theoretical and the experimental values of Gibbs free energy, the general trend for the adsorption of arsenicals from the highest to the lowest adsorption values is the following: DMDTA $^{V-}$ - Au > DMMTA^{V-} - Au > DMMTA^{V} - Au > DMA^{V-} > DMA^{V} - Au, which is in agreement with the charge transfer that maximizes at the most charged species and the species that have the soft atoms thus providing the highest adsorption to the AuNF surface. The major factors affecting the arsenicals adsorption to the AuNF is the presence of the O or S atoms that directly interact with AuNF. It is well known that S is a soft ligand having a higher affinity to the soft Au atomic cluster whereas "harder" O does not display this affinity to the Au atoms, thus the species with S have higher binding energies and, consequently, higher Raman shift. Another factor is the molecular charge that promoting the charge transfer and thus contributing to the increase in the Raman shift. The charged species were found to have lower Gibbs free energies, and thus higher adsorption constants, consequently DMDTA^{V-}, DMMTA^{V-}, and DMA^{V-} interact stronger with AuNF in comparison to the neutral compounds (DMMTA^{V} , DMA^{V}). Interestingly, even though the atomic charge of DMA^{V} is negative, it has the positive Raman shift variation, which is not in agreement with the theoretical predictions which indicates that DMA is not directly adsorbed onto the Au cluster. We reason that there is no chemical shift of the As – O bond, and it mostly disappears from the SERS spectra, thus we propose that DMA^{V} is located in the vicinity of the citrate surface, interacting mostly with negatively charged citrate's COO- and COOH groups, forming the hydrogen bonding to the stabilizing agent. Regarding DMMTA^{V} and DMDTA^{V}, we have observed the Raman shift for the As – S vibrational stretching for DMDTA^{V-}, DMMTA^{V-} and DMMTA^{V} of 4, 14, 18 cm^{-1} respectively. The Raman shift of the charged arsenicals that have S in their molecule provided the highest Raman shift for As – C vibrations which correlates with the As – S Raman shift for the species. Interestingly, As – C DMA^{V} Raman shift accounted for the smallest value of 1 or -5 cm^{-1} (608 cm^{-1} from the 602 cm^{-1}), indicating the possible electrostatic interaction of its molecule and the substrate giving that its adsorption is not possible onto the AuNF surface because DMA^{V} could not substitute citrate molecule onto the Au atoms. For DMMTA^{V} and DMDTA^{V} we have identified their spectra only upon the As – C shift. And the largest Raman shift of As – C accounted for 27 cm^{-1} was found for DMDTA^{V-}, due to the strong covalent bond formation Au cluster.

Based on the theoretical approach we have developed for DMDTA^V, DMMTA^V, and DMA^V we have applied this theory for the calculations of the unknown arsenicals omitting the calculations step of the DAR and DMAC adsorption to the AuNF. We have found the corresponding As – C and As – S Raman shift value for both DAR and DMAC: The predicted As – C vibrational stretching Raman shift of DAR and DMAC: of 16 and 12 cm^{-1}, The predicted As – S vibrational stretching Raman shift of DAR and DMAC: of 5 and 10 cm^{-1}. Raman shift of the major DAR and DMAC vibrations (the As – S and the As – C symmetrical vibrational stretching's appeared mainly due to the high affinity of S-conjugated to Au atoms leading to the formation of the Au – S – As a cluster, which might orient the As – C bonds in out of plane direction (vertically) resulting in the relatively large Raman shift of the As – C stretching (610 cm^{-1} → 594 cm^{-1}) for DAR and (610 cm^{-1} → 598 cm^{-1}) for DMAC[222]. Interestingly, the Raman shift for DMAC' As – S stretching was larger than that of DAR: 10 cm^{-1} vs 5 cm^{-1} suggesting that DMAC might interact stronger with AuNF than DAR, which is in agreement with the sterically constrains of the DAR and DMAC, while DAR might not be adsorbed through the As – S moiety due to the steric hindrance of its molecule, bearing three amino acids, while for DMAC it was easier due to the less constrained molecular adsorbate. according to the pKa of DAR and DMAC, at pH=2, DMAC has only one COO^-/NH_3^+ however, at pH=5, two pairs become ionic. Thus, DMAC's COO^-/NH_3^+ would interact greater with the $COOH/COO^-$ group of the citrate providing the higher Raman shift.

This applicable model allows us to predict the Raman shift of the specific groups providing the possibility to identify them later or to understand their adsorption onto AuNF and predict the interactions of the analytes with the AuNF by examining the Raman shift values. We reason the behind the arsenicals adsorption onto AuNF stand the different interaction of the species with AuNF surface: donor-acceptor (DA), electrostatic (EL) van der Waals (LW). Depending on the presence in the arsenical molecule S atoms, it influences the DA interaction via the covalent bonding between the Au atoms and the arsenicals which are widely known. The molecular charge will also influence the adsorption capacity of the AuNF, as an example is DMMTA^{V}, which adsorption energy changes significantly during the deprotonation. In the case of the larger molecules such as DAR and DMAC, we need to consider the possible steric effect, which might hinder the adsorption of the analytes onto the Au(111) sites. Thus, based upon the adsorption of arsenicals onto the AuNF surface it is possible to predict the interactions of them with AuNF surface and vice versa. Identification of the analytes is the second advantage of this approach especially for those molecules that might not be separated by the CRE, the selective tuning of the Raman shift variations allows us to identify individual compounds.

6.6.2 The theoretical applications for the species adsorbed onto the citrate coated AuNPs

In this section, we have summarized the major concepts of the adsorption of the analyte onto the citrate coated gold nanoparticles, considering the various functional groups, their ability to substitute citrate onto the AuNF surface and we provide analytes-AuNF interaction types[245]. Most of the functional groups showed the pH dependent Raman spectra, meaning that during the deprotonation the nonbonding electrons transfer their charge from the functional groups to the AuNPs, resulting in the Raman shift variations. In general, by mixing the aromatic amines onto the AuNPs surface it was shown that $-NH_2$ was found to be more efficiently substituting citrate than $-COOH$ due to the lower binding energy of $-COOH$ (2 kcal) vs $-NH_3^+$ (8 kcal). Moreover, $-NH_3^+$ contributes to the electrostatic attraction to negatively charged citrates promoting the adsorptive overcoating of $-NH_3^+$ to AuNF surface, increasing the adsorption, in contrast to negatively charged $-COO^-$ that was mostly repelled by citrate molecules[246]. Also, typically the HS having a very high affinity to the substrate easily substitute citrate onto the AuNPs surface. Deprotonation of HS leads to the S^- which have been extensively reported and proven in our work promotes the charge transfer between the nonbonding electrons onto the S^- to the AuNPs resulting in a very strong covalent bond. For =N-/=NH- it was reported the mix of the covalent and the electrostatic interactions for the corresponding pair: = NH- ‘s proton would form the hydrogen bond between its moiety and the negatively charged COO^- citrate groups. = N- intern have the electronic pair that might interact be donated to them as a charge transfer to the AuNPs[247]. The OH/O^- have a week electrostatic interaction because of the negative surface charge of O^-, even though the OH was reported to forms the hydrogen bonding with the citrate molecules. The Raman shift mainly classified as red shift (to lower wavenumber, meaning that the electron density is transferred from the molecule to the AuNPs) or the blue shift indicating that gold d-orbitals provided the electrons and enriched the molecule by transferring the electrons from the Au atoms to the molecule’s orbitals.

The guest ligand efficiency of replacing citrate increasing as follows[248]:

SH/S^- > NH_2/NH_3^+ > =N-/=NH- > $COOH/COO^-$ > OH/O^-

This trend might be used for the assessment of the ligand substituting power providing the assessment of the covalent, electrostatic, or hydrogen bonding interactions with the negatively charged citrate molecules as summarized in **Table 8**.

Table 8. The Interactions classifications of the functional group adsorbed onto the citrate coated gold nanoparticles (Electrostatic : EO, Covalent: CO).

Functional groups	NH_2/ NH_3+	COOH /COO^-	SH/S^-	=N- /=NH-	OH/O^-
Types of interactions with AuNPs	EO [249], [250], [251]	EO [252], [253], [246]	CO [254], [255], [256], [257]	EO/CO [258], [259], [247]	EO [260], [261]
Raman shift observed	red/ blue	red	red	red	red/blue

6.7 Conclusion

Surface-enhanced Raman scattering (SERS) is a sensitive technique that reveals information regarding molecular adsorption driving forces at nanoparticle surfaces. While the plasmonic properties of SERS substrates provide the largest signal enhancements, chemical enhancement mechanisms are more sensitive to molecular adsorption and intermolecular interactions. Raman shift is the key parameter for the evaluation of the molecular adsorption onto the AuNF surface. We present the unified quantified approach for the relationship between the Raman shift of the adsorbed molecules and their interactions with the AuNF surface. we have developed the theoretical approach that links the theoretically calculated interactions energies of species with Au cluster, which transposes to the predictions of the Raman shift and the Raman shift variations with pH. As pH increases, and overcomes pKa, charge transfer becomes more favorable leading to the stronger interactions of molecules with the AuNF surface. In this paper, we also defined the interactions of molecules with AuNF surface, we have classified the covalent and electrostatic interactions, providing the model for the prediction of the interactions based on the molecular charge and the Raman shift.

Chapter 7. Summary, Significance, and Future Research Directions

7.1 Summary

Firstly, arsenic speciation was performed by the developed CRE-SERS method focusing on the commonly existing oxoarsenical species, including As^{III}, As^{V}, MMA^{V} and DMA^{V}. The CRE separation platform was the AgNF, which was fabricated by depositing silver nanoparticles colloidal solution onto glass substrate surface. Giving adsorption/desorption interactions between arsenicals and the AgNF surface, arsenical was separated during the species migration across the AgNF driven by the capillary flow resulting in the preconcentration of arsenicals right at the edge of the coffee ring stain. To further extend the traveled distances of oxoarsenicals, which would encourage the species separation, surfactants were then applied into the sessile droplet, enabling the reduction of the surface tension and leading to the solution permeation into the peripheral region of the drying sessile droplet. This peripheral region of the CRE was named as the halo coffee ring, because of two concentric-ring stain pattern formed after the complete sessile droplet evaporation. The separation of oxoarsenicals As^{III}, As^{V}, MMA^{V} and DMA^{V} using the halo CRE was successfully demonstrated in the buffer system with 0.1 M phosphate (pH=7.5). Then, scanning the CRE spot from the center to the edge of the droplet, SERS signals of oxoarsenicals were recorded at the normal CRE stain, following the scans at the halo region, demonstrating that arsenicals were separated along the halo region. This work provides a novel approach using the coffee ring effect for chemicals separation.

Secondly, a method based on surface-enhanced Raman spectroscopy (SERS) detection in combination with the CRE for separation was found to be particularly useful for analysis of unstable species, thanks to minimal sample pretreatment and unique fingerprint Ramon identification. Thus, the CRE-SERS was applied for the speciation of thioarsenicals: dimethylmonothioarsinic acid (DMMTA^{V}) and dimethyldithioarsinic acid (DMDTA^{V}), unstable yet important arsenic metabolites the analysis of which remains a challenging task. However, in the case of thioarsenicals, it was found that these labile species were oxidized onto the AgNF surface, forming the oxygen silver oxides. Thus, the more biocompatible and robust AuNF was fabricated and served as a the CRE substrate for the speciation of thiolated arsenicals. This CRE substrate was employed not only as a SERS substrate, but also as a platform for the separation of thioarsenicals. Once a drop of the thioarsenicals solution was placed onto the AuNF and evaporation of the solvent and the CRE stamp formation onto AuNF began, the SERS signal intensity substantially increased from center to edge regions of the evaporated droplet due to the presence of the CRE. Through calculating the pKa's of DMMTA^{V} and DMDTA^{V} and accordingly manipulating the chemical environment, separation of these thioarsenicals was achieved as they traveled different distances during the development of the coffee ring. The migration distances of individual species were influenced by a radial outward flow of a solute, the thioarsenicals-AuNF interactions and a thermally induced Marangoni flow. The AuNF based the coffee ring effect combined with SERS demonstrated a decent potential for the separation of arsenic species.

Thirdly, a unified theoretical approach based on the combination of oxoarsenicals and thioarsenicals speciation by the CRE-SERS has been developed for the analysis of small molecules. Three arsenic containing species, DMA^{V}, DMMTA^{V} and DMDTA^{V} were chosen as standards for the theory development. Three major factors affect the formation of the CRE deposit: the radial outward flow, the analyte-AuNF interactions and the reversed Marangoni flow, which is relatively weak in the aqueous solutions and, therefore, was neglected. I provided the mathematical description of the radial outward flow, followed by the introduction of the mass transfer equations for the arsenicals partition from the bulk to the nanofilm surface. The radial flow velocity was calculated through the CRE theory and the attraction forces between the AuNF and arsenicals were obtained from XDLVO. I then modified the van Deemter equation by introducing the radial flow as the mobile phase and the adsorption constants as mass transfer parameters to describe the CRE-driven nanochromatographic separation. I manipulated pH and the velocity of the radial flow to find optimal conditions for the separation of DMA^{V}, $DMMTA^{V}$, and $DMDTA^{V}$. The theoretical model enables a prediction of the travelled distances of small molecules during the formation of the CRE deposit through the different affinity of analytes to the AuNF. In case of the Raman peak overlap, selectively adjusting the pH allows tuning the Raman shift as the way to identify different species.

Fourthly, the developed theoretical approach and CRE-SERS method for small molecules was extrapolated for the separation of arsenic containing peptides: a novel arsenic-based anticancer Darinaparsin ($DMA^{III}GSH$, DAR) and its major breakdown product, dimethylarsino-cysteine ($DMA^{III}Cys$, DMAC). DAR was found to be effective against acute promyelocytic leukemia (APL) and exhibited less toxicity comparing to commonly used arsenic trioxide (ATO), and $DMA^{III}Cys$ was proposed to enter the cells and cause the therapeutic effect. Two major factors that affect the formation of the CRE deposit were the radial outward flow and analyte-AuNF interactions. In the final CRE deposit DAR was detected in the center and the middle regions, whereas DMAC traveled longer distances across the CRE stain and was in the middle and the edge regions. Despite the overlap of DAR and DMAC's Raman spectra, we were able to identify each compound due to their unique SERS fingerprint. Overall, the developed method was able not only to separate and identify the S-conjugated arsenicals, but at the same time to preserve the DAR and DMAC's As^{III} oxidations state and the fragile As – S moiety, thus providing an alternative speciation method for unstable thioarsenicals.

Fifthly, while the SERS sensitivity mostly rely on the plasmonic nanomaterials electromagnetic enhancements, chemical enhancement mechanisms that are more sensitive to molecular adsorption and intermolecular interactions were less exploited for the molecular detection. Raman shift variations are the key parameters for the evaluation of the molecular adsorption onto nanomaterial surface. Here I present the unified approach combining the Raman shift of the adsorbed molecules and the classification of their interactions with gold nanofilm (AuNF). I have employed three common arsenic species: DMA^{V}, $DMMTA^{V}$ and $DMDTA^{V}$ as a model for the theory development. By theoretically calculated interactions energies of species with Au cluster, we extrapolated this to the predictions of the the Raman shift variations with pH of the unknown arsenic species. Moreover, we have classified the interactions of the various molecules with the citrate coated gold nanoparticles. As pH increases, and overcomes pKa, charge transfer becomes more favorable leading to the stronger interactions of molecules with AuNF surface. Besides that, we defined the interactions of molecules with AuNF surface, classifying the covalent and electrostatic interactions, providing the model for the prediction of the interactions based on the molecular charge and the Raman shift.

7.2 Significance of this study

In the first part of this work, a novel arsenic speciation method using the CRE was developed. The CRE stain was formed by depositing 2 μL solution down onto the AgNF and the strong radial outward flow moved away everything in the droplet to the edge region. It was shown that the following two requirements would influence for CRE separation. Firstly, the liquid in the droplet should be able to travel into outer region of the drying droplet. Secondly, the arsenicals – AgNF surface interactions would govern the final CRE depositions. The introduction of surfactants was aimed to minimize the surface tension, so the droplet solution would be able to migrate into outer region by thanks to the reduction of surface tension and strong radial outward flow. Depositing the nanoparticles onto the glass surface would enhance the interaction between arsenicals and AgNF. The introduction of surfactants would be considered as a novel method, which decreases the surface tension enabling the liquid to travel into the peripheral region, due to the closely packed Ag nanoparticles on the AgNF. This radial outward flow moved away solutes in the sessile droplet, induced by the capillary action and decreased surface tension, oxoarsenicals were separated thanks to different affinity to the AgNF surface. This work ensures a unique and novel approach for the arsenic speciation by SERS, especially for a small volume of biological and environmental samples.

Secondly, the CRE-SERS was applied for the speciation of unstable thioarsenicals: dimethylmonothioarsinic acid ($DMMTA^V$) and dimethyldithioarsinic acid ($DMDTA^V$) onto AuNF surface providing an alternative method for the speciation of easily degradable compounds. This CRE substrate was employed not only as a SERS substrate, but also as a platform for the separation of thioarsenicals. Through calculating the pKa's of $DMMTA^V$ and $DMDTA^V$ and adjusting pH of buffer solution, the migration distances of analytes across the AuNF surface were controlled and the species of interest were guided to the specific locations in the CRE stain. The migration distances of individual species were influenced by a radial outward flow of a solute, the thioarsenicals-AuNF interactions and a thermally induced Marangoni flow. The AuNF based the coffee ring effect combined with SERS demonstrated a decent potential for the separation of unstable arsenic species.

Thirdly, I developed a theoretical framework for the CRE-driven nanochromatography on AuNF in SERS analysis of small molecules, taking arsenicals as an example. To do so, I adapted the classic chromatographic theory to derive a modified van Deemter equation for the CRE-driven separation by combining the CRE theory for the radial flow and the XDLVO theory for mass transfer between solution and AuNF surface. To my best knowledge, this is the first theoretical description for CRE-driven separation, which I believe is a major breakthrough in the field of CRE-driven nanochromatography. The applications of CRE on nanofilm and nanoparticle surface, in particular coupled to SERS, have been increasingly expanded from particles and macromolecules to small molecules. This new type of CRE-driven separation technique appears to be promising as a powerful nanochromatography for analysis of a broad range of compounds. Despite the theory behind the formation of CRE itself from a single drop evaporation onto the dry surface is well established, theoretical approaches for CRE-driven separation, especially the analyte-nanofilm surface interactions involving small molecules, have been lacking. By developing and using this theoretical model, I was able to predict the travel distances of arsenicals based on their different affinity to the AuNF and to manipulate pH and the radial flow velocity to achieve optimal separations. The successful adaptation of classic chromatographic theory to CRE-driven nanochromatography provides the ability of predicting the travel distances of small molecules during the CRE formation and guiding molecules to certain specific locations of the CRE stain through manipulating conditions (e.g., pH), which is essential for expanding the CRE applications to unknown analytes.

Fourthly, the CRE-SERS previously developed theoretical approach for the small molecule's speciation was extrapolated for the separation of arsenic containing peptides: a novel arsenic-based anticancer Darinaparsin ($DMA^{III}GSH$, DAR) and its major breakdown product, dimethylarsino-cysteine ($DMA^{III}Cys$, DMAC). DAR was found to be effective against acute promyelocytic leukemia (APL) and exhibited less toxicity comparing to commonly used arsenic trioxide (ATO). The significance of the work lies in the following: the CRE-SERS method was able not only to separate, but also and identify the S-conjugated peptides resulting in the successful application of chromatographical framework for the speciation unstable S-conjugated peptides. In addition, the CRE-SERS enabled the preservation of the native forms of DAR and DMAC's molecules demonstrating the detection of the As^{III} oxidations states onto the AuNF surface and the identification of the fragile As – S moiety, thus providing an key insights into the active binding domain of the APL targeting drugs.

Fifthly, the citrate coated gold nanoparticles are the mostly employed nanomaterial for the development of the nano-based sensors. Raman shift appears to be the key parameter for the evaluation of the molecular adsorption onto nanomaterial surface. In this work I have developed the unified theoretical approach utilizing the pH dependent Raman shift variations of the adsorbed molecules onto the AuNF surface. It is crucial to classify the interactions of the various molecules with the citrate coated gold nanoparticles by this experimental framework instead of utilizing the time-consuming quantum chemistry approaches. Besides that, we provided the model for the prediction of the interactions energeias based on the molecular charge and the Raman shift variations.

7.2.1. Limitations of the CRE-SERS

Firstly, the major limitation of the CRE-SERS method lies in the inherently poor reproducibility of the SERS spectra. The great care must be taken during the nanofilms fabrication as nanoparticles distribution onto a nanofilm surface plays a crucial role in the overall reproducibility of SERS spectra. It is vital to apply the robust chemical vapor deposition techniques or similar approaches that produce high quality substrates for SERS diagnostics due to the controlled nanoparticles deposition leading to the homogeneous distribution of hot spots across the nanofilm surface, and thus increasing reproducibility of a SERS output signal. In addition, the homogeneous nanoparticles distribution will improve the separation capacity of nanofilms through a decrease of the Eddy diffusion coefficient (van Deemter equation) resulting in the increase in the overall method resolution capacity.

Secondly, the mobile phase for CRE-SERS separations should not contain organic solvent but 100% water solution because the introduction of the organic phase would decrease the surface tension of the lying droplet leading to the reversed Marangoni flow, which might worsen the separation of analytes. Besides, the effect of the Marangoni flow must be described and properly validated in the modified van Deemter equation, which would make it even more difficult to control and predict the final travelled distances of the individual analytes. Thus, the implementation of the gradient elution should be avoided during the preparation of the mobile phase.

Thirdly, the CRE regions are subject to discussion and the unified metric must be developed to verify the borders of each region of the CRE. In addition, the center, middle and edge regions must be validated by the complementary techniques like SIMS or LA-ICP-MS following the identification of the confidence intervals for each region.

7.3 Future research directions

Firstly, the oxoarsenicals speciation using the CRE could be expanded the application to other arsenic species, especially for the halo coffee ring effect. For now, some additional investigations about the halo CRE mechanism might be applied for the comprehensive understanding of the CRE phenomenon and further bioanalytical applications. For example, the influence of the AgNF surface charges upon the travelled distances of the species across the edge and outer regions of the CRE needs to be studied.

Also, it should be promising to investigate the influence of the surfactants onto the uniformity of the CRE stain in the assigned regions.

Secondly, the arsenic speciation using the CRE could be expanded to the speciation of the arsenic bonded proteins by the SERS approaches. As peptides speciation was successfully carried out by tuning the solvent evaporation speed and pH environment, the potential application of the developed method for the speciation of macromolecules appears promising, especially giving the clear control of the travelled distances of the target analytes.

Thirdly, the halo coffee ring has a significant potential for the application in the separation science and the van Deemter equation for the CRE might be further modified to adapt the influence of the Marangoni flow that is generated by the addition of surfactants. That will shed light onto the further separation optimizations when the extension of the standard CRE is needed.

Fourthly, the CRE promotes the partial separation of the complex mixture of the biological species that is especially useful for metabolomics bioanalytical sensing. Indeed, the cell lysates can be directly analyzed using the CRE substrate following the nondestructive MALDI sensing to analyze the fragile compounds onto the nanofilm surface without the sample preparation and protein purification. Overall, the CRE-driven direct sensing detection processes play a crucial role in the acceleration of the analytical sensing and preservation of the fragile biological compounds.

Fifthly, the ultimate objective of the presented study was to finally apply the developed CRE-SERS method for the direct sensing of small molecules in the complex biological matrices. We know that we can apply the CRE-SERS for the peptide's separation (**Chapter 6**), and even though some overlap of the DAR and DMAC SERS spectra was present in the middle region, I was able to identify each arsenical by SERS thanks to their unique vibrational fingerprints (**Figure 22**). To further extrapolate the developed method for the speciation of the arsenic conjugated proteins, I have applied the CRE-SERS method for the arsenical speciation in sheep red blood cell lysates aiming to identify DMA^V in the biological macromolecules. In short, the sheep cell lines were cultured at a concentration of 2×10^7 cells/ml, centrifuged at 3000 rpm for 10 minutes, washed with PBS twice, spun down again, and then stored at −30°C for future usage. Once the cell lysates were prepared by the sonication (15 min), 20 µl of the cell lysates were mixed with 5 µl of 1000 ppm individual DMA^V standard solution and then 400 µl of PBS buffer were added (pH=7). After the deposition of the freshly prepared mixture of cell lysates and DMA^V onto the AuNF and solvent evaporation, I have scanned the nanofilm surface from the center to the edge and obtained the SERS output signal. Along with that I employed the pure (1000 ppm) DMA^V PBS buffer solution (pH = 7) as a control metric standard and tracked DMA^V's SERS signal on the same AuNF. The traveled distance of the DMA^V was not significantly different from the reported previously at pH= 7 (**Table 4**). In the resulting CRE deposit, I have found that DMA^V traveled a shorter distance and was detected in the center and middle regions while the cell lysates were driven down to the edge and situated mainly at the edge region. The DMA^V SERS signal was detected despite the formation of a protein's corona onto the AuNF surface that commonly hindered the nanofilm electromagnetic enhancements due to the "deactivation" of AuNPs hot spots (data not shown).

To validate the CRE-SERS method, I have opted for TOF-SIMS, which allows tracking the mass spectrometry signal onto a flat surface enabling the sensing across the CRE regions. The CRE-TOF-SIMS of DMA^V (137 - 1) obtained in the negative selection mode demonstrated the same distribution pattern of DMA^V across the dried CRE deposit as CRE-SERS. Overall, I have successfully identified the DMA^V in the cell lysates thanks to its distinct traveled distance proving that the identification of the arsenic species in a complex biological sample is possible, however, the CRE ring stains for the detection of small molecules require further validation and systematization.

References

1. Deegan, R.D., et al., *Capillary flow as the cause of ring stains from dried liquid drops.* Nature, 1997. **389**(6653): p. 827-829.

2. Soltman, D. and V. Subramanian, *Inkjet-printed line morphologies and temperature control of the coffee ring effect.* Langmuir, 2008. **24**(5): p. 2224-2231.

3. Parsa, M., et al., *Effect of substrate temperature on pattern formation of nanoparticles from volatile drops.* Langmuir, 2015. **31**(11): p. 3354-3367.

4. Choi, S., et al., *Coffee-ring effect-based three dimensional patterning of micro/nanoparticle assembly with a single droplet.* Langmuir, 2010. **26**(14): p. 11690-11698.

5. Nguyen, T.A., M.A. Hampton, and A.V. Nguyen, *Evaporation of nanoparticle droplets on smooth hydrophobic surfaces: the inner coffee ring deposits.* The Journal of Physical Chemistry C, 2013. **117**(9): p. 4707-4716.

6. Ruan, S., X. Li, and T. Jiang, *Hydrophilic-hydrophobic poly (dimethyl siloxane)-based SERS substrate with internal Raman signaling.* Materials Chemistry and Physics, 2020. **255**: p. 123582.

7. Anyfantakis, M. and D. Baigl, *Manipulating the coffee-ring effect: interactions at work.* ChemPhysChem, 2015. **16**(13): p. 2726-2734.

8. Yunker, P.J., et al., *Suppression of the coffee-ring effect by shape-dependent capillary interactions.* Nature, 2011. **476**(7360): p. 308-311.

9. Deegan, R.D., et al., *Contact line deposits in an evaporating drop.* Physical Review E, 2000. **62**(1): p. 756.

10. Fischer, B.J., *Particle convection in an evaporating colloidal droplet.* Langmuir, 2002. **18**(1): p. 60-67.

11. Truskett, V.N. and K.J. Stebe, *Influence of surfactants on an evaporating drop: Fluorescence images and particle deposition patterns.* Langmuir, 2003. **19**(20): p. 8271-8279.

12. Dunn, G., et al., *A mathematical model for the evaporation of a thin sessile liquid droplet: Comparison between experiment and theory.* Colloids and Surfaces A: Physicochemical and Engineering Aspects, 2008. **323**(1-3): p. 50-55.

13. Birdi, K., D. Vu, and A. Winter, *A study of the evaporation rates of small water drops placed on a solid surface.* The Journal of Physical Chemistry, 1989. **93**(9): p. 3702-3703.

14. Hu, H. and R.G. Larson, *Evaporation of a sessile droplet on a substrate.* The Journal of Physical Chemistry B, 2002. **106**(6): p. 1334-1344.

15. Larson, R.G., *Transport and deposition patterns in drying sessile droplets.* AIChE Journal, 2014. **60**(5): p. 1538-1571.

16. Corkidi, G., et al., *Evaporation dynamics and sedimentation pattern of a sessile particle laden water droplet.* Experiments in Fluids, 2016. **57**(6): p. 99.

17. Bhardwaj, R., et al., *Self-assembly of colloidal particles from evaporating droplets: role of DLVO interactions and proposition of a phase diagram.* Langmuir, 2010. **26**(11): p. 7833-7842.

18. Marsico, A.L., et al., *Enhanced laser desorption/ionization mass spectrometric detection of biomolecules using gold nanoparticles, matrix, and the coffee ring effect.* Analytical Chemistry, 2017. **89**(5): p. 3009-3014.

19. Juneja, S. and J. Bhattacharya, *Coffee ring effect assisted improved S. aureus screening on a physically restrained gold nanoflower enriched SERS substrate.* Colloids and Surfaces B: Biointerfaces, 2019. **182**: p. 110349.

20. Ji, B., et al., *Suppression of coffee-ring effect via periodic oscillation of substrate for ultra-sensitive enrichment towards surface-enhanced Raman scattering.* Nanoscale, 2019. **11**(43): p. 20534-20545.

21. Hu, J.-B., Y.-C. Chen, and P.L. Urban, *Coffee-ring effects in laser desorption/ionization mass spectrometry.* Analytica Chimica Acta, 2013. **766**: p. 77-82.

22. Stöckle, R.M., et al., *Nanoscale chemical analysis by tip-enhanced Raman spectroscopy.* Chemical Physics Letters, 2000. **318**(1): p. 131-136.

23. Gracie, K., et al., *Simultaneous detection and quantification of three bacterial meningitis pathogens by SERS.* Chemical Science, 2014. **5**(3): p. 1030-1040.

24. Blackie, E.J., E.C.L. Ru, and P.G. Etchegoin, *Single-molecule surface-enhanced Raman spectroscopy of nonresonant molecules.* Journal of the American Chemical Society, 2009. **131**(40): p. 14466-14472.

25. Le Ru, E., et al., *Surface enhanced Raman scattering enhancement factors: a comprehensive study*. The Journal of Physical Chemistry C, 2007. **111**(37): p. 13794-13803.

26. Valley, N., et al., *A look at the origin and magnitude of the chemical contribution to the enhancement mechanism of surface-enhanced Raman spectroscopy (SERS): Theory and experiment.* The Journal of Physical Chemistry Letters, 2013. **4**(16): p. 2599-2604.

27. McNay, G., et al., *Surface-enhanced Raman scattering (SERS) and surface-enhanced resonance Raman scattering (SERRS): a review of applications.* Applied Spectroscopy, 2011. **65**(8): p. 825-837.

28. Prochazka, M., *SERS Investigations of Cells, Viruses and Microorganisms*, in *Surface-Enhanced Raman Spectroscopy*. 2016, Springer. p. 127-148.

29. Kneipp, K., et al., *Surface-enhanced Raman spectroscopy in single living cells using gold nanoparticles.* Applied Spectroscopy, 2002. **56**(2): p. 150-154.

30. Boca, S., et al., *Flower-shaped gold nanoparticles: synthesis, characterization and their application as SERS-active tags inside living cells.* Nanotechnology, 2010. **22**(5): p. 055702.

31. Nabiev, I., H. Morjani, and M. Manfait, *Selective analysis of antitumor drug interaction with living cancer cells as probed by surface-enhanced Raman spectroscopy.* European Biophysics Journal, 1991. **19**(6): p. 311-316.

32. Feng, S., et al., *Ultrasound-mediated method for rapid delivery of nano-particles into cells for intracellular surface-enhanced Raman spectroscopy and cancer cell screening.* Nanotechnology, 2015. **26**(6): p. 065101.

33. Usman, M., et al., *Facile silicone oil-coated hydrophobic surface for surface enhanced Raman spectroscopy of antibiotics.* RSC Advances, 2019. **9**(25): p. 14109-14115.

34. Minh, D.T.C., et al., *Detection of sildenafil adulterated in herbal products using thin layer chromatography combined with surface enhanced Raman spectroscopy:"Double coffee-ring effect" based enhancement.* Journal of Pharmaceutical and Biomedical Analysis, 2019. **174**: p. 340-347.

35. Hong, Y., et al., *Label-free diagnosis for colorectal cancer through coffee ring-assisted surface-enhanced Raman spectroscopy on blood serum.* Journal of Biophotonics, 2020. **13**(4): p. e201960176.

36. Zhang, L., et al., *Combined host-guest complex with coffee-ring effect for constructing ultrasensitive SERS substrate for phenformin hydrochloride detection in healthcare products.* Analytical and Bioanalytical Chemistry, 2018. **410**(29): p. 7599-7609.

37. Xu, J., et al., *Facile detection of polycyclic aromatic hydrocarbons by a surface-enhanced Raman scattering sensor based on the Au coffee ring effect.* ACS Applied Materials & Interfaces, 2014. **6**(9): p. 6891-6897.

38. Murugesan, B. and J. Yang, *Tunable Coffee Ring Formation on Polycarbonate Nanofiber Film for Sensitive SERS Detection of Phenylalanine in Urine.* ACS Omega, 2019. **4**(12): p. 14928-14936.

39. Hwang, J., S. Lee, and J. Choo, *Application of a SERS-based lateral flow immunoassay strip for the rapid and sensitive detection of staphylococcal enterotoxin B.* Nanoscale, 2016. **8**(22): p. 11418-11425.

40. Wang, Q.Q., D.J. Thomas, and H. Naranmandura, *Importance of being thiomethylated: formation, fate, and effects of methylated thioarsenicals.* Chemical Research in Toxicology, 2015. **28**(3): p. 281-289.

41. Kim, S., et al., *A rapid tag-free identification of Escherichia coli antibiotic-resistant isolates using Raman scattering.* Analytical Methods, 2019. **11**(42): p. 5381-5387.

42. Liu, Y., et al., *Micro-coffee-ring-patterned fiber SERS probes and their in situ detection application in complex liquid environments.* Sensors and Actuators B: Chemical, 2019. **299**: p. 126990.

43. Hussain, A., D.-W. Sun, and H. Pu, *SERS detection of urea and ammonium sulfate adulterants in milk with coffee ring effect.* Food Additives & Contaminants: Part A, 2019. **36**(6): p. 851-862.

44. Wróbel, M.S., et al. *Drop-coating deposition surface-enhanced Raman spectroscopy on silver substrates for biofluid analysis*. in *European Conference on Biomedical Optics*. 2019. Optical Society of America.

45. Chen, Y., et al., *Study on surface enhancement fluorescence effect of gold nanoparticle assembly structure on rough copper substrate surface.* Optik, 2018. **158**: p. 901-907.

46. Gholami, M., et al., *Application of reverse osmosis technology for arsenic removal from drinking water.* Desalination, 2006. **200**(1-3): p. 725-727.

47. Uddin, R. and N.H. Huda, *Arsenic poisoning in Bangladesh.* Oman Medical Journal, 2011. **26**(3): p. 207.

48. Borak, J. and H.D. Hosgood, *Seafood arsenic: implications for human risk assessment.* Regulatory Toxicology and Pharmacology, 2007. **47**(2): p. 204-212.

49. Wauchope, R., *Fixation of arsenical herbicides, phosphate, and arsenate in alluvial soils.* Journal of Environmental Quality, 1975. **4**(3): p. 355-358.

50. Frankenberger Jr, W.T., *Environmental chemistry of arsenic*. 2001: CRC Press.

51. Antman, K.H., *Introduction: the history of arsenic trioxide in cancer therapy.* The Oncologist, 2001. **6**(Supplement 2): p. 1-2.

52. Quintás-Cardama, A., et al., *Chemical and clinical development of darinaparsin, a novel organic arsenic derivative.* Anti-Cancer Agents in Medicinal Chemistry (Formerly Current Medicinal Chemistry-Anti-Cancer Agents), 2008. **8**(8): p. 904-909.

53. Kubachka, K.M., et al., *Exploring the in vitro formation of trimethylarsine sulfide from dimethylthioarsinic acid in anaerobic microflora of mouse cecum using HPLC–ICP-MS and HPLC–ESI-MS.* Toxicology and Applied Pharmacology, 2009. **239**(2): p. 137-143.

54. Alava, P., et al., *HPLC-ICP-MS method development to monitor arsenic speciation changes by human gut microbiota.* Biomedical Chromatography, 2012. **26**(4): p. 524-533.

55. Mandal, B.K., et al., *A SEC-HPLC-ICP MS hyphenated technique for identification of sulfur-containing arsenic metabolites in biological samples.* Journal of Chromatography B, 2008. **874**(1-2): p. 64-76.

56. Hayakawa, T., et al., *A new metabolic pathway of arsenite: arsenic–glutathione complexes are substrates for human arsenic methyltransferase Cyt19.* Archives of Toxicology, 2005. **79**(4): p. 183-191.

57. Hansen, H.R., et al., *2-Dimethylarsinothioyl Acetic Acid Identified in a Biological Sample: The First Occurrence of a Mammalian Arsinothioyl Metabolite.* Angewandte Chemie, 2004. **116**(3): p. 341-344.

58. Raab, A., et al., *Pentavalent arsenic can bind to biomolecules.* Angewandte Chemie International Edition, 2007. **46**(15): p. 2594-2597.

59. Naranmandura, H., K. Ibata, and K.T. Suzuki, *Toxicity of dimethylmonothioarsinic acid toward human epidermoid carcinoma A431 cells.* Chemical Research in Toxicology, 2007. **20**(8): p. 1120-1125.

60. Ashoka, S., et al., *Comparison of digestion methods for ICP-MS determination of trace elements in fish tissues.* Analytica Chimica Acta, 2009. **653**(2): p. 191-9.

61. Yehiayan, L., et al., *Extraction tool and matrix effects on arsenic speciation analysis in cell lines.* Analytica Chimica Acta, 2011. **699**(2): p. 187-192.

62. Dheeman, D.S., et al., *Pathway of human AS3MT arsenic methylation.* Chemical Research in Toxicology, 2014. **27**(11): p. 1979-1989.

63. Chen, B., et al., *Arsenic speciation in the blood of arsenite-treated F344 rats.* Chemical Research in Toxicology, 2013. **26**(6): p. 952-962.

64. Yehiayan, L., et al., *Speciation, formation, stability and analytical challenges of human arsenic metabolites.* Journal of Analytical Atomic Spectrometry, 2009. **24**(10): p. 1397-1405.

65. Dheeman, D.S., et al., *Pathway of human AS3MT arsenic methylation.* Chemical Research in Toxicology, 2014. **27**(11): p. 1979-1989.

66. Baker-Austin, C., et al., *Extreme arsenic resistance by the acidophilic archaeon 'Ferroplasma acidarmanus' Fer1.* Extremophiles, 2007. **11**(3): p. 425-434.

67. Chen, J., et al., *Volatilization of arsenic from polluted soil by Pseudomonas putida engineered for expression of the arsM arsenic (III) S-adenosine methyltransferase gene.* Environmental Science & Technology, 2014. **48**(17): p. 10337-10344.

68. Hamdi, M., et al., *Arsenic transport by zebrafish aquaglyceroporins.* BMC Molecular Biology, 2009. **10**(1): p. 1-11.

69. Dufailly, V., et al., *Validation of a method for arsenic speciation in food by ion chromatography-inductively coupled plasma/mass spectrometry after ultrasonic-assisted enzymatic extraction.* Journal of AOAC International, 2011. **94**(3): p. 947-958.

70. Ammann, A.A., *Arsenic speciation by gradient anion exchange narrow bore ion chromatography and high resolution inductively coupled plasma mass spectrometry detection.* Journal of Chromatography A, 2010. **1217**(14): p. 2111-2116.

71. Yang, G., et al., *Speciation analysis of arsenic in Mya arenaria Linnaeus and Shrimp with capillary electrophoresis-inductively coupled plasma mass spectrometry*. Talanta, 2009. **78**(2): p. 471-476.

72. Yang, G.-D., et al., *Speciation Analysis of Arsenic in Seafood with Capillary Electrophoresis-UV Detection.* Chinese Journal of Analytical Chemistry, 2009. **37**(4): p. 532-536.

73. Kozak, L., P. Niedzielski, and W. Szczuciński, *The methodology and results of determination of inorganic arsenic species in mobile fractions of tsunami deposits by a hyphenated technique of HPLC-HG-AAS.* International Journal of Environmental and Analytical Chemistry, 2008. **88**(14): p. 989-1003.

74. Gong, Z., et al., *Unstable trivalent arsenic metabolites, monomethylarsonous acid and dimethylarsinous acid.* Journal of Analytical Atomic Spectrometry, 2001. **16**(12): p. 1409-1413.

75. Kobayashi, Y., X. Cui, and S. Hirano, *Stability of arsenic metabolites, arsenic triglutathione [As(GS)(3)] and methylarsenic diglutathione [CH3As(GS)(2)], in rat bile.* Toxicology, 2005. **211**(1-2): p. 115-123.

76. Conklin, S.D., et al., *Investigation of the pH effects on the formation of methylated thio-arsenicals, and the effects of pH and temperature on their stability.* Journal of Analytical Atomic Spectrometry, 2008. **23**(5): p. 711-716.

77. Greaves, S.J. and W.P. Griffith, *Surface-enhanced Raman scattering (SERS) from silver colloids of vanadate, phosphate and arsenate.* Journal of Raman Spectroscopy, 1988. **19**(8): p. 503-507.

78. Du, J., J. Cui, and C. Jing, *Rapid in situ identification of arsenic species using a portable Fe3O4@Ag SERS sensor.* Chemical Communications, 2014. **50**(3): p. 347-349.

79. Song, L., et al., *A novel biosensor based on Au@Ag core–shell nanoparticles for SERS detection of arsenic (III).* Talanta, 2016. **146**: p. 285-290.

80. Xu, Z., et al., *Surface-enhanced Raman spectroscopy of arsenate and arsenite using Ag nanofilm prepared by modified mirror reaction.* Journal of Colloid and Interface Science, 2010. **347**(1): p. 90-95.

81. Gloria, D., G. Moran, and D.B. Hibbert. *Detection of Arsenobetaine: A Step Towards SERS-based Arsenic Speciation*. in *XXII International Conference on Raman Spectroscop*. 2010. Boston, MA, USA: American Inst. of Physics.

82. Olavarría-Fullerton, J., et al., *Surface-Enhanced Raman Scattering (SERS) Characterization of Trace Organoarsenic Antimicrobials Using Silver/Polydimethylsiloxane Nanocomposites.* Applied Spectroscopy, 2011. **65**(4): p. 423-428.

83. Hao, J.M., et al., *Fabrication and evolution of multilayer silver nanofilms for surface-enhanced Raman scattering sensing of arsenate.* Nanoscale Research Letters, 2011. **6**: p. 263.

84. Xu, Z., et al., *Effect of bonding interactions between arsenate and silver nanofilm on surface-enhanced Raman scattering sensitivity.* The Journal of Physical Chemistry C, 2011. **116**(1): p. 325-329.

85. Xu, Z., et al., *Effects and mechanisms of water matrix on surface-enhanced Raman scattering analysis of arsenite on silver nanofilm.* Colloids and Surfaces A: Physicochemical and Engineering Aspects, 2016. **497**: p. 117-125.

86. Li, J., et al., *Highly sensitive SERS detection of As3+ ions in aqueous media using glutathione functionalized silver nanoparticles.* ACS Applied Materials & Interfaces, 2011. **3**(10): p. 3936-3941.

87. Ye, L., et al., *A simple label-free rhodamine 6G SERS probe for quantitative analysis of trace As3+ in an aptamer–nanosol.* RSC Advances, 2014. **4**(62): p. 32960-32964.

88. Hao, J., et al., *SERS detection of arsenic in water: A review.* Journal of Environmental Sciences, 2015. **36**: p. 152-162.

89. Mulvihill, M., et al., *Surface-Enhanced Raman Spectroscopy for Trace Arsenic Detection in Contaminated Water.* Angewandte Chemie International Edition, 2008. **47**(34): p. 6456-6460.

90. Yang, M., et al., *Potential application of SERS for arsenic speciation in biological matrices.* Analytical and Bioanalytical Chemistry, 2017. **409**(20): p. 4683-4695.

91. Kočišová, E., M. Procházka, and H. Šípová, *Thiol-modified gold-coated glass as an efficient hydrophobic substrate for drop coating deposition Raman (DCDR) technique.* Journal of Raman Spectroscopy, 2016. **47**(11): p. 1394-1396.

92. Wang, W., et al., *Coffee-ring effect-based simultaneous SERS substrate fabrication and analyte enrichment for trace analysis.* Nanoscale, 2014. **6**(16): p. 9588-9593.

93. Wong, T.S., et al., *Nanochromatography Driven by the Coffee Ring Effect.* Analytical Chemistry, 2011. **83**(6): p. 1871-1873.

94. Devlin, N.R., K. Loehr, and M.T. Harris, *The separation of two different sized particles in an evaporating droplet.* Aiche Journal, 2015. **61**(10): p. 3547-3556.

95. Li, D., et al., *Facile On-Site Detection of Substituted Aromatic Pollutants in Water Using Thin Layer Chromatography Combined with Surface-Enhanced Raman Spectroscopy.* Environmental Science & Technology, 2011. **45**(9): p. 4046-4052.

96. Zhu, Q., et al., *Antipsychotic drug poisoning monitoring of clozapine in urine by using coffee ring effect based surface-enhanced Raman spectroscopy.* Analytica Chimica Acta, 2018. **1014**: p. 64-70.

97. Zhu, Q., et al., *Rapid on-site TLC–SERS detection of four antidiabetes drugs used as adulterants in botanical dietary supplements.* Analytical and Bioanalytical Chemistry, 2014. **406**(7): p. 1877-1884.

98. Ho, Y.C., W.W.Y. Lee, and S.E.J. Bell, *Investigation of the chemical origin and evidential value of differences in the SERS spectra of blue gel inks.* Analyst, 2016. **141**(17): p. 5152-5158.

99. Brochard-Wyart, F., R. Fondecave, and M. Boudoussier, *Wetting of antagonist mixtures: the `leak out' transition.* International Journal of Engineering Science, 2000. **38**(9–10): p. 1033-1047.

100. Fondecave, R. and F.B. Wyart, *Wetting laws for polymer solutions.* Europhysics Letters, 1997. **37**(2): p. 115-120.

101. Maher, W.A., et al., *Thio arsenic species measurements in marine organisms and geothermal waters.* Microchemical Journal, 2013. **111**: p. 82-90.

102. Lee, P. and D. Meisel, *Adsorption and surface-enhanced Raman of dyes on silver and gold sols.* The Journal of Physical Chemistry, 1982. **86**(17): p. 3391-3395.

103. Grabar, K.C., et al., *Preparation and Characterization of Au Colloid Monolayers.* Analytical Chemistry, 1995. **67**(4): p. 735-743.

104. Bharathi, S., N. Fishelson, and O. Lev, *Direct Synthesis and Characterization of Gold and Other Noble Metal Nanodispersions in Sol−Gel-Derived Organically Modified Silicates.* Langmuir, 1999. **15**(6): p. 1929-1937.

105. Aslan, K., P. Holley, and C.D. Geddes, *Metal-enhanced fluorescence from silver nanoparticle-deposited polycarbonate substrates.* Journal of Materials Chemistry, 2006. **16**(27): p. 2846-2852.

106. Loehr, T.M. and R.A. Plane, *Raman spectra and structures of arsenious acid and arsenites in aqueous solution.* Inorganic Chemistry, 1968. **7**(9): p. 1708-1714.

107. Vansant, F.K., B.J. Van Der Veken, and H.O. Desseyn, *Vibrational analysis of arsenic acid and its anions: I. Description of the Raman spectra.* Journal of Molecular Structure, 1973. **15**(3): p. 425-437.

108. Vansant, F., B. Van der Veken, and M. Herman, *The vibrational analysis of methylarsonic acid, trideuteromethylarsonic acid and their anions.* Journal of Molecular Structure, 1976. **35**(2): p. 191-200.

109. Stýblo, M., et al., *Identification of methylated metabolites of inorganic arsenic by thin-layer chromatography.* Journal of Chromatography B, 1995. **668**(1): p. 21-29.

110. Huang, Y.-F., et al., *Activation of Oxygen on Gold and Silver Nanoparticles Assisted by Surface Plasmon Resonances.* Angewandte Chemie International Edition, 2014. **53**(9): p. 2353-2357.

111. Council, N.R., *Arsenic in Drinking Water*. 1999, Washington, DC: The National Academies Press. 330.

112. Still, T., P.J. Yunker, and A.G. Yodh, *Surfactant-induced Marangoni eddies alter the coffee-rings of evaporating colloidal drops.* Langmuir, 2012. **28**(11): p. 4984-4988.

113. Dan, X., M. Jürgen, and W. Rainer, *Retention of arsenic species on zwitterionic stationary phase in hydrophilic interaction chromatography.* Journal of Separation Science, 2010. **33**(6-7): p. 817-825.

114. Fan, C., et al., *Thiolation in arsenic metabolism: a chemical perspective.* Metallomics, 2018.

115. Rehman, K. and H. Naranmandura, *Arsenic metabolism and thioarsenicals.* Metallomics, 2012. **4**(9): p. 881-892.

116. Yehiayan, L., et al., *Dimethylarsinothioyl glutathione as a metabolite in human multiple myeloma cell lines upon exposure to darinaparsin.* Chemical Research in Toxicology, 2014. **27**(5): p. 754-764.

117. Chen, J. and B.P. Rosen, *Organoarsenical biotransformations by Shewanella putrefaciens.* Environmental Science & Technology, 2016. **50**(15): p. 7956-7963.

118. Raml, R., et al., *Thio-dimethylarsinate is a common metabolite in urine samples from arsenic-exposed women in Bangladesh.* Toxicology and Applied Pharmacology, 2007. **222**(3): p. 374-380.

119. Rosen, B.P., *Biochemistry of arsenic detoxification.* FEBS Letters, 2002. **529**(1): p. 86-92.

120. Zhu, Y.-G., et al., *Earth abides arsenic biotransformations.* Annual Review of Earth and Planetary Sciences, 2014. **42**: p. 443-467.

121. Rosen, B.P., *Families of arsenic transporters.* Trends in Microbiology, 1999. **7**(5): p. 207-212.

122. Rosen, B.P. and Z. Liu, *Transport pathways for arsenic and selenium: a minireview.* Environment International, 2009. **35**(3): p. 512-515.

123. Naranmandura, H. and K.T. Suzuki, *Formation of dimethylthioarsenicals in red blood cells.* Toxicology and Applied Pharmacology, 2008. **227**(3): p. 390-399.

124. Fan, C., et al., *Thiolation in arsenic metabolism: a chemical perspective.* Metallomics, 2018. **10**(10): p. 1368-1382.

125. Jung, J.-Y., Y.W. Kim, and J.Y. Yoo, *Behavior of particles in an evaporating didisperse colloid droplet on a hydrophilic surface.* Analytical Chemistry, 2009. **81**(19): p. 8256-8259.

126. Wong, T.-S., et al., *Nanochromatography driven by the coffee ring effect.* Analytical Chemistry, 2011. **83**(6): p. 1871-1873.

127. Miller, J.B., et al., *Phase separation and the 'coffee-ring'effect in polymer–nanocrystal mixtures.* Soft Matter, 2014. **10**(11): p. 1665-1675.

128. Yang, M., et al., *Arsenic speciation on silver nanofilms by surface-enhanced raman spectroscopy.* Analytical Chemistry, 2019. **91**(13): p. 8280-8288.

129. Yang, M., et al., *Raman spectra of thiolated arsenicals with biological importance.* Talanta, 2018. **179**: p. 520-530.

130. Cullen, W.R., et al., *Methylated and thiolated arsenic species for environmental and health research—a review on synthesis and characterization.* Journal of Environmental Sciences, 2016. **49**: p. 7-27.

131. Suzuki, K.T., et al., *Dimethylthioarsenicals as arsenic metabolites and their chemical preparations.* Chemical Research in Toxicology, 2004. **17**(7): p. 914-921.

132. Fricke, M.W., et al., *Chromatographic separation and identification of products from the reaction of dimethylarsinic acid with hydrogen sulfide.* Chemical Research in Toxicology, 2005. **18**(12): p. 1821-1829.

133. Schaftenaar, G. and J.H. Noordik, *Molden: a pre-and post-processing program for molecular and electronic structures.* Journal of Computer-aided Molecular Design, 2000. **14**(2): p. 123-134.

134. Lu, T. and F. Chen, *Multiwfn: a multifunctional wavefunction analyzer.* Journal of Computational Chemistry, 2012. **33**(5): p. 580-592.

135. Vansant, F., B. Van der Veken, and M. Herman, *Vibrational analysis of dimethylarsinic acid.* Spectrochimica Acta Part A: Molecular Spectroscopy, 1974. **30**(1): p. 69-78.

136. Watanabe, T. and S. Hirano, *Metabolism of arsenic and its toxicological relevance.* Archives of Toxicology, 2013. **87**(6): p. 969-979.

137. Santos, T.d.A.D.d., et al., *Potentiometric and conductimetric studies of chemical equilibria for pyridoxine hydrochloride in aqueous solutions: simple experimental determination of pKa values and analytical applications to pharmaceutical analysis.* Eclética Química, 2010. **35**(4): p. 81-86.

138. Dogan Daldal, Y., et al., *Liquid Chromatographic, Spectrophotometric and Potentiometric pKa Determination of Ranitidine and Famotidine.* Current Drug Therapy, 2014. **9**(4): p. 277-284.

139. Ferrando-Climent, L., et al., *Comprehensive study of ibuprofen and its metabolites in activated sludge batch experiments and aquatic environment.* Science of the Total Environment, 2012. **438**: p. 404-413.

140. Svintsitskaya, N., et al., *A new procedure for synthesis of phosphorylated ynamines.* Russian Journal of General Chemistry, 2008. **78**(1): p. 157-159.

141. McKinney, J.D., *Metabolism and disposition of inorganic arsenic in laboratory animals and humans.* Environmental Geochemistry and Health, 1992. **14**(2): p. 43-48.

142. Healy, S.M., et al., *Enzymatic methylation of arsenic compounds: V. arsenite methyltransferase activity in tissues of mice.* Toxicology and Applied Pharmacology, 1998. **148**(1): p. 65-70.

143. Scarpettini, A.F. and A.V. Bragas, *Coverage and aggregation of gold nanoparticles on silanized glasses.* Langmuir, 2010. **26**(20): p. 15948-15953.

144. Fricke, M., et al., *Dimethylthioarsinic anhydride: a standard for arsenic speciation.* Analytica Chimica Acta, 2007. **583**(1): p. 78-83.

145. Haiduc, I. and L. Silaghi-Dumitrescu, *Organotin and tin (IV) derivatives of dimethyldithioarsinic acid.* Journal of Organometallic Chemistry, 1982. **225**(1): p. 225-232.

146. Wong, M.W., *Vibrational frequency prediction using density functional theory.* Chemical Physics Letters, 1996. **256**(4-5): p. 391-399.

147. Zingaro, R.A., et al., *Rearrangement of tetramethyldiarsine disulfide.* Journal of the American Chemical Society, 1971. **93**(22): p. 5677-5681.

148. Wu, D.-Y., et al., *Photon-driven charge transfer and photocatalysis of p-aminothiophenol in metal nanogaps: a DFT study of SERS.* Chemical Communications, 2011. **47**(9): p. 2520-2522.

149. Smith, S.R., et al., *Characterization of a self-assembled monolayer of 1-thio-β-D-glucose with electrochemical surface enhanced Raman spectroscopy using a nanoparticle modified gold electrode.* Langmuir, 2015. **31**(36): p. 10076-10086.

150. Kočišová, E., et al., *Drop coating deposition of a liposome suspension on surfaces with different wettabilities:"coffee ring" formation and suspension preconcentration.* Physical Chemistry Chemical Physics, 2017. **19**(1): p. 388-393.

151. Kočišová, E. and M. Procházka, *Drop-coating deposition Raman spectroscopy of porphyrins.* Journal of Raman Spectroscopy, 2015. **46**(2): p. 280-282.

152. Yang, M., et al., *Arsenic Speciation on Silver Nanofilms by Surface-Enhanced Raman Spectroscopy.* Analytical Chemistry, 2019.

153. Huang, Y.F., et al., *Activation of Oxygen on Gold and Silver Nanoparticles Assisted by Surface Plasmon Resonances.* Angewandte Chemie International Edition, 2014. **53**(9): p. 2353-2357.

154. Shukla, R., et al., *Biocompatibility of gold nanoparticles and their endocytotic fate inside the cellular compartment: a microscopic overview.* Langmuir, 2005. **21**(23): p. 10644-10654.

155. Boulogne, F., F. Ingremeau, and H.A. Stone, *Coffee-stain growth dynamics on dry and wet surfaces.* Journal of Physics: Condensed Matter, 2016. **29**(7): p. 074001.

156. Hu, H. and R.G. Larson, *Analysis of the effects of Marangoni stresses on the microflow in an evaporating sessile droplet.* Langmuir, 2005. **21**(9): p. 3972-3980.

157. Yi, J., H. Jeong, and J. Park, *Modulation of nanoparticle separation by initial contact angle in coffee ring effect.* Micro and Nano Systems Letters, 2018. **6**(1): p. 17.

158. Park, J.-W. and J.S. Shumaker-Parry, *Structural study of citrate layers on gold nanoparticles: role of intermolecular interactions in stabilizing nanoparticles.* Journal of the American Chemical Society, 2014. **136**(5): p. 1907-1921.

159. Giljohann, D.A., et al., *Gold nanoparticles for biology and medicine.* Angewandte Chemie International Edition, 2010. **49**(19): p. 3280-3294.

160. Bellino, M.G., E.J. Calvo, and G. Gordillo, *Adsorption kinetics of charged thiols on gold nanoparticles.* Physical Chemistry Chemical Physics, 2004. **6**(2): p. 424-428.

161. Lin, S.-Y., et al., *Two-step functionalization of neutral and positively charged thiols onto citrate-stabilized Au nanoparticles.* The Journal of Physical Chemistry B, 2004. **108**(7): p. 2134-2139.

162. Perera, G.S., et al., *Facile displacement of citrate residues from gold nanoparticle surfaces.* Journal of Colloid and Interface Science, 2017.

163. Krüger, D., et al., *Interaction of short-chain alkane thiols and thiolates with small gold clusters: Adsorption structures and energetics.* The Journal of Chemical Physics, 2001. **115**(10): p. 4776-4786.

164. Goldmann, C., et al., *Charge transfer at hybrid interfaces: Plasmonics of aromatic thiol-capped gold nanoparticles.* ACS Nano, 2015. **9**(7): p. 7572-7582.

165. Magura, J., et al., *Thiol-modified gold nanoparticles deposited on silica support using dip coating.* Applied Surface Science, 2014. **315**: p. 392-399.

166. Hoft, R.C., et al., *Adsorption of amine compounds on the Au (111) surface: a density functional study.* The Journal of Physical Chemistry C, 2007. **111**(37): p. 13886-13891.

167. Bhardwaj, R., X. Fang, and D. Attinger, *Pattern formation during the evaporation of a colloidal nanoliter drop: a numerical and experimental study.* New Journal of Physics, 2009. **11**(7): p. 075020.

168. Xu, X. and J. Luo, *Marangoni flow in an evaporating water droplet.* Applied Physics Letters, 2007. **91**(12): p. 124102.

169. Zhong, X., A. Crivoi, and F. Duan, *Sessile nanofluid droplet drying.* Advances in Colloid and Interface Science, 2015. **217**: p. 13-30.

170. Kim, J.-H., et al., *Evaporation of water droplets on polymer surfaces.* Langmuir, 2007. **23**(11): p. 6163-6169.

171. Dugyala, V.R. and M.G. Basavaraj, *Evaporation of sessile drops containing colloidal rods: coffee-ring and order–disorder transition.* The Journal of Physical Chemistry B, 2015. **119**(9): p. 3860-3867.

172. Hara, R., et al., *Surface-enhanced Raman spectroscopy using a coffee-ring-type three-dimensional silver nanostructure.* RSC Advances, 2015. **5**(2): p. 1378-1384.

173. Kopecký Jr, V. and V. Baumruk, *Structure of the ring in drop coating deposited proteins and its implication for Raman spectroscopy of biomolecules.* Vibrational Spectroscopy, 2006. **42**(2): p. 184-187.

174. Baldwin, K.A., et al., *Monolith formation and ring-stain suppression in low-pressure evaporation of poly (ethylene oxide) droplets.* Journal of Fluid Mechanics, 2012. **695**: p. 321-329.

175. Liamtsau, V. and Y. Cai. *Application of nanofilms for arsenic speciation using surface-enhanced Raman spectroscopy (SERS)*. in *Environmental Arsenic in a Changing World: Proceedings of the 7th International Congress and Exhibition on Arsenic in the Environment (AS 2018), July 1-6, 2018, Beijing, PR China*. 2019. CRC Press.

176. Adamczyk, Z. and P. Weroński, *Application of the DLVO theory for particle deposition problems.* Advances in Colloid and Interface Science, 1999. **83**(1-3): p. 137-226.

177. Morales, V.n.L., et al., *Surfactant-mediated control of colloid pattern assembly and attachment strength in evaporating droplets.* Langmuir, 2013. **29**(6): p. 1831-1840.

178. Hoek, E.M. and G.K. Agarwal, *Extended DLVO interactions between spherical particles and rough surfaces.* Journal of Colloid and Interface Science, 2006. **298**(1): p. 50-58.

179. Grasso, D., et al., *A review of non-DLVO interactions in environmental colloidal systems.* Reviews in Environmental Science and Biotechnology, 2002. **1**(1): p. 17-38.

180. Van Oss, C., R. Giese, and P.M. Costanzo, *DLVO and non-DLVO interactions in hectorite.* Clays Clay Miner, 1990. **38**(2): p. 151-159.

181. Zhang, M.-q., Q. Liu, and J.-t. Liu, *Extended DLVO theory applied to coal slime-water suspensions.* Journal of Central South University, 2012. **19**(12): p. 3558-3563.

182. Gan, W., B. Xu, and H.L. Dai, *Activation of thiols at a silver nanoparticle surface.* Angewandte Chemie International Edition, 2011. **50**(29): p. 6622-6625.

183. Schlenoff, J.B., M. Li, and H. Ly, *Stability and self-exchange in alkanethiol monolayers.* Journal of the American Chemical Society, 1995. **117**(50): p. 12528-12536.

184. Rouhana, L.L., M.D. Moussallem, and J.B. Schlenoff, *Adsorption of short-chain thiols and disulfides onto gold under defined mass transport conditions: coverage, kinetics, and mechanism.* Journal of the American Chemical Society, 2011. **133**(40): p. 16080-16091.

185. Han, Y. and K. Uosaki, *Effects of concentration and temperature on the formation process of decanethiol self-assembled monolayer on Au (1 1 1) followed by electrochemical reductive desorption.* Electrochimica Acta, 2008. **53**(21): p. 6196-6201.

186. Van Rees, K.C., et al., *Evaluation of laboratory techniques for measuring diffusion coefficients in sediments.* Environmental Science & Technology, 1991. **25**(9): p. 1605-1611.

187. Matos, A., et al., *Retardation factors and the dispersion-diffusion coefficients of Zn, Cd, Cu, and Pb in soils from Vicosa-MG, Brazil.* Transactions of the ASAE, 1999. **42**(4): p. 903.

188. Becke, A.D., *Becke's three parameter hybrid method using the LYP correlation functional.* J. Chem. Phys, 1993. **98**(492): p. 5648-5652.

189. Lee, C., W. Yang, and R. Parr, *Density-functional exchange-energy approximation with correct asymptotic behaviour.* Phys. Rev. B, 1988. **37**(2): p. 785-789.

190. Couty, M. and M.B. Hall, *Basis sets for transition metals: Optimized outer p functions.* Journal of Computational Chemistry, 1996. **17**(11): p. 1359-1370.

191. Hariharan, P.C. and J.A. Pople, *The influence of polarization functions on molecular orbital hydrogenation energies.* Theoretica Chimica Acta, 1973. **28**(3): p. 213-222.

192. Shao, Y., et al., *Advances in molecular quantum chemistry contained in the Q-Chem 4 program package.* Molecular Physics, 2015. **113**(2): p. 184-215.

193. Al-Johani, H., et al., *The structure and binding mode of citrate in the stabilization of gold nanoparticles.* Nature Chemistry, 2017. **9**(9): p. 890.

194. Maksymovych, P., et al., *Gold adatom as a key structural component in self-assembled monolayers of organosulfur molecules on Au (1 1 1).* Progress in Surface Science, 2010. **85**(5-8): p. 206-240.

195. Tapia, O. and O. Goscinski, *Self-consistent reaction field theory of solvent effects.* Molecular Physics, 1975. **29**(6): p. 1653-1661.

196. Bryantsev, V.S., M.S. Diallo, and W.A. Goddard Iii, *Calculation of solvation free energies of charged solutes using mixed cluster/continuum models.* The Journal of Physical Chemistry B, 2008. **112**(32): p. 9709-9719.

197. Liu, Y., *Is the free energy change of adsorption correctly calculated?* Journal of Chemical & Engineering Data, 2009. **54**(7): p. 1981-1985.

198. Kubackova, J., et al., *Sensitive surface-enhanced Raman spectroscopy (SERS) detection of organochlorine pesticides by alkyl dithiol-functionalized metal nanoparticles-induced plasmonic hot spots.* Analytical Chemistry, 2014. **87**(1): p. 663-669.

199. Ansar, S.M., et al., *Determination of the binding affinity, packing, and conformation of thiolate and thione ligands on gold nanoparticles.* The Journal of Physical Chemistry C, 2010. **115**(3): p. 653-660.

200. Di Felice, R., A. Selloni, and E. Molinari, *DFT study of cysteine adsorption on Au (111).* The Journal of Physical Chemistry B, 2003. **107**(5): p. 1151-1156.

201. Reimers, J.R., et al., *Competition of van der Waals and chemical forces on gold–sulfur surfaces and nanoparticles.* Nature Reviews Chemistry, 2017. **1**(2): p. 0017.

202. Reimers, J.R., et al., *Gold surfaces and nanoparticles are protected by Au (0)–thiyl species and are destroyed when Au (I)–thiolates form.* Proceedings of the National Academy of Sciences, 2016: p. 201600472.

203. Costelle, L., et al., *Binding of deposited gold clusters to thiol self-assembled monolayers on Au (111) surfaces.* Applied Physics Letters, 2011. **98**(4): p. 043107.

204. Lavrich, D.J., et al., *Physisorption and chemisorption of alkanethiols and alkyl sulfides on Au (111).* The Journal of Physical Chemistry B, 1998. **102**(18): p. 3456-3465.

205. Gong, L., et al., *Colorimetric aggregation assay for arsenic (III) using gold nanoparticles.* Microchimica Acta, 2017. **184**(4): p. 1185-1190.

206. Matulis, S.M., et al., *Darinaparsin induces a unique cellular response and is active in an arsenic trioxide-resistant myeloma cell line.* Molecular Cancer Therapeutics, 2009. **8**(5): p. 1197-1206.

207. Chen, B., et al., *Therapeutic and analytical applications of arsenic binding to proteins*. Metallomics, 2015. **7**(1): p. 39-55.

208. Camacho, L., et al., *Phase-1 trial of ZIO-101, a novel organic arsenic in patients with advanced cancers*. Journal of Clinical Oncology, 2006. **24**(18_suppl): p. 13041-13041.

209. Hosein, P.J., et al., *A multicenter phase II study of darinaparsin in relapsed or refractory Hodgkin's and non-Hodgkin's lymphoma.* American Journal of Hematology, 2012. **87**(1): p. 111-114.

210. Tsimberidou, A.M., et al., *A phase I clinical trial of darinaparsin in patients with refractory solid tumors.* Clinical Cancer Research, 2009. **15**(14): p. 4769-4776.

211. Stice, S., et al., *Determination of multiple human arsenic metabolites employing high performance liquid chromatography inductively coupled plasma mass spectrometry*. Journal of Chromatography B, 2016. **1009**: p. 55-65.

212. Garnier, N., et al., *The novel arsenical darinaparsin is transported by cystine importing systems.* Molecular Pharmacology, 2014. **85**(4): p. 576-585.

213. Tian, J., et al., *Darinaparsin: solid tumor hypoxic cytotoxin and radiosensitizer.* Clinical Cancer Research, 2012. **18**(12): p. 3366-3376.

214. Shen, S., et al., *Arsenic binding to proteins.* Chemical Reviews, 2013. **113**(10): p. 7769-7792.

215. Xu, X., et al., *S-Dimethylarsino-glutathione (darinaparsin®) targets histone H3. 3, leading to TRAIL-induced apoptosis in leukemia cells.* Chemical Communications, 2019. **55**(87): p. 13120-13123.

216. Pinyayev, T.S., et al., *Preabsorptive metabolism of sodium arsenate by anaerobic microbiota of mouse cecum forms a variety of methylated and thiolated arsenicals.* Chemical Research in Toxicology, 2011. **24**(4): p. 475-477.

217. Raab, A., et al., *Pentavalent arsenic can bind to biomolecules.* Angewandte Chemie, 2007. **119**(15): p. 2648-2651.

218. Liamtsau, V., et al., *Speciation of thioarsenicals through application of coffee ring effect on gold nanofilm and surface-enhanced Raman spectroscopy.* Analytica Chimica Acta, 2020. **1106**: p. 88-95.

219. Kato, A., et al., *Pharmacodynamics of S-dimethylarsino-glutathione, a putative metabolic intermediate of inorganic arsenic, in mice.* Biochemical Pharmacology, 2017. **126**: p. 79-86.

220. Nims, C., et al., *Low frequency Raman spectroscopy for micron-scale and in vivo characterization of elemental sulfur in microbial samples.* Scientific Reports, 2019. **9**(1): p. 1-12.

221. Slavin, S., et al., *Adsorption behaviour of sulfur containing polymers to gold surfaces using QCM-D.* Soft Matter, 2012. **8**(1): p. 118-128.

222. Michota, A. and J. Bukowska, *Surface-enhanced Raman scattering (SERS) of 4-mercaptobenzoic acid on silver and gold substrates.* Journal of Raman Spectroscopy, 2003. **34**(1): p. 21-25.

223. Ghersi, D. and M. Singh, *molBLOCKS: decomposing small molecule sets and uncovering enriched fragments.* Bioinformatics, 2014. **30**(14): p. 2081-2083.

224. Yi, J., H. Jeong, and J. Park, *Modulation of nanoparticle separation by initial contact angle in coffee ring effect.* Micro and Nano Systems Letters, 2018. **6**(1): p. 1-7.

225. Kim, D.J., et al., *SERS-Active-Charged Microgels for Size-and Charge-Selective Molecular Analysis of Complex Biological Samples.* Small, 2018. **14**(40): p. 1802520.

226. Wang, Z., et al., *SERS-activated platforms for immunoassay: probes, encoding methods, and applications.* Chemical Reviews, 2017. **117**(12): p. 7910-7963.

227. Sharma, B., et al., *SERS: Materials, applications, and the future.* Materials Today, 2012. **15**(1-2): p. 16-25.

228. Karthigeyan, D., et al., *SERS and MD simulation studies of a kinase inhibitor demonstrate the emergence of a potential drug discovery tool.* Proceedings of the National Academy of Sciences, 2014. **111**(29): p. 10416-10421.

229. Kneipp, K., et al., *Single molecule detection using surface-enhanced Raman scattering (SERS).* Physical Review Letters, 1997. **78**(9): p. 1667.

230. Kleinman, S.L., et al., *Creating, characterizing, and controlling chemistry with SERS hot spots.* Physical Chemistry Chemical Physics, 2013. **15**(1): p. 21-36.

231. Vo-Dinh, T., *SERS chemical sensors and biosensors: new tools for environmental and biological analysis.* Sensors and Actuators B: Chemical, 1995. **29**(1-3): p. 183-189.

232. Schatz, G.C. and R.P.J.H.o.v.s. Van Duyne, *Electromagnetic mechanism of surface-enhanced spectroscopy*. 2002, Wiley: New York. p. 759-774.

233. Doorn, S.K., et al., *Experimental assessment of dynamic structural parameters for homogeneous and interfacial charge-transfer reactions: case studies based on time-dependent Raman scattering methods.* Electrochimica Acta, 1991. **36**(11-12): p. 1775-1785.

234. Mariscal, M., et al., *On the atomic structure of thiol-protected gold nanoparticles: a combined experimental and theoretical study.* Physical Chemistry Chemical Physics, 2010. **12**(37): p. 11785-11790.

235. Mdluli, P.S., et al., *Surface enhanced Raman spectroscopy (SERS) and density functional theory (DFT) study for understanding the regioselective adsorption of pyrrolidinone on the surface of silver and gold colloids.* Journal of Molecular Structure, 2009. **935**(1-3): p. 32-38.

236. Li, J.-F., et al., *SERS and DFT study of water on metal cathodes of silver, gold and platinum nanoparticles.* Physical Chemistry Chemical Physics, 2010. **12**(10): p. 2493-2502.

237. Caporali, S., et al., *SERS, XPS and DFT study of xanthine adsorbed on citrate-stabilized gold nanoparticles.* Sensors, 2019. **19**(12): p. 2700.

238. Liamtsau, V., et al., *Speciation of thioarsenicals through application of coffee ring effect on gold nanofilm and surface-enhanced Raman spectroscopy.* Analytica Chimica Acta, 2020. **1106**: p. 88-95.

239. Blackbourn, R.L., C.S. Johnson, and J.T. Hupp, *Surface intervalence enhanced Raman scattering from ferrocyanide on colloidal titanium dioxide. A mode-by-mode description of the Franck-Condon barrier to interfacial charge transfer.* Journal of the American Chemical Society, 1991. **113**(3): p. 1060-1062.

240. Ma, H., et al., *Charge-transfer effect on surface-enhanced Raman spectroscopy in Ag/PTCA: Herzberg–Teller selection rules.* The Journal of Physical Chemistry C, 2017. **121**(46): p. 25788-25794.

241. Woods, R., G. Hope, and K. Watling, *A SERS spectroelectrochemical investigation of the interaction of 2-mercaptobenzothiazole with copper, silver and gold surfaces.* Journal of Applied Electrochemistry, 2000. **30**(11): p. 1209-1222.

242. Larsson, J., M. Nolan, and J.C. Greer, *Interactions between thiol molecular linkers and the Au13 nanoparticle.* The Journal of Physical Chemistry B, 2002. **106**(23): p. 5931-5937.

243. Sellers, H., et al., *Structure and binding of alkanethiolates on gold and silver surfaces: implications for self-assembled monolayers.* Journal of the American Chemical Society, 1993. **115**(21): p. 9389-9401.

244. Beardmore, K.M., et al., *Determination of the headgroup-gold (111) potential surface for alkanethiol self-assembled monolayers by ab initio calculation.* Chemical Physics Letters, 1998. **286**(1-2): p. 40-45.

245. Wei, H., et al., *Real-time monitoring of ligand exchange kinetics on gold nanoparticle surfaces enabled by hot spot-normalized surface-enhanced Raman scattering.* Environmental Science & Technology, 2018. **53**(2): p. 575-585.

246. Capocefalo, A., et al., *Exploring the potentiality of a SERS-active pH nano-biosensor.* Frontiers in Chemistry, 2019. **7**: p. 413.

247. Ly, N.H. and S.W. Joo, *Surface anchoring mode-dependent hydrolysis reactions of hydrazone groups on gold examined by pH-dependent Raman spectroscopy.* Journal of Raman Spectroscopy, 2015. **46**(11): p. 1082-1086.

248. Wei, H., et al., *Real-time monitoring of ligand exchange kinetics on gold nanoparticle surfaces enabled by hot spot-normalized surface-enhanced Raman scattering.* Environmental Science & Technology. 2018. **53**(2): p. 575-585.

249. Wei, H., Q. Huang, and P.J. Vikesland, *The Aromatic Amine p K a Determines the Affinity for Citrate-Coated Gold Nanoparticles: In Situ Observation via Hot Spot-Normalized Surface-Enhanced Raman Spectroscopy.* Environmental Science & Technology Letters, 2019. **6**(4): p. 199-204.

250. Kim, K., et al., *Surface-enhanced Raman scattering of 4-aminobenzenethiol on Ag and Au: pH dependence of b 2-type bands.* The Journal of Physical Chemistry C, 2012. **116**(7): p. 4774-4779.

251. Chong, N.S., et al., *Significance of chemical enhancement effects in surface-enhanced Raman scattering (SERS) signals of aniline and aminobiphenyl isomers.* Vibrational Spectroscopy, 2015. **81**: p. 22-31.

252. Iosin, M., V. Canpean, and S. Astilean, *Spectroscopic studies on pH-and thermally induced conformational changes of Bovine Serum Albumin adsorbed onto gold nanoparticles.* Journal of Photochemistry and Photobiology A: Chemistry, 2011. **217**(2-3): p. 395-401.

253. Dou, X.-M. and Y. Ozaki, *Surface-Enchanced Raman Scattering of Biological Molecules on Metal Colloids: Basic Studies and Applications to Quantitative Assay.* Reviews in Analytical Chemistry, 1999. **18**(4): p. 285-321.

254. Taladriz-Blanco, P., et al., *Reversible assembly of metal nanoparticles induced by penicillamine. Dynamic formation of SERS hot spots.* Journal of Materials Chemistry, 2011. **21**(42): p. 16880-16887.

255. dos Santos Jr, D.S., et al., *Controlling the size and shape of gold nanoparticles in fulvic acid colloidal solutions and their optical characterization using SERS.* Journal of Materials Chemistry, 2005. **15**(29): p. 3045-3049.

256. Lopez-Tobar, E., et al., *Stability of the disulfide bond in cystine adsorbed on silver and gold nanoparticles as evidenced by SERS data.* The Journal of Physical Chemistry C, 2013. **117**(3): p. 1531-1537.

257. Xiang, S.Q., et al., *Simulating pH-dependent surface-enhanced Raman spectra by density functional theory calculations.* Journal of Raman Spectroscopy, 2019. **50**(8): p. 1065-1073.

258. Tu, Q., J. Eisen, and C. Chang, *Surface-enhanced Raman spectroscopy study of indolic molecules adsorbed on gold colloids.* Journal of Biomedical Optics, 2010. **15**(2): p. 020512.

259. Lim, J.K. and S.-W. Joo, *Gold nanoparticle-based pH sensor in highly alkaline region at pH> 11: surface-enhanced Raman scattering study.* Applied Spectroscopy, 2006. **60**(8): p. 847-852.

260. Bu, Y. and S.-W. Lee, *The characteristic AgcoreAushell nanoparticles as SERS substrates in detecting dopamine molecules at various pH ranges.* International Journal of Nanomedicine, 2015. **10**(Spec Iss): p. 47.

261. Sarkar, S., et al., *A pH dependent Raman and surface enhanced Raman spectroscopic studies of citrazinic acid aided by theoretical calculations.* Spectrochimica Acta Part A: Molecular and Biomolecular Spectroscopy, 2016. **169**: p. 108-115.

VITA

VALERY LIAMTSAU

Born, Minsk, Belarus

2008-2013	B.S., Chemistry Belarusian State University, Minsk, Belarus
2013-2015	Product Management Belmedpreparaty, Minsk, Belarus
2015-2016	Product Design Manager Smart study, Minsk, Belarus
2016-2021	Doctorate in Chemistry Florida International University, Miami, Florida
2016-2021	Teaching Assistant Florida International University, Miami, Florida
2020-2021	Dissertation Year Fellowship Florida International University, Miami, Florida

PUBLICATIONS AND PRESENTATIONS

1. Valery Liamtsau, Changjun Fan, Guangliang Liu, Anthony J. McGoron, and Yong Cai. *Speciation of thioarsenicals through application of coffee ring effect on gold nanofilm and surface-enhanced Raman spectroscopy*. Analytica Chimica Acta 1106 (2020): 88-95.

2. Mingwei Yang, Valery Liamtsau, Changjun Fan, Kelli L. Sylvers, Anthony J. McGoron, Guangliang Liu, Fengfu Fu, and Yong Cai, *Arsenic speciation on silver nanofilms by surface-enhanced raman spectroscopy.* Analytical Chemistry, 2019. 91(13): p. 8280-8288.

3. Valery Liamtsau and Yong Cai. *Application of nanofilms for arsenic speciation using surface-enhanced Raman spectroscopy (SERS)*. in *Environmental Arsenic in a Changing World: Proceedings of the 7th International Congress and Exhibition*

on Arsenic in the Environment (AS 2018), July 1-6, 2018, Beijing, PR China. 2019. CRC.

4. Valery Liamtsau, Guangliang Liu, Alexander Morozov, Alexander Mebel, Yong Cai. *Chromatographic framework for coffee ring effect-driven separation of small molecules in surface enhanced Raman spectroscopy analysis*.
   Submitted to Analytica Chimica Acta.

5. Valery Liamtsau, Guangliang Liu, Yong Cai. *Application of gold nanofilm–based coffee ring effect and surface-enhanced Raman spectroscopy for speciation of Darinaparsin*
   Submitted to Chromatography A.